

Synthesis and Functionalization of Nanoparticles with Biogenic Amines and their Biological Application

Synthese und Funktionalisierung von Nanopartikeln mit
biogenen Aminen und deren biologische Anwendung

Dissertation zur Erlangung des Doktorgrades
der Naturwissenschaftlichen Fachbereiche
im Fachgebiet Anorganische und Analytische Chemie
der Justus-Liebig-Universität Gießen

vorgelegt von

Friederike Britta Gasiorek
aus
Wehrheim

Gießen 2016

Diese Arbeit wurde im Zeitraum von Januar 2013 bis Februar 2016 am Institut für Anorganische und Analytische Chemie der Justus-Liebig-Universität Gießen angefertigt, unter der Betreuung von Prof. Dr. Sabine Schlecht begonnen und unter Herr Prof. Dr. Siegfried Schindler und Herr Prof. Dr. Mathias S. Wickleder beendet.

Erstgutachter: Prof. Dr. Siegfried Schindler

Zweitgutachter: Prof. Dr. Mathias S. Wickleder

Für meinen Vater

„Our greatest weakness lies in giving up. The most certain way to succeed is always to try just one more time.”

Thomas A. Edison

Table of Content

1.	Introduction.....	1
2.	Basic Knowledge	3
2.1	Nanomaterials	3
2.2	Metal Nanoparticles	8
2.1.1	Synthesis of Coinage Metal Nanoparticles	8
2.1.2	Optical Properties of Gold Nanoparticles	9
2.3	Semiconductor Nanoparticles	11
2.4	Surface Functionalization.....	16
2.5	Characterization	20
2.6	Nanoparticles in Biological Systems	22
2.7	Multivalent Ligands	24
3.	Motivation and Goals.....	27
4.	Gold Nanoparticles.....	29
4.1	Syntheses of Gold Nanoparticles	29
4.2	Optical Properties.....	33
4.3	Alloyed Metal Nanoparticles	34
4.4	Ligand Exchange Reactions at Gold Nanoparticles	35
4.5	Gold Nanoparticles with Positively Charged Ligands	42
4.6	Mixed Ligand Shells on Gold Nanoparticles	45
4.7	Functionalization at the Ligand Periphery	47
4.8	Functionalization with Bioactive Amines	49
4.9	Biological Functionality.....	57
4.10	Effects of Multivalent Histamine Supported on Gold Nanoparticles: Activation of Histamine Receptors by Derivatized Histamine at Subnanomolar Concentrations	62
5.	Quantum Dots	79
5.1	Quantum Dots for Cellular Imaging	79

Table of Content

5.2	The Ternary System $\text{CdTe}_x\text{Se}_{1-x}$ -MPA	88
6.	Summary/Zusammenfassung	93
6.1	Summary	93
6.2	Zusammenfassung	95
7.	Outlook.....	99
8.	Experimental Section	101
8.1	Chemicals, Solvents and Consumables	101
8.2	Analytics.....	101
8.3	Synthesis of the Nanoparticles	104
8.4	Ligand Exchange Reactions	107
8.5	Dithiocarbamate Functionalized Gold Nanoparticles.....	109
8.6	Positively Charged Gold Nanoparticles	110
8.7	Mixed Ligand Shell	111
8.8	Functionalization of the Particles Shell.....	112
8.9	Synthesis of the Ligands.....	115
8.10	Synthesis of Quantum Dots.....	118
9.	References	123
10.	Appendix	135
10.1	Abbreviations and Symbols.....	135
10.2	Calculation of core diameters	136
10.3	List of Figures	137
10.4	List of Tables.....	142
11.	Publications and Presentations	143
12.	Lebenslauf	144
13.	Acknowledgement.....	145
14.	Erklärung	147

1. Introduction

Nowadays nanotechnology is omnipresent: from nanodevices in technology to nanorobots for medicine, a lot of materials have found their way into our daily life. Sunscreens based on nanoparticles made of titanium dioxide or zinc oxide or clothes with nanosilver, which are able to kill bacteria and eradicate unwanted odor are only two examples of nanomaterials making our daily life more comfortable. A special feature of nanotechnology is its cross section character. It contains pulses from almost every scientific-technical disciplines and in many branches this promising technology is indispensable. Accordingly the importance of nanotechnology increases steadily. While nanomaterials already enhance the properties of many products in present life, future techniques are under development. What *Ostwald* described in 1914 as “The world of neglected dimensions” is today known as nanochemistry. [1] He saw the opportunities, new properties and interesting application of these materials.

Even though it is a relatively young topic, nanotechnology has become a widely inquired branch of science. The number of publications with “nanoparticles” as buzzword exponentially increased during the last decades. In 2014 a special issue for Nanotechnology & Nanomaterials, Nanotoxicology & Nanomedicine appeared in *Angewandte Chemie Int. Ed.* summarizing the versatile applications. [2]

The term *nano* emanates from the Greek word for dwarf and is on prefix at the metric scale for the factor 10^{-9} ($1 \text{ nm} = 10^{-9} \text{ m}$). For comparison, the diameter of a human hair is about a thousand times larger but still visible to the naked eye, red blood cells are even smaller and the size of a virus is about 20 nm to 100 nm (Figure 1). Objects with a size less than 100 nm are typically called nanomaterials.

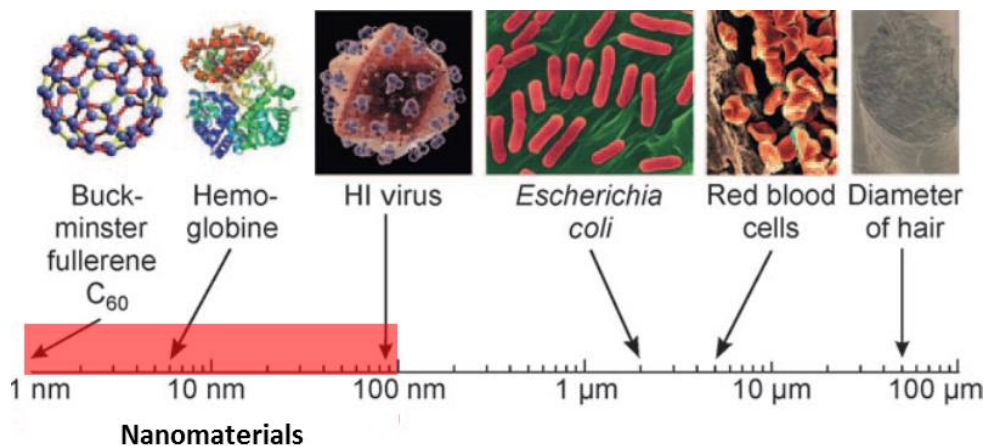


Figure 1: Length scale for classification of nanomaterials. Adapted from [3]

Besides the size, their large surface area is characteristic for these materials compared to the bulk material and the physicochemical properties are directly dependent. The surface properties are characteristic for nanomaterials and due to the increased surface-to-volume ratio they are different compared to their bulk material. Nanoparticles resemble both bulk material and molecules, they combine the ability to move (molecule) with specific properties of solids, e. g. catalytic activity, magnetism, surface.

The interaction of nanoscale materials with biological systems is currently the focus of a fast-growing area of investigation and progress in nanomedicine increased rapidly in the last years. As these interactions are mostly governed by the surface of the particles, modifications of those can tune the properties. Nanoparticulate materials are in a comparable size range relative to proteins or enzymes, they can selectively intervene in cellular processes in a way that small molecules cannot. Engineered nanoparticles have shown versatile applications for e. g. drug delivery. Compared to conventional therapeutics nanoparticles can overcome problems like poor solubility, lack of targeting or non-specific distribution. Remarkable progress has been made in the development of new nanomaterials with enhanced water-solubility, bioavailability and reduced toxicity. Although nanomaterials are currently widely used, there is a lack of information concerning environmental implications and it is necessary to spend investigations on the behavior. Gold nanoparticles have been used for biomedical applications since their colloidal synthesis. Because of their high biocompatibility they have versatile applications. A lot of synthetic approaches have been developed to prepare size- and shape-controlled particles. Future challenges will be to find new methods of functionalizing gold nanoparticles with compounds that involve sufficient biocompatibility and are efficient pharmaceutical agents.

2. Basic Knowledge

2.1 Nanomaterials

The development of colloidal chemistry is closely related to the advances in methods and techniques and colloidal gold for example is no invention of modern times. It was Michael Faraday who reported on the earliest experimental studies on noble metals and their interactions with light giving a first description of colloidal solutions. [4] He reduced tetrachloroaurate (AuCl_4^-) with phosphorous in CS_2 and obtained a deep red solution. He described it as finely disperse gold, not knowing that the optical phenomenon was caused by nanoparticles. Scientists assumed much earlier that gold must be present in such a degree that it is not visible to the human eye. [5] The term colloid, from the French word *colle* (glue), was introduced by Thomas Graham in 1861. [6] Some colloidal phenomena are known unconsciously since applications in ancient times, e. g. inks or cosmetics and manufacturing of colored glass based on dispersions of pigments. The Lycurgus cup is a fascinating example for nanomaterials from ancient times (Figure 2). Dated back in the 4th century B.C. it is a masterpiece of handcraft for this time. It appears in different colors depending of the incident of light; if it is reflected it appears jade green, if it is transmitted it appears ruby red. The material consists of metal nanoparticles of gold and silver. [7] Another example for nanomaterials in daily use is the *Purple of Cassius*. It was popular in the 17th century as colorant for glasses consisting of gold particles and tin oxide. [8]



Figure 2: The Lycurgus cup contains nanoparticles of gold and silver (British Museum). [9]

At the nano-scale not only miniaturization but also changes in properties are possible. The TiO_2 , which is applied as UV/Vis protector in sunscreens, is only about 50 nm in diameter. Absorption of solar radiation is much higher in materials composed of nanoparticles than it is in thin films. At this size it appears no longer white but transparent and can be applied to the skin.

Nanoparticles with a diameter roughly between 10 nm and 100 nm are natural bridges between molecules and extended solids and are also called *advanced molecules*. They combine the molecular ability to move with properties of bulk material, like fluorescence. Besides their size, the vast surface area is also characteristic. Nanoparticles possess a high surface-to-volume ratio. For example 10 nm nanoparticles have about 20% of the atoms at the surface, whereas for 2 nm nanoparticles this value increases up to 80% surface atoms. These surface atoms are different in energy and mainly govern the properties of the material. [3] At the nanoscale the electronic energy states become discrete to unique optical, electronical and mechanical properties of the materials. Thus miniaturization has drastic effects for the physical and chemical properties. Not only for metal nanoparticles, but for all nanomaterials the characteristics at the submicroscopic scale are different. Gold as bulk material appears with a metallic glance, gold at the nanosize appears as a purple solution (Figure 3). In addition gold nanoparticles melt at much lower temperatures ($\sim 300^\circ\text{C}$ for 2.5 nm size) than the gold slabs (1064°C). This is due to the increasing number of surface atoms. Solid gold is inert against oxygen and is used for jewelry or tooth crowns. When presented in nanostructures it is very affine to oxygen and therefore applied as catalyst. The optical appearance at the nanoscale is also no longer metallic but red caused by quantum effects.



Figure 3: Gold as bulk material and dispersed in water as colloids.

Quantum effects are based on the fact that electrons behave both as particle and as wave resulting in the wave-particle-duality. When electrons are trapped in a space similar to their wavelength their energy levels are no longer continuous but discrete. The values depend on the size and shape of the particle. Other size-dependent property changes include quantum confinement in semiconductor

particles (CdSe, CdTe), surface plasmon resonance in some metal nanoparticles (Au, Ag) and superparamagnetism in magnetic materials (Fe_2O_3 , Fe_3O_4).

Within a colloidal system, nanoparticles are uniformly dispersed in an agent. Classification is made in dispersion, molecular and association colloids. Dispersion colloids are thermodynamically instable systems consisting of crystalline or amorphous solids in a liquid agent. Micelles and biocolloids belong to the category of associative colloids. The stabilization force of dispersion colloids basically derives from the repulsive interactions of the charge distribution around the particles or a stabilizing shell. [10] In this context *colloid* describes the characteristics and *nano* gives the indication for size and quantum effects.

Nanoparticles can be understood as a small unit of a solid, accordingly they can be synthesized by two different routes. While in the *top-down* method a macrocrystalline material is crushed down to nanoscale under mechanical action, in the *bottom-up* method nanoscopic structures are built from atomic components (Figure 4).

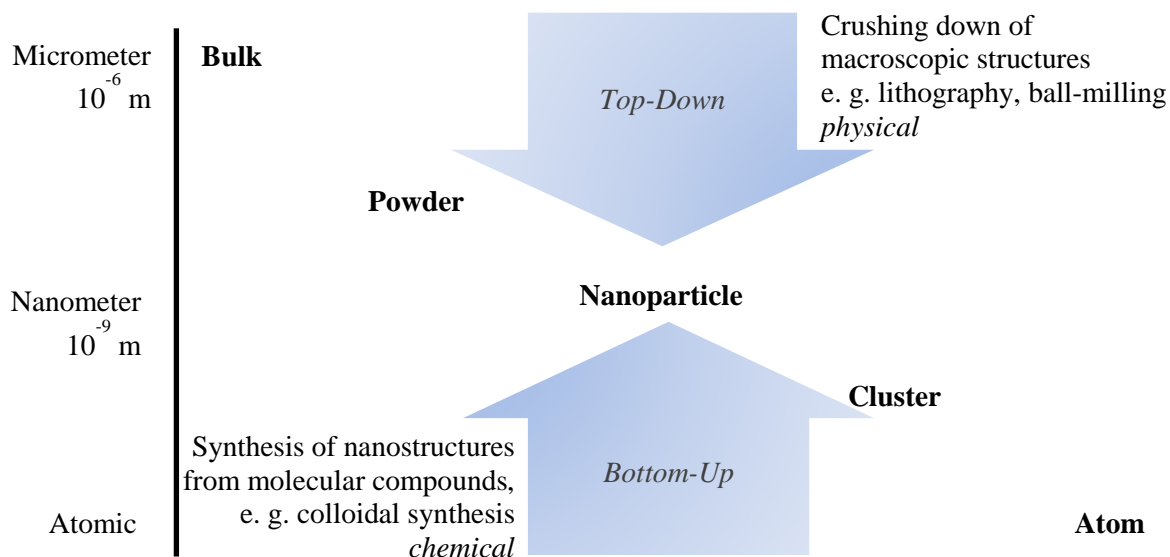


Figure 4: Top-down and bottom-up approach for the synthesis of nanoparticles.

In a top-down approach usually the nanoparticulate material is generated from the bulk material by *physical* methods, e. g. lithography. Contrastingly, bottom-up methods have a *chemical* approach. The bottom up synthesis starts with the nucleation step, and then the surface is saturated with further atoms (surface growth). The growth mechanism has to be stopped at the nanoscale and the

resulting nanoparticles have to be stabilized to avoid further particle growth. Nanomaterials are synthesized from molecular/atomic precursors usually in solution by self-organization. The growth mechanism can be controlled during the synthesis. The nanoparticles need to be stabilized at the surface to prevent coalescence.

The synthesis of nanoparticles is typically divided into a number of different steps: nucleation, nucleus growth and *Ostwald* ripening. Syntheses in the liquid phase can usually be adjusted, e. g. via the monomer concentration and reaction temperature. For monodisperse nanoparticles, nucleation, nucleus growth and agglomeration process have to be controlled precisely. The reactive surfaces can be saturated directly with stabilizers or ligands added to the solution. *LaMer* and *Dinegar* set up a model to describe the steps of nucleation and growth (Figure 5). [11]

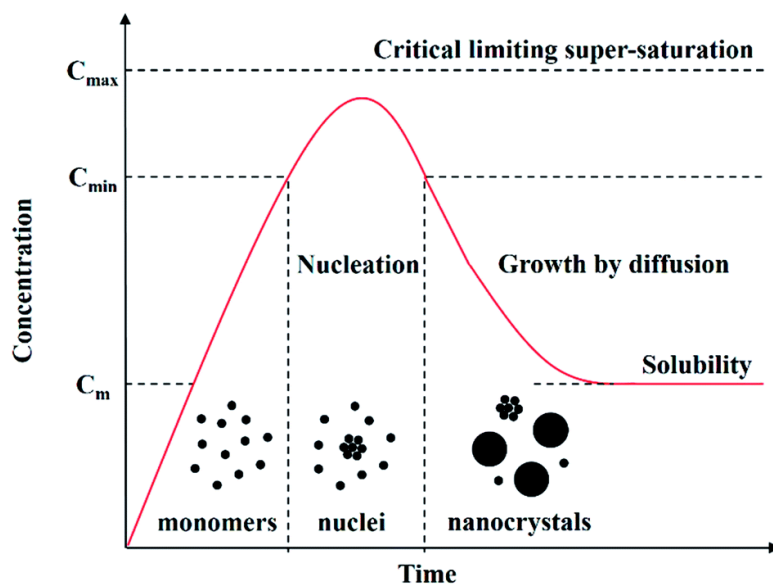


Figure 5: LaMer diagram to describe nucleation and nucleus growth. Adapted from [12]

The mechanism starts with the reduction or decomposition of the precursor and the increase of the monomeric building blocks. When a certain concentration is reached, nucleation starts and homogeneous crystal nuclei are formed. Thermodynamic control results in the most stable product, whereas the reduction of reaction velocity (kinetic control) can result in other structures. This can for example be achieved by a weak reducing agent. Subsequently, free atoms accumulate at the surface of the nuclei always alternating in loss of volume energy and increase of surface energy. Surfactants can control and stabilize the surface.

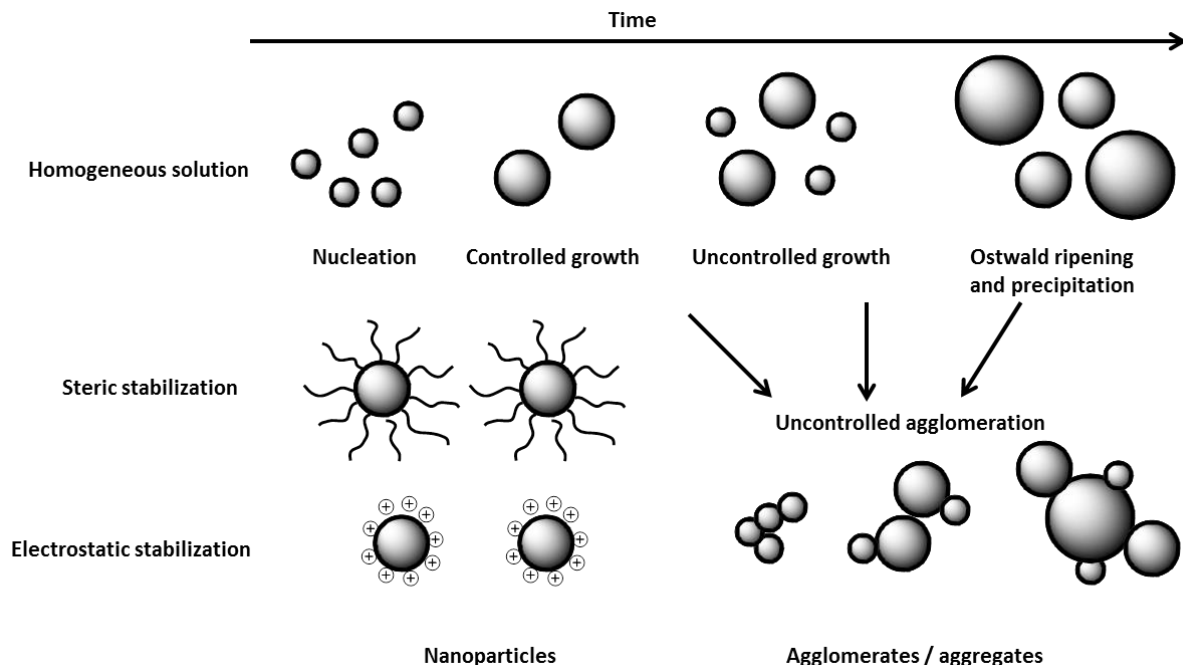


Figure 6: Growth and stabilization of nanoparticles. Adapted from [3]

As colloidal solutions are thermodynamically instable and aim for a stable state, the surface must be immediately saturated. This process can be suppressed by stabilization. This can either be achieved sterically or electrostatically (Figure 6). Within a colloidal system there are repulsive and attractive forces. Attractive actions result from dipole-dipole interactions and are also called van-der-Waals-forces. Repulsion results from electrostatic interactions from charged particles. Dispersed particles in a medium have a charge at their surface called charge cloud. It is symmetrically placed around the particle. When the particles move through a homogeneous phase the static and a part of the diffuse layer move along. Within this motion a potential barrier occurs between the layer and the surrounding medium. It increases linearly in the *Stern*-layer, a rigid layer around the particle, and falls exponentially in the diffuse layer. The resulting difference is called *zeta-potential*, which is a characteristic value for the stability of colloidal solutions and can be measured by electrophoresis or streaming potentials. It depends on the properties of the surface as well as of the solvent. Ligands surrounding the nanoparticles must be able to stabilize the colloidal solution either electrostatically or sterically. This can be achieved by surface tailoring. The stabilization of nanoparticles is described in the literature with various methods, mostly using polymers. A proper monolayer is often needed to shield the surface. The surface energy is decreased, which reduces the formation of aggregates.

2.2 Metal Nanoparticles

Compared to bulk metals, metallic nanoparticles have different properties due to their size and thus the resulting high surface-to-volume ratio. Nanostructured materials of coinage metals such as gold and silver have unique optical properties due to strong surface plasmon absorption in the visible region of light. [13] They have versatile applications in modern research and technology and are no longer indispensable. They are applied in catalysis, electronic compounds, sensors or medicinal devices. [14, 15] Their properties are based on physical parameters and can easily be tuned. Size, shape and structure are the mainly contributing parameters.

2.1.1 Synthesis of Coinage Metal Nanoparticles

Various synthetic procedures have been published. In the majority of reports, HAuCl_4 proved to be the favored starting material due to its ready availability, despite the disadvantage of limited control over nucleation process and possible chloride contamination in the resulting particles. This method was first described by *Turkevich* and enhanced by *Frens*. [16, 17] It is based on the chemical reduction of tetrachloroaurate with citrate in aqueous solution. Citrate is both reducing agent and ligand for the stabilization of the formed nanoparticles. Nanoparticles with a diameter between 10 nm and 100 nm can be prepared. *Frens* also showed that the colloidal stability strongly depends on the size of the nanoparticles. [18] Mechanistic studies on the formation of the nanoparticles showed that in the synthesis acetone is formed and stabilizes the surface. If NaBH_4 is used as reducing agent different particle sizes could be obtained and the surface can be covered with different ligands added during the synthesis. The reduction of AuCl_4^- with NaBH_4 in a two-phase system was described by *Brust and Schiffrin*. [19, 20] Nanoparticles of Au, Ag, Pt, and Ir in toluene can be readily synthesized using a biphasic reduction procedure. [21–23] A noble metal salt (e. g., HAuCl_4) dissolved in water is first extracted into an organic phase with the help of a phase transfer reagent, tetraoctylammonium bromide (TOAB). Upon reduction with NaBH_4 it is possible to obtain uniform-sized metal nanoparticles. Small gold nanoparticles with a diameter of <10 nm can be synthesized in organic solvents. 4-Dimethylaminopyridine (DMAP) is often used for the stabilization of the resulting nanoparticles in aqueous solution. [24, 25]

Stucky and co-workers developed a method for the reduction of a gold salt in organic solvents using an amine-borane complex and *n*-dodecanethiol for stabilization. [26] The resulting nanoparticles

have a narrow size distribution and are nearly spherical. Reaction time, temperature, molar ratios, and solvents can be varied to adjust the size of the gold nanoparticles. In addition, other metal nanoparticles like Ag, Pd, and alloy compositions can be synthesized. Furthermore, the synthesis can be easily upscaled to get multigrams of nanoparticles for applications. Gold nanoparticles smaller than ~ 1.5 nm consist of a distinct number of atoms and the compounds are called clusters. These gold clusters can either behave like discrete molecules or exhibit properties of nanoparticles, depending on the number of atoms. The well-known *Schmid*-cluster Au_{55} consists of a phosphine stabilized gold cluster $\text{Au}_{55}(\text{PPh}_3)_{12}\text{Cl}_6$ with a stable closed shell. It is a molecule with a well-defined formula weight, unlike the colloidal solutions. Different to nanoparticles they have no weakly bound ligands on the surface. In cluster structures metal-metal bonding interactions can be found. [27] Apart from spherical nanoparticles, other shapes of gold nanostructures can be synthesized. Nanorods can be prepared by a seeding growth mechanism. [28] Hollow gold nanospheres can be prepared by sacrificial galvanic replacement of cobalt nanoparticles. [29] Colloidal stability of the nanoparticles is the key challenge in synthesis and can be controlled by the ligands at the surface. Weakly capped nanoparticles agglomerate faster than those with strongly bound ligands. Citrate-capped gold nanoparticles are stabilized via weakly physisorption of citrate ions, whereas dodecanethiol-stabilized gold nanoparticles are stabilized via strongly chemisorbed thiolate ligands. [30] This thiol stabilization of gold nanoparticles and the self-assembly of organic sulfur compounds on gold surfaces was first reported by *Giersig* and *Mulvaney* and gave access to highly stable colloidal solutions. [31]

2.1.2 Optical Properties of Gold Nanoparticles

A characteristic of all gold colloids is the color, which can vary from light red via purple-red to blueish-red. The optical properties of gold nanoparticles, first described and attributed to those by Faraday in the 19th century, are unique and caused by quantum sized effects. The color results from absorption and scattering of electromagnetic irradiation by local surface plasmon resonance, a collective oscillation of the free electrons in the conduction band. The expression *plasmon* consists of the physical terms for plasma and vibration. For gold nanoparticles with different core size, the absorption maximum shifts. For larger nanoparticles it shifts to a longer wavelength, meaning lower energies (Figure 7). The maxima are also broadened. It is also possible to determine the particle size via the correlation with λ_{max} of the surface plasmon. [32] This phenomenon is very characteristic for both gold and silver nanoparticles, which appear red and yellow, respectively.

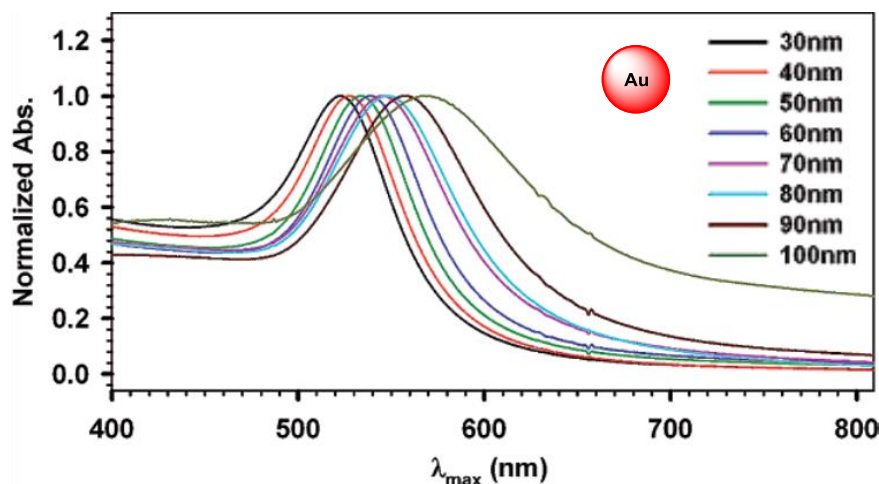


Figure 7: UV/Vis spectra (normalized) for Au nanoparticles with different core sizes in aqueous solution.

Adapted from [32]

When small spherical metallic nanoparticles are irradiated by light, the oscillating electric field causes the conduction electrons to oscillate coherently. The displaced electron cloud has a restoring force which arises from the Coulomb attractions between negatively charged electrons and positively charged nuclei (Figure 8). An oscillation caused by the displacement appears relative to the nuclei framework. When incoming light enters into resonance with the vibration of the electron cloud an amplification proceeds and the absorption is intensified.

The frequency is related to the size and shape of the resonance body and the density and effective mass of electrons. Thus metal nanoparticles of different sizes appear in different colors. For gold nanoparticles the maximum lies at around 520 nm, for silver nanoparticles at 420 nm with respect to a particle size of 20 nm.

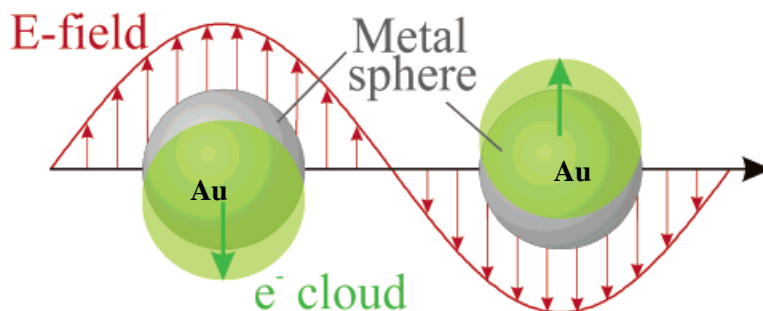


Figure 8: Plasmon resonance: scheme for oscillation of the electron cloud at a spherical nanoparticle.

Adapted from [33]

2.3 Semiconductor Nanoparticles

From a historical perspective the research on semiconductor-based nanomaterials is much younger than those based on metals, but many principles from metal nanoparticles could be transferred. In the beginning of the 1980s CdS colloids were synthesized and analyzed by *Grätzel*, *Brus* and *Henglein*. [34–36] A few years later the quantum size-effect has been introduced by *Brus*. [37] It describes the relation of size and electronic band gap and is based on a strong confinement of electrons and holes in a small particle with a diameter below the exciton Bohr radius, the average diameter between electron and hole. As the size is reduced the electronic excitation shifts to higher energies. It means that the larger the core diameters of semiconductor nanoparticles the lower the energy of the emitted light and the longer the wavelength. [38]

Semiconductor nanoparticles between 2 nm and 10 nm are quasi zero-dimensional single crystals and are often called quantum dots (QDs). These colloidal nanocrystals exhibit strong fluorescence with a size-dependent emission wavelength. The energy states become discrete (Figure 9). They possess unique optical properties and are often used in electronic and optical devices. QDs are applied for LEDs and solid-state lighting, displays, photovoltaics, transistors, quantum computing, medical imaging, biosensors, among many others.

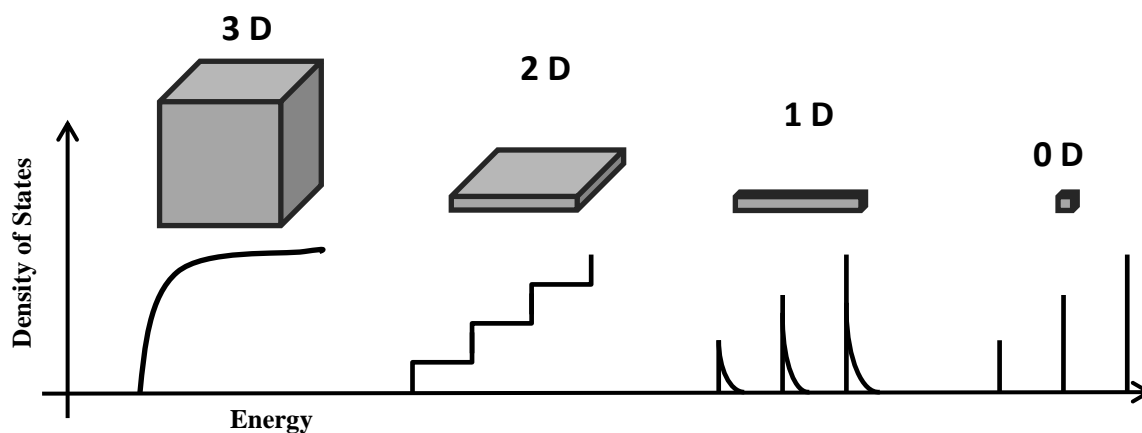


Figure 9: Density of states in a semiconductor crystal in dependence of the dimension. Adapted from [38]

The optical properties are a result of the quantum confinement effect and depend on size, shape and composition of the nanocrystals. Most common quantum dots are CdTe and CdSe. When the core

diameter of the QDs is smaller than the exciton Bohr radius, the energy levels become discrete and recombination on the band gap causes emission. Larger QDs emit longer wavelengths (Figure 10). For both materials at the nanoscale the emission wavelength lies in the visible part of the electromagnetic spectrum making these materials suitable for imaging of biological tissues. [39], [40] The photo- and electroluminescence properties can be fine-tuned to emit any color of light by changing the material's crystallite size.

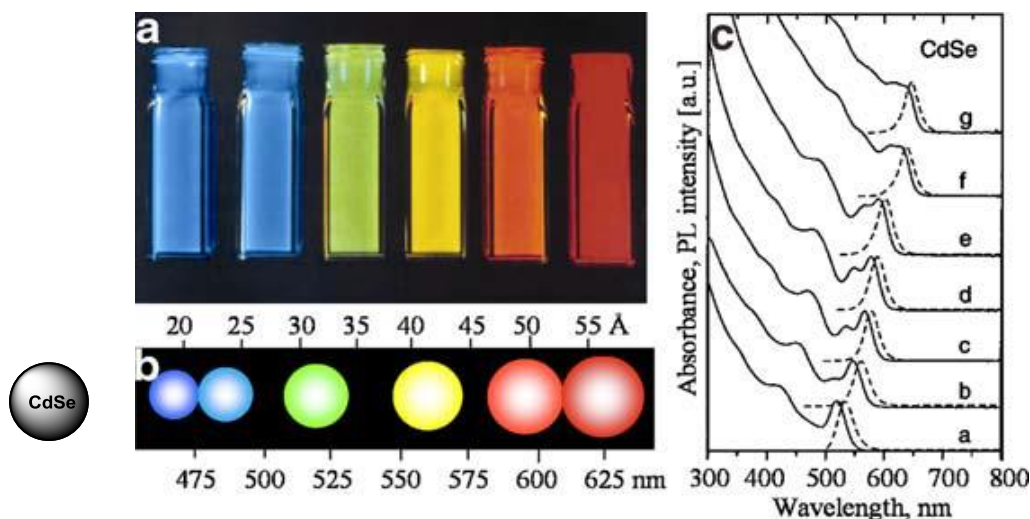


Figure 10: Size-dependent photoluminescence (a + b) and absorption and emission spectra (c) of CdSe.
Adapted from [41]

The size-dependent optical properties allow the synthesis of quantum dots covering the entire visible to near-IR wavelength range. A different growth of the nanocrystals, and therefore different optical properties, can be achieved by the use of different ligands in the synthesis. [42, 43] One major disadvantage of this tuning method is that each maximum is related to a different core size, which makes a direct comparison difficult. This could be avoided by the use of mixed crystal systems, multicomponent materials with gradient composition. A ternary system of CdTe and CdSe varies in chemical composition of the nanocrystal and the optical properties of both binary compounds can be combined. [44] In the core-shell structure of two component materials the external shell improves the quantum yields and gives stability to the nanocrystal.

Originally QDs were prepared by a *hot-injection* method, a bottom-up synthesis using dimethyl cadmium and a selenide or telluride precursor in a coordinating solvent with trioctylphosphine (TOP) and trioctylphosphine oxide (TOPO). [39] Besides the extremely toxic precursor the

resulting nanoparticles are capped with a hydrophobic shell, which makes them unsuitable for biological applications. Different cadmium precursors like CdO, Cd(OAc)₂ or CdCO₃ have been applied in the organic approach, but for biological applications solubility in water and stability are required. Synthesis in organic solvent must be followed by ligand exchange at the nanoparticles or they have to be synthesized directly in aqueous solution. The direct synthesis of cadmium chalcogenide nanoparticles in aqueous solution was achieved by thiol-capping of the nanocrystals yielding size-controlled and highly luminescent QDs. [45] First described by Weller and further investigated by Zhang CdTe nanocrystals were synthesized in aqueous solution. [42, 46] A freshly prepared NaHTe precursor solution is added to a mixture of Cd²⁺ ions and thiol ligands under inert conditions leading to highly luminescent CdTe quantum dots. Later different synthetic approaches using hydrothermal synthesis, ultrasonic or microwave irradiation were developed but mainly based on the procedure by Weller. [47–50]

To obtain water soluble quantum dots from organic synthesis the hydrophobic shell must be replaced by ligands providing both solubility in water and stability of the colloidal solution. Mercaptopropionic acid capped CdTe/ZnS nanocrystals could be synthesized via ligand exchange. [51] One major disadvantage of this method is the decreasing photoluminescence upon site exchange of the ligands. The impact of thiol ligands on the photophysical properties of quantum dots has been studied intensively. [52] They mainly depend on the concentration and pH value in solution.

Optical properties of quantum dots are mainly determined by the elements in the core material and are size-dependent. For some applications tuning of optical properties without changing the size is important, e. g. in cell uptake studies. This can be achieved by a variation of the core components. CdTe and CdSe nanocrystals are both versatile materials for biological applications, both emit in the visible to near infra-red spectra (Figure 11). Both compounds crystallize in cubic structures and a combination of both can lead to combined optical properties. Mixed crystal systems with a homogeneous internal structure allow fine tuning of optical properties. [53]

Compared to binary compounds like CdTe, CdSe or other semiconductors, ternary systems are only scarcely explored. Until now some ternary and quaternary systems have been synthesized and characterized. [54] Aqueous and microwave-assisted syntheses are known for the preparation of these CdTe_xSe_{1-x} quantum dots. [55, 56]

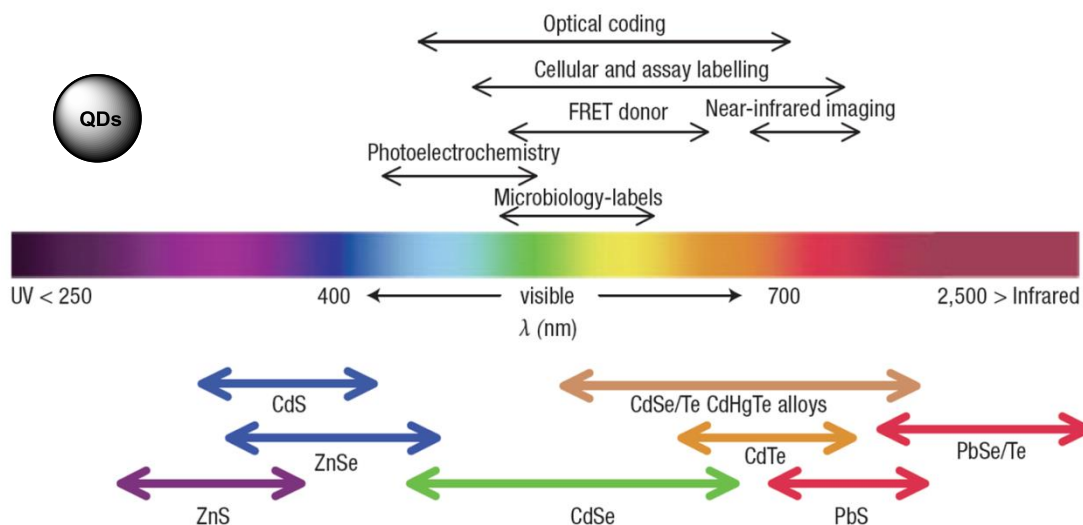


Figure 11: Quantum dot core materials and their emission wavelengths. Adapted from [57]

Semiconductor quantum dots (QDs) with high photoluminescence and narrow size distribution are versatile diagnostic and therapeutic tools for a variety of *in vitro* and *in vivo* bioapplications. [58] Due to their bright photoluminescence and their high photostability they have major advantages when compared to organic dyes. Nonetheless it should also be considered that upon functionalization of the QDs the hydrodynamic diameter of the particles increases and can have an effect the cell uptake.

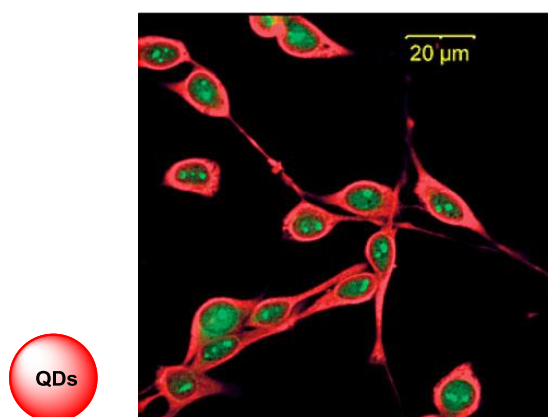


Figure 12: Confocal fluorescence microscopy images of cells incubated with quantum dots. Two different kinds of modified CdTe coloring nuclei (red) and cytoplasm (green). Adapted from [59]

In vitro they can be applied for labeling of cells or biomolecules and immunostaining. *In vivo* they can be used as vessels and for tumor imaging, visualization of the bio distribution of QDs and tracing of labeled cells in a body [60] and they are also applied for cell imaging (Figure 12). In contrast to organic dyes they are stable against photo bleaching (Figure 13). Fluorescein isothiocyanate (FITC) luminescence for example fades in color after only a few minutes whereas CdTe/CdS/ZnS quantum dots show luminescence for more than 30 min under the same irradiation conditions.

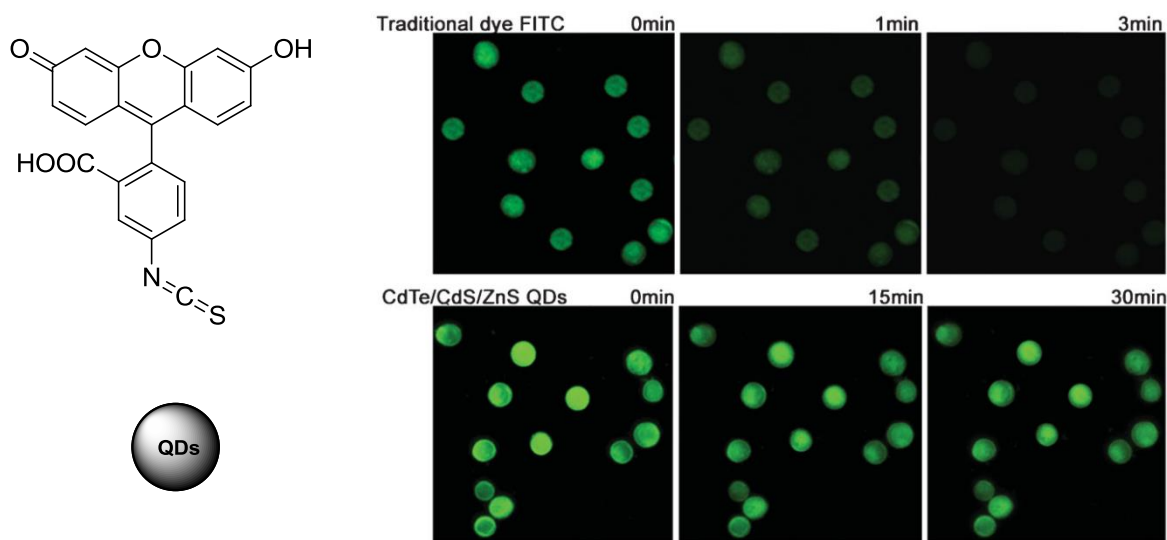


Figure 13: Photostability of a traditional dye compared to quantum dots. Adapted from [61]

QDs can also be linked to biomolecules such as antibodies, peptides or small molecules, allowing a highly sensitive and specific targeting or detection. [57]

Another important aspect for biological applications of QDs is their biocompatibility. Cadmium-based quantum dots can leak cytotoxic Cd^{2+} ions and have the tendency to aggregate, which are two major factors essentially for biocompatibility. Both can be prevented by a core-shell structure. Passivation of the bare QDs with a polymer coating or the growth of a ZnS shell can reduce the cytotoxicity. [62] Cytotoxic effects can not only result from the core material but also from ligands at the surface. [63] However there are also a number of studies where no cytotoxic effects of quantum dots were observed. [59]

2.4 Surface Functionalization

Surface functionalization of nanomaterials is an important topic of current research. The interaction of nanoscale materials with (biological) systems is mostly governed by the surface of the materials. Modifications of these can tune properties. Nanoparticles are well suited as templates for the immobilization of bioactive ligands, e. g. amino acids, peptides or enzymes, and their multiple presentations to receptors for a simultaneous binding. [64–66] Figure 14 shows a general scheme for the functionalization of nanoparticles.

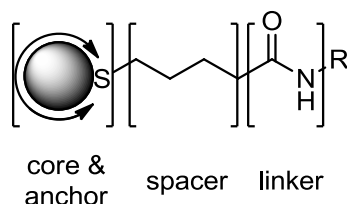


Figure 14: General scheme for the functionalization of nanoparticles.

Various core materials like noble metals (Au, Ag), quantum dots (CdTe, CdSe) or metal oxides (Fe_3O_4 , TiO_2) can be synthesized and applied as multivalent scaffolds. For both noble metal and semiconductor nanoparticles ligands with a sulfide anchor are often used due to their excellent stability. For iron oxide nanoparticles catechol-like ligands exhibit high stability. [67] The spacer between the nanoparticle and the active moiety usually consists of alkyl or polyethylene glycol chains, while the length of which may vary. The spacer must provide enough stability to the colloidal solution. Bifunctionalized ligands with both a moiety on one end anchoring at the nanoparticle and a free functionality at the other end offer an additional moiety for the further attachments of bioactive ligands. Functionalization of gold nanoparticles is mainly based on the work on self-assembled monolayers (SAMs) of molecules on planar gold surfaces. The dynamics and conformations of these assemblies have been studied intensively. [68, 69] A variety of functional ligands is available including thiolates, dithiolates, dithiocarbamates, amines, carboxylates, or phosphines. These molecules can be attached to the nanoparticle's surface via ligand exchange reactions. For stable conjugations thiol-based anchoring groups are favored.

It could be an advantage when the ligand used in the synthesis is only weakly bound to the surface. Citrate- or DMAP-stabilized gold nanoparticles are good precursors for these reactions, but also

thiol-stabilized gold nanoparticles can undergo an exchange. [25, 64, 70, 71] Even if gold nanoparticles synthesized with the method by *Turkevich* are only weakly covered by citrate, chloride ions and acetone dicarboxylate, the oxidation product of citrate, are also present. [72, 73] These species bind strongly to the surface and give certain stability to the colloidal solution. For a successful exchange ligands with stronger affinity to the gold surface must be used.

Schiffrin et al. described for the first time a two-phase synthesis of gold nanoparticles. Thiol-stabilized gold nanoparticles were synthesized in aqueous solution and transferred into an organic phase in a single synthesis step. [19] Monolayer protected nanoparticles smaller than 5 nm can be synthesized with this method. Thiol-gold interactions and van-der-Waals attractions stabilize the nanoparticles. Ionic and polymeric stabilization are much weaker. Through ligand-exchange reactions at the surface citrate-capped gold nanoparticles can be stabilized. However, upon chemisorption of thiolate ligands desorption of charged ligands like citrate sacrifices the electrostatic stability and can cause irreversible aggregation. [74]

Ligand exchange reactions at gold nanoparticles are carried out by adding an excess of thiolate ligands into the aqueous solution of the colloids. Suitable are ω -functionalized thiols, which offer both the ability to bind at the surface via the thiol moiety and stabilization via van-der-Waals interactions. Colloidal solutions with ligands which do not shield the nanoparticles properly turn steel blue in their optical appearance indicating particle aggregation. A two-step approach for the functionalization can be used. [70] Negatively charged ligands provide enough electrostatic stability whereas ligand exchange with neutral or positively charged ligands is critical and often results in aggregation of the colloidal solution. Especially mercaptocarboxylic (Figure 15) acids turned out to be excellent ligands. [75]

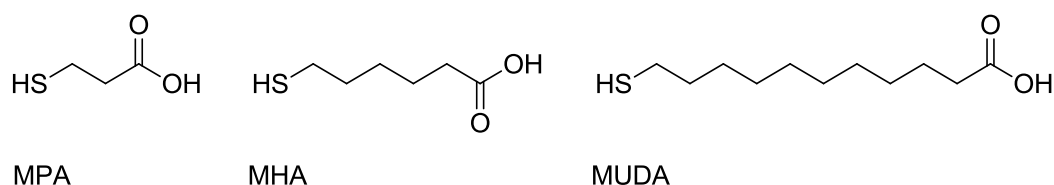


Figure 15: Mercaptocarboxylic acids for ligand exchange reactions.

Studies on the stability of gold nanoparticles showed that methylene chains from mercaptoacetic acid (thioglycolic acid, TGA) or mercaptopropionic acid (MPA) are too short and do not establish

enough steric stabilization for the colloids. [76] 6-Mercaptohexanoic acid (MHA) is still not sufficient, however 11-mercaptocarboxylic acid (MUDA) with its long alkyl-chain protects the surface sufficiently and stabilizes the nanoparticles, because it possesses more methylene units. [77] Vibrations C-H bond in the IR spectrum appears at 2918 cm^{-1} indicating a polymethylene monolayer of trans-zigzag chains. [78] This effect was also observed on gold surfaces with self-assembled-monolayers (SAM).

To obtain gold nanoparticles with short-chained ligands, other synthetic strategies must be selected. The biphasic reduction of a metal salt (HAuCl_4 or AgNO_3) with NaBH_4 and the addition of organic ligands give access to these colloidal solutions. [79, 80] Positively charged gold nanoparticles cannot be synthesized via ligand exchange reaction. The opposite charges interfere with each other and destabilize the solution. [70] This type of nanoparticles has to be synthesized directly from the precursor salts or via a two-step modification. [81]

The dynamic and mechanism of place-exchange reactions at the surface of gold nanoparticles has been studied intensively. Kinetic studies have revealed that either an associative $\text{S}_{\text{N}}2$ -like, a dissociative $\text{S}_{\text{N}}1$ -like or a combination of both takes place when long alkythiolate ligands are used. The rate depends on the concentration of the incoming ligand and decreases with the size of it. [71] Detailed ^1H NMR studies by *Murray* and coworkers examined the ligand exchange on monolayer protected gold clusters in dependence of concentration and ligand chain length and concluded an $\text{S}_{\text{N}}2$ -like associative mechanism. [82] Later, this was confirmed by *Montalti et al.*, who examined the kinetics of the release of a pyrene derivative from the surface via fluorescence spectroscopy. [83]

Through reactions at the ligand periphery bioactive molecules can be attached to the surface of the nanoparticles. The molecules are covalently bound to the ligand and stable against detachment. Depending on the free functional groups of ω -functionalized thiols at the nanoparticle's surface, there are a variety of reaction types possible (Figure 16). [84], [85] The synthetic methods require highly reactive species like active esters or nucleophiles but reaction conditions are always limited to the protection of the colloidal stability. The reaction between carboxylic acids and amino groups results in a very stable amide bond. This is a rather common method for the immobilization of biomolecules, because many of them possess a free amino group. MUDA-stabilized nanoparticles can be coupled directly in solution with the respective amine. Usually carbodiimide based agents are used for the activation of the carboxylate, followed by the reaction with *N*-hydroxysuccinimide. [86] Then the active ester reacts with the amine immobilizing the molecule via a covalent bond. This method can be applied for reactions both in aqueous and organic solvents.

Esterification between both alcohol and carboxylate functionality can also yield in a covalent attachment between bioactive molecule and ligand. [87]

Nucleophilic substitution at ω -functionalized halogen alkanes is also an approved strategy for the immobilization of bioactive molecules. As in organic synthesis the steric demand of the ligand directs the reaction to be S_N1 or S_N2 -like. [88] Another powerful synthetic method for incorporating bioactive molecules on the surface of nanoparticles is the 1,3-dipolar cycloaddition between azides and alkynes. Although these *click*-reactions are usually catalyzed by a Cu(I) salt, triazole formation can also occur at room temperature and uncatalyzed. [89]

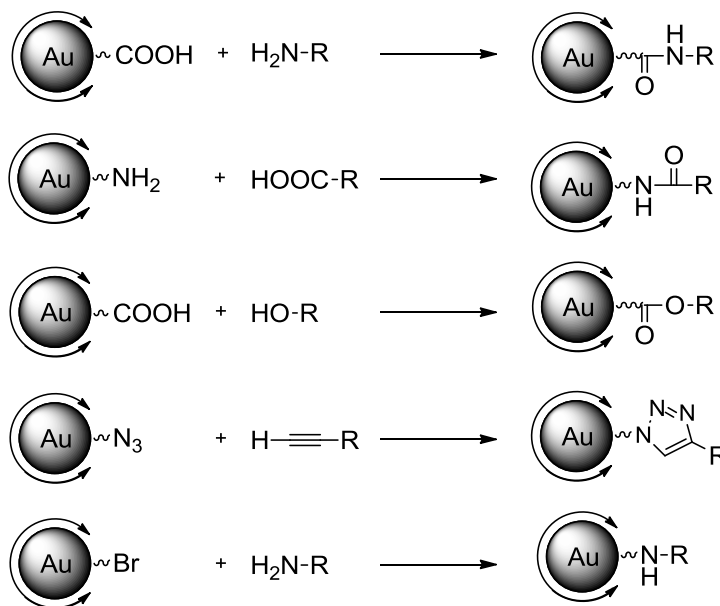


Figure 16: Different reaction types for covalent attachment of bioactive molecules.

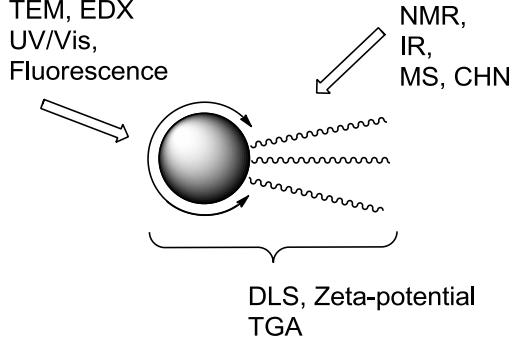
Besides covalent linkage of active molecules to the surface of nanoparticles also physical methods like hydrogen bonding and electrostatic or hydrophobic interactions can be used for the adsorption of molecules. This process plays an important role in protein and enzyme adsorption. [57] For example negatively charged DNA can be linked to gold surfaces via electrostatic interactions. [90, 91] Compared to covalently bound moieties, the stability of the resulting nanoparticles is weaker and strongly depends on the solvent, pH value, and ionic strength. Furthermore, the number of immobilized molecules can vary significantly.

In general functionalization depends on the type of molecule which is to be immobilized and the type of application. In some cases, for example drug delivery, a weakly bound ligand is favored. For all synthetic methods the molecules need to possess functional groups which are either already there or must be inserted through chemical modifications. Functionalized molecules can be qualitatively verified by a number of characterization methods, e. g. vibrational spectroscopy, thermogravimetric analysis, determination of hydrodynamic diameter and *zeta* potentials.

2.5 Characterization

There are different methods to characterize nanoparticles or colloidal solutions, generally all those which can be used for bulk materials. For functionalized nanoparticles with an inorganic core and an organic ligand shell, a technique can only characterize either core or shell. For a complete characterization a combination is necessary. The different methods for characterization used in this work are shown in Table 1. The precise determination of size, dispersity, state of aggregation and composition of the ligand shell is crucial for applications not only in biological media. For all techniques only small amounts in the nanomolar range are available and the method has to be sensitive enough to analyze these quantities.

Table 1: Summary of the nanoparticle characterization methods.

	Core		Shell	
	TEM	d_{core}	H NMR	δ_{H}
	EDX	composition	IR	ν_{bond}
	DLS	d_{hydr}	MS	m/z
	UV/Vis	λ_{abs}	ζ -potential	charge
	Fluorescence	λ_{em}		

For the characterization of the core size transmission-electron-microscopy (TEM) is mainly used. The mean core diameter of the nanoparticles can be determined. The sample is penetrated by a high energy electron beam which is scattered at the atoms of the core. High accelerating voltage and the

low wavelength of the electrons can lead to single atom resolution. For the measurement of biological samples the voltage needs to be lower to avoid destruction of the material. TEM measurements with lower resolution can give an overview of the sample and give a statistical distribution of the nanoparticles. High-resolution TEM can visualize single nanoparticles in structure and crystallinity. Lattice planes indicate crystalline materials and allow lattice parameter determination. Due to complex interference patterns the determination can be very complex. Elements with a high atomic number and therefore a heavy core like gold or silver have a high scattering rate and appear with high contrast, whereas organic compounds, like single ligands, mainly consisting of carbon do not appear. In addition, energy-dispersive X-ray emission spectroscopy (EDX) can be done to obtain the elemental constitution of the sample. For alloyed systems or mixed crystals the respective content can be determined using this technique.

Dynamic light scattering (DLS) gives the hydrodynamic diameter of the nanoparticles, where the volume of the whole nanoparticle including the core and ligand shell is determined, compared to TEM measurements where only the core diameter is measured. For ionic shells, coordinating solvent molecules can also be depicted. The method is nondestructive and can be assessed directly of the sample. DLS measurements give the average diameter of all the nanoparticles included in the sample, for a reliable result the nanoparticles should be monodisperse. Furthermore, the colloidal solution can be characterized by their surface potential. Streaming potential measurements indicate the charge at the surface.

Optical properties of nanoparticles can be determined with UV/Vis spectroscopy and fluorescence measurements. As mentioned above, the optical properties strongly depend on the shape of the nanoparticles. For metal nanoparticles the plasmon resonance causes the color appearance, quantum dots can either absorb or emit light with distinct wavelengths. Gold nanoparticles larger than 3 nm develop the characteristic plasmon resonance. The maximum shifts towards longer wavelength and therefore smaller energies for bigger nanoparticles. The position of the maximum can be used for the determination of the nanoparticle's size, the shape for the dispersity. Monodisperse colloidal solutions have a narrow absorption band. By comparison with reference solutions the concentration of the nanoparticles can be calculated. Anisotropic gold nanoparticles appear in different colors and possess more than one maximum. The optical properties of quantum dots also strongly depend on the size and shape. Besides absorption they also have an emission maximum when irradiated with a distinct wavelength. With fluorescence spectroscopy the size and size distribution can also be calculated. Another figure for high quality fluorophores is the quantum yield (QY). It is defined as the ratio between emitted and absorbed photons. QY below 100% means that some electrons in

excited states relax without radiation. It is drastically reduced by any kind of defect in the crystal lattice.

The ligand shell of the nanoparticles can be characterized with the same methods used in organic chemistry. NMR (nuclear magnetic resonance) and IR (infra-red) spectroscopy give information about the composition of the shell. The signals of immobilized ligands are typically broadened compared to the free ones. Broadening is caused by the chemical environment and the inhomogeneity of the shifts caused by tightly bound molecules. Close to the core the signals are even more broadened. [92] Due to only small concentrations of the particles mostly only proton NMR is recorded, for significant signals in carbon NMR analysis the concentrations are too low.

IR spectroscopy also characterizes the organic compounds of the nanoparticle. Both NMR and IR can monitor the surface and indicate changes after ligand exchange or coupling reactions. Characteristic vibrations of functional groups, e. g. S-H or C-H bonds or the carbonyl group in amide bonds, can help to identify the ligand.

Mass spectrometry can be used for the characterization of the single ligand before immobilized on nanoparticles. Depending on the reaction way the complete ligand can be synthesized separately, characterized and then attached to the surface. Elemental analysis also helps to characterize the organic compound.

The number of ligands can be determined with thermogravimetric analysis (TGA). The loss of weight depending on the temperature can be attributed to the amount of organic compound. With the diameter from TEM measurements, the assumption of a spherical shape and the molecular mass of the ligand, the number of ligand molecules can be calculated. This analysis needs a relatively large amount of sample.

2.6 Nanoparticles in Biological Systems

The synthesis and controlled functionalization of nanoparticles allows their application in biological systems. Due to the small size and large surface their properties are beyond the performance of previously used materials and offer new opportunities but also render them to unexpected interactions and unanticipated consequences. [93] Depending on the material, the application possibilities are widespread. For example, gold nanoparticles can be used for labelling, delivering,

heating and sensing [94] and quantum dots can be used as fluorescent markers for *in vitro* and *in vivo* imaging.

Traditionally, gold nanoparticles were used for visualization due to their strong interactions with light. Applied on tissue and enriched in areas of interest, they provide enough contrast.

Consideration should also be given to the toxicity of nanomaterials which is also a significant part in drug development and has to be elucidated carefully. The term nanotoxicology originated and describes the effects of nanomaterials on living tissues. Since to their size similar to biological components (cells, proteins) nanoparticles can interact at a cellular level. They also possess dynamic properties. Nanoparticles have the ability to move in the system allowing a wide distribution, but they also have the ability to build agglomerates, which are less mobile. Through functionalization of the ligand shell stabilization in biological media can be achieved. Liposomes, polymeric nanoparticles and gold nanoparticles have already found their way into medicine as powerful carrier systems. [95–98] The first FDA-approved nanodrug was Doxil®, a liposome based nanocarrier. [99] Iron oxide nanoparticles are already approved as MR imaging agent and targeted polymeric nanoparticles entered clinical trials. In the second generation of nanomedicine nanoparticles were developed for specific ligand targeting of organs, tissues, or cells. The ligand is presented at the surface of the carrier, which is accumulated at the site of action. [100] Third-generation nanoparticles act at the subcellular and organelle-level. [101] Ligand-functionalized nanoparticles are the focus of current research and have a huge potential application.

Biofunctionalized nanoparticles can overcome natural barriers in organisms, e. g. biological membranes, skin, lung, or the blood-brain barrier. Like small molecules they can diffuse through the lipid bilayer depending on size, shape, and charge. This can be used in therapeutic applications and medical diagnostics, but the nanoparticles need to have efficient binding, biocompatibility, and long-time safety. [102] Transport across a membrane can either proceed in vesicles, mostly found for oxidic nanoparticles, or directly without modification. The charge and *zeta*-potential of the nanoparticles have a vast effect on the cell uptake. Solubility of the nanoparticles in the biological medium is decisive for average residence time in the organism. Depending on the size and composition nanoparticles can enter the cell by different endocytic pathways. There are several internalization mechanisms like phagocytosis, macropinocytosis, and clathrin- and caveolae-mediated endocytosis. [103] The processes are triggered by cell-surface receptors either targeted directly by the nanoparticle or indirectly by effective molecules (e. g. growth factors). When the nanoparticle is incorporated in a vesicle, the natural digestion mechanism starts. Phagocytosis engulfs foreign particles and disables the pathogen. This process is a natural defense mechanism in

organisms. Furthermore pinocytosis is also a pathway for materials entering eukaryotic cells. [103] Through lysosomes and phagocytosis the nanoparticle is infiltrated into the cell, where the pH value is lower. Depending on their chemical properties, oxidic and metallic nanoparticles are not stable under acidic conditions and toxic ions can be released. Heavy metal ions in the cytosol cause stress and have an influence on production and activation of reaction oxygen species (ROS). [104] Through passivation of the core with polymers or zinc oxide, this can be prevented. For the development of nanocarrier systems an in-depth understanding of cellular uptake is of great importance.

2.7 Multivalent Ligands

Multivalency is a key interaction in biological systems. [105] It means polyvalent interactions in (biological) systems and often results in an amplification of binding strength. Multivalency is the simultaneous interaction of multiple ligands on one entity with multiple receptors on another. The valency of a particle is determined by the number of separate active moieties. This concept plays a central role in recognition processes, self-assembly of matter and in signal transduction pathways. The recognition element on the central scaffold can be a carbohydrate, peptide, protein or small molecule, any moiety binding to the receptor. The scaffold defines the geometric features of the multivalent ligand, e. g. shape, size, orientation, flexibility and valency. Nanomaterials provide a versatile platform for immobilization of bioactive molecules. Due to the high surface-to-volume ratio a multitude of molecules can be assembled on them. For the immobilization of effector molecules, a central particle is needed. Several inorganic and organic scaffolds belong to the class of nanomaterials: dendrimers, fullerenes, liposomes, SPIONS, Au NP, polymer NP, QDs, nano hollow spheres, or self-assembled peptides.

Multivalent ligands can act as effectors or inhibitors of biological processes. The terms are different to bioactive monovalent molecules which are often referred to as agonists (activating) or antagonists (inhibiting). High functional affinities and binding part density can result in an amplification of the effect. The potency of a multivalent ligand can depend on the mechanism of interaction (Figure 17). For monovalent ligands single site receptor binding or hetero dimerization are typically found. In multivalent presentation there are different interaction modes between ligand and receptor. For example, natural occurring multivalent vaccines are able to cluster cell surface receptors and have a high effectiveness. The inhibitory activity of pentameric *Shiga*-like toxins derives from the ability to occupy multiple binding sites. Steric stabilization is given when the size

ligand prevents further interactions. Subsite binding and chelating effects are secondary binding effects in regions of the receptor different to the primary binding site. Statistical effects can also occur when rebinding of the multivalent ligand is favored through high local concentration. [106, 107] Different binding modes can result because of the structural complexity of multivalent ligands. There are many biological systems in which multivalency plays a crucial role. Understanding the molecular features that influence the binding can help to develop new systems.

The scaffold structure mainly determines the effects on activity. Small multivalent scaffolds may not be capable of spanning a large distance between several receptors but may effectively occupy multiple subsites.

Receptors are usually proteins embedded in cell surfaces and transmit information from outside into the inside of a cell. Signal transduction is predominantly mediated by ligand-gated ion channels. Many receptors act as part of oligomeric complexes and the interaction with multiple ligands may have an effect on signal transduction. Multivalent ligands provide new opportunities for the activation or inhibition of receptor interactions. [108] The valency and orientation of recognition sites and the stability of the resulting complex can influence the interactions. [109]

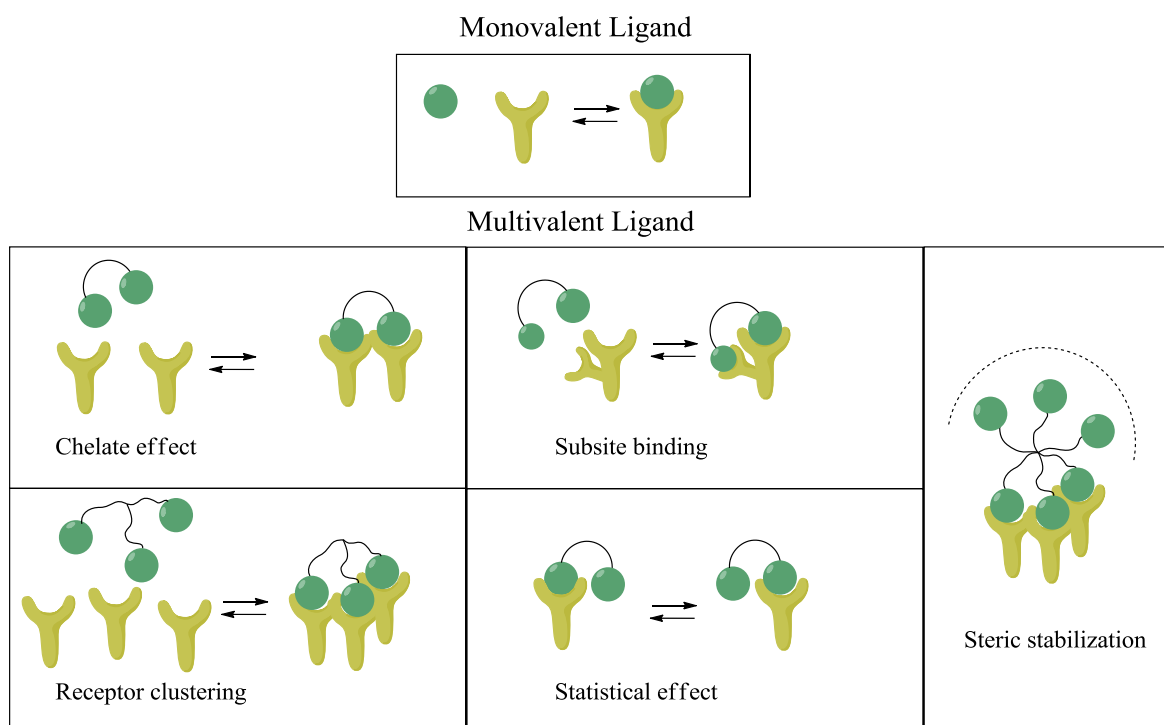


Figure 17: Different mechanisms of binding with monovalent and multivalent ligands.

Nanoparticles offer a versatile platform for multivalent action. When functionalized with ligands including both a bioactive moiety and an anchor for the surface they are a highly multivalent system. Size, shape and physical properties can be selectively adjusted. For example multivalent presentation of carbohydrate mimetics on gold nanoparticles for selectin inhibition exhibited IC_{50} values in picomolar range with high selectivity. [110]

Although nanoparticles with terminally functionalized ligand shells are used for a large number of applications in the life sciences gold nanoparticles have only been used as multivalent ligands for the presentation of bioactive amines in receptor binding interaction. [111]

3. Motivation and Goals

Due to their similar size to biological systems, e. g. enzymes or receptors, nanoparticles are interesting tools for studying the interaction with each other. Functionalized nanomaterials might help to answer fundamental questions in biochemical and cell biology to understand molecular mechanisms and might also find their way into medicinal applications. The behavior of nanomaterials in biological systems is still not completely understood and currently under investigation.

These nanomaterials, especially nanoparticles, can be functionalized with simplified binding moieties of biologically active compounds. This type of functionalization implies a multivalent presentation allowing polyvalent interactions between ligand and receptor. The concept of multivalency proved to have special effects in biological interactions. The newly developed conjugates possess different properties compared to monovalent analogues. Besides studies on the multivalent interactions of natural molecules, e. g. carbohydrates or selectin inhibitors, only little is known about the interactions of neurotransmitters multivalently presented to their receptors. Neurotransmitters belong to an essential class of natural products and represent an appealing class of small molecules for immobilization on nanomaterials. These molecules are endogenous chemicals which enable transfer of information in biological systems. They are chemical messengers transmitting a signal. Their biosynthesis is rather simple and they are readily available in living organisms. There are different types of neurotransmitters, e. g. amino acids, peptides or amines. Investigations are to be focused on biogenic amines. Histamine, dopamine and serotonin are only three examples with important functions in the central nervous system. All neurotransmitters have distinct receptors for signal transductions. These native amines act as agonists activating a receptor response. Their monovalent ligand-receptor interactions are well studied and understood.

Gold nanoparticles proved to be versatile tools for the application in biological systems due to their high biocompatibility. The surface can easily be modified and furthermore, size and shape of the nanomaterials can be adjusted during synthesis. By the determination of the size, the number of free active moieties can be varied.

In this work gold nanoparticles are to be synthesized, functionalized and fully characterized. Different synthetic approaches can be used to obtain various core sizes, yet water solubility and stability must be ensured. Subsequently these nanoparticles should be functionalized with the

biogenic amines mentioned above. It has to be tested, which core sizes are suitable for application. The effect of these newly developed conjugates on the ligand-receptor interactions should be studied. Therefore a cooperation project between chemistry and veterinary medicine will be established, where the biological functionality of the gold nanoparticles can be tested. These results can be compared to the effects of the native amines. Immobilization of the amines also involves a loss of recognition attribute as the amino group will be bound to the nanoparticles. But simplification of binding moieties is also common in multivalent presentation. As there is no information about multivalent contribution in these interactions, these investigations can give new insights in this phenomenon. Depending on the results the scaffold and geometry of the components can be improved. The particular aim is the development of new nanoscaled materials for medical application.

Besides the interaction of gold nanoparticles in biological systems another class of nanomaterials is to be investigated. Quantum dots of low nanometer scale are able to penetrate biological barriers and can be used for cell imaging. The physical properties of these materials are size- and shape-dependent, which can be precisely adjusted during the synthesis. Optical characteristics like emission and absorption ability of different quantum dots should be investigated and improved, as these are important for upcoming use. The quantum dots can be applied as cell dyes and the cellular uptake can be studied. Additionally, the synthesis should be followed by surface functionalization with bioactive amines. Fluorescence microscopy can be used for a visualization of the behavior in biological systems.

4. Gold Nanoparticles

4.1 Syntheses of Gold Nanoparticles

In this work various gold nanoparticles with a nearly spherical shape were synthesized using different gold precursor materials. The size of the nanoparticles varies between 4 nm and 25 nm and they are either already water soluble or dispersed in an organic solvent. Three different synthetic approaches were chosen to obtain nanoparticles with different diameters. For biomedical applications a uniform size is required. Thus the size distribution of the resulting particles should be very narrow. Additionally, the colloidal solution must be stable in water and under physiological conditions. Therefore ligand exchange reactions have to be performed. The size of the colloids can be adjusted from smaller to larger spheres depending on the reaction conditions. Figure 18 gives an overview of the synthesized gold nanoparticles from 4 nm to 25 nm obtained by different synthetic approaches.

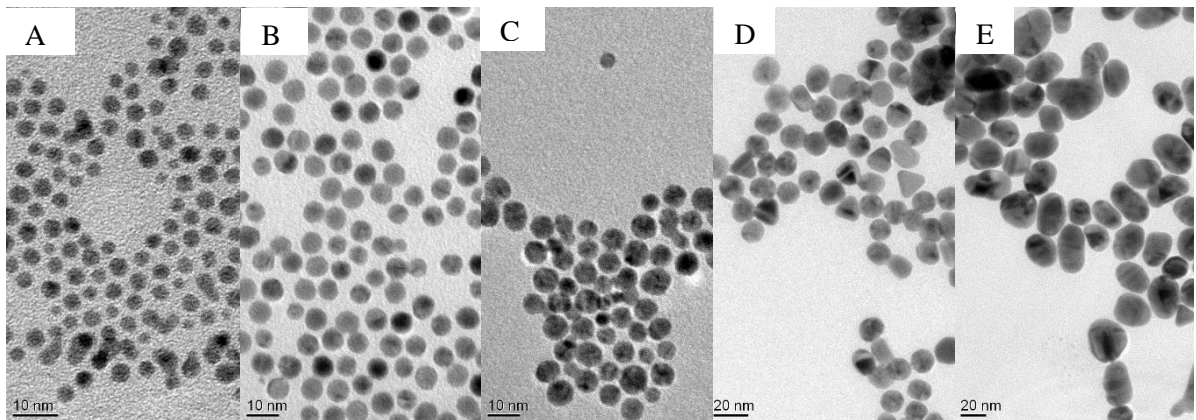


Figure 18: TEM images of colloidal gold nanoparticles with different sizes synthesized via the *Stucky* approach (A, B), the *Brust-Schiffrin* method (C) and the *Turkevich* method (D, E).

The most popular and frequently used concept for the synthesis of gold nanoparticles is the reduction of tetrachloroaurate AuCl_4^- in aqueous solution using NaBH_4 or trisodium citrate. This method provides gold nanoparticles which are already water soluble. First published by *Turkevich* in 1951 and improved by *Panigrahi et al.* these gold nanoparticles were synthesized size-selective. [16], [112]

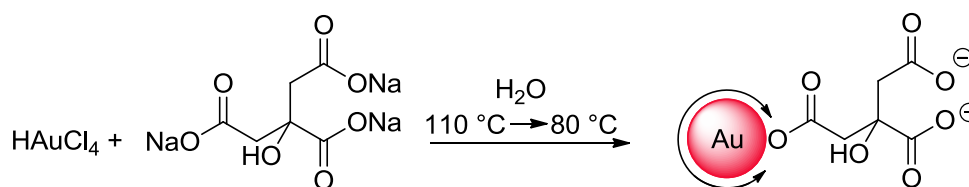


Figure 19: Reaction scheme for the synthesis of citrate-stabilized gold nanoparticles.

For the synthesis $\text{HAuCl}_4 \cdot 3 \text{H}_2\text{O}$ was dissolved in ultrapure water and heated up to 110°C (Figure 19). Under vigorous stirring a solution of trisodium citrate was added at once and the mixture was stirred at 80°C . The reaction time and the molar ratios of Au(III) and trisodium citrate determined the size of the resulting particles, less reduction agent gave bigger nanoparticles. The reaction volume was kept at 50 mL for each synthesis. Trisodium citrate serves not only as a reducing agent but also as the stabilizing ligand. The formation of the nanoparticles in solution can be monitored by the change of the color from pale yellow over greyish after a few minutes to final red. After a certain time the solution was cooled down with an ice bath to stop the reaction. Three different reactions were performed via this approach yielding three different sizes (Table 2).

Table 2: Reaction conditions for the synthesis of Au-Citrate nanoparticles in aqueous solution. [112]

d_{expected}	$n(\text{HAuCl}_4)$	$n(\text{Na}_3\text{Cit})$	Au:Lig	T	t
8 nm	12.5 μmol	76 μmol	1:6	110°C	30 min
14 nm	12.5 μmol	50 μmol	1:4	110°C	30 min
25 nm	12.5 μmol	28 μmol	1:2	110°C	30 min

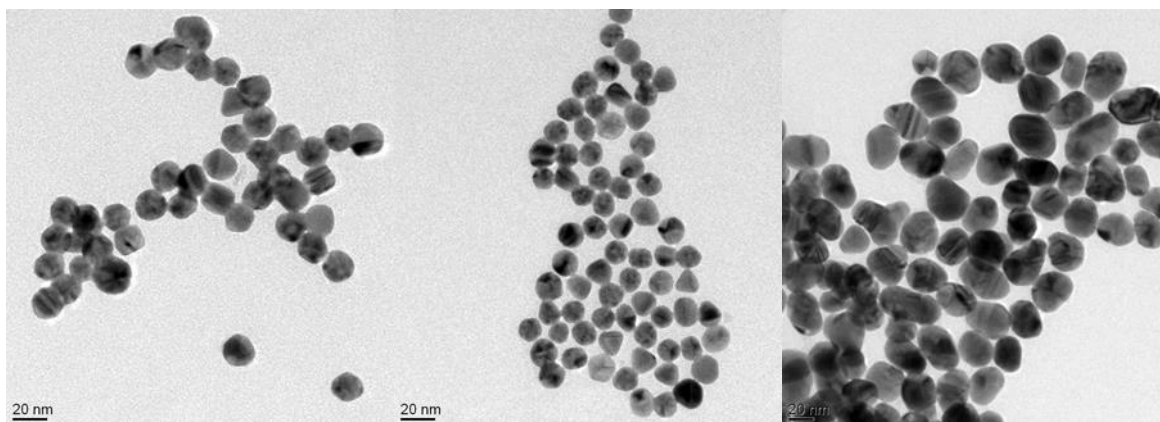
The size of the gold nanoparticles was characterized by TEM and DLS and summarized in Table 3. All synthesized gold nanoparticles are mostly of a spherical shape with an average size distribution. The larger particles of 25 nm and 14 nm diameter were reproducible with respect to the literature; only the smaller particles with a diameter of 8 nm could not be synthesized successfully. To obtain gold nanoparticles from the citrate reduction a reversed addition of the compounds is needed. [113] The hydrodynamic diameter is slightly larger than the core diameter determined by TEM due to the ligand shell and coordinated solvent molecules.

Table 3: Three different gold nanoparticles synthesized through reduction of HAuCl_4 with different amounts of $\text{Na}_3\text{Citrate}$. TEM and DLS values are given for the determination of the core size. Scale bar is 20 nm.

$d_{\text{expected}} = 8 \text{ nm}$

$d_{\text{expected}} = 14 \text{ nm}$

$d_{\text{expected}} = 25 \text{ nm}$



TEM: $d = 17.4 \pm 1.2 \text{ nm}$

TEM: $d = 14.0 \pm 0.9 \text{ nm}$

TEM: $d = 25.3 \pm 2.4 \text{ nm}$

DLS: $d = 19 \pm 6 \text{ nm}$

DLS: $d = 16 \pm 3 \text{ nm}$

DLS: $d = 26 \pm 10 \text{ nm}$

Smaller gold nanoparticles can be synthesized via the *Stucky* method. $\text{Au}(\text{PPh}_3)\text{Cl}$ and 1-dodecanethiol were used in different ratios and different solvents (Figure 20). [26] This method gives access to nanoparticles smaller than 10 nm dispersed in organic media. Two different sizes were prepared and the substitution of benzene through toluene was investigated.

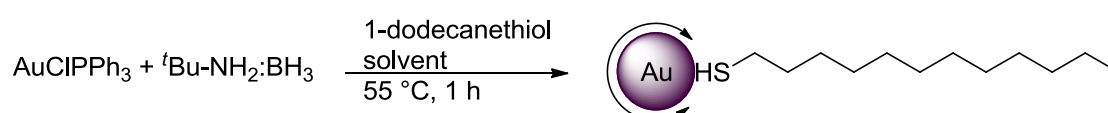
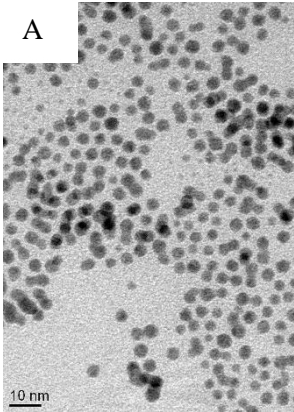
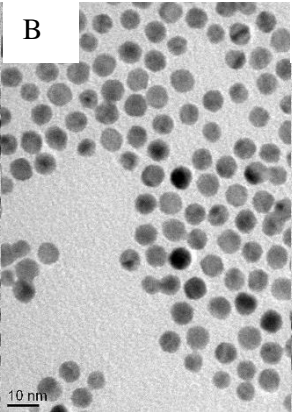
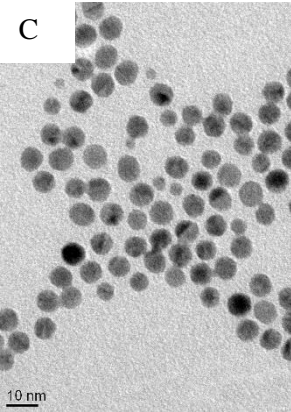
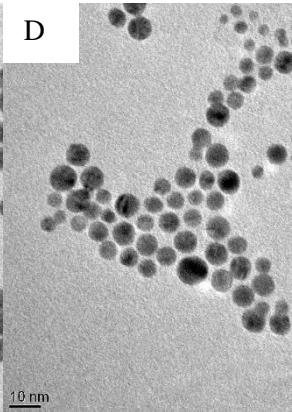


Figure 20: Reaction scheme for the synthesis of dodecanethiol-stabilized gold nanoparticles in organic solution.

All syntheses were carried out under atmospheric conditions. The gold precursor was dissolved with the capping ligand in chloroform or benzene, heated up to 55°C and then the amine-borane complex was added. The resulting gold nanoparticles are summarized in Table 4, A-C. All three types are monodisperse with a narrow size distribution and nearly perfectly spherical. This can be explained by the use of the amine-borane complex. Compared to commonly used reducing agents like NaBH_4 this is a milder alternative. The reducing ability is weaker and the formation process is slowed down resulting in a constant growth. [26] This process is visible in the color change of the reaction mixture and is much slower than in the citrate reduction. At lower temperatures small gold nanoparticles of 4 nm can be synthesized. The slightly bigger 6 nm gold nanoparticles were synthesized in benzene. The substitution of toxic benzene by toluene

results in monodisperse 7 nm gold nanoparticles. Characterization was done with TEM microscopy and DLS measurements. All gold nanoparticles synthesized via this method are dispersed in organic solvents and a phase transfer into aqueous solution must be done afterwards.

Table 4: Different gold nanoparticles were synthesized in different organic solvents. TEM and DLS values are given for the determination of the core size.

$d_{\text{expected}} = 4 \text{ nm}$	$d_{\text{expected}} = 6 \text{ nm}$	$d_{\text{expected}} = 7 \text{ nm}$	$d_{\text{expected}} = 6 \text{ nm}$
A	B	C	D
			
TEM: $d=3.8 \pm 1.3 \text{ nm}$	TEM: $d=6.4 \pm 0.4 \text{ nm}$	TEM: $d=7.2 \pm 0.4 \text{ nm}$	TEM: $d=6.0 \pm 1.5 \text{ nm}$
DLS: $d = 5 \pm 0 \text{ nm}$	DLS: $d = 13 \pm 2 \text{ nm}$	DLS: $d = 12 \pm 2 \text{ nm}$	DLS: $d = 35 \pm 10 \text{ nm}$
Chloroform	Benzene	Toluene	Toluene/Water

A third method for the preparation of gold nanoparticles was performed in a two phase liquid-liquid system via the *Brust-Schiffrin* method. [19] Using the phase transfer agent TOAB AuCl_4^- ions were transferred into an organic phase where they were reduced with NaBH_4 and stabilized (Figure 21). With DMAP the gold nanoparticles were transferred back into the aqueous phase. [114] The resulting gold nanoparticles were about 6 nm in diameter, spherical but rather disperse in size and prone to agglomeration (Table 4, D).

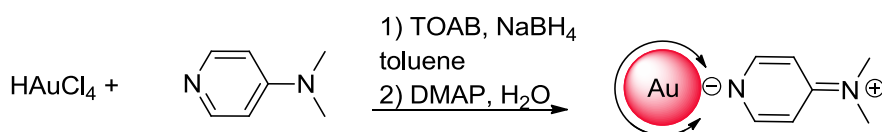


Figure 21: Reaction scheme for the biphasic synthesis of DMAP-stabilized gold nanoparticles

Nevertheless these gold nanoparticles are good precursors for ligand exchange reactions due to the weak interactions of ligand and surface.

4.2 Optical Properties

Figure 22 gives an overview of the UV/Vis absorption spectra of the colloids, measured in quartz cuvettes. Spherical gold nanoparticles exhibit a characteristic surface plasmon band around 520 nm induced by the collective oscillation of electrons in the conducting band. Depending on the size of the nanoparticles the absorption maximum can shift. The characteristic plasmon resonance band can be seen in all synthesized sizes. The gold nanoparticles of 6 nm and 7 nm size cannot be distinguished in the spectra; they show no difference in the position of the maximum.

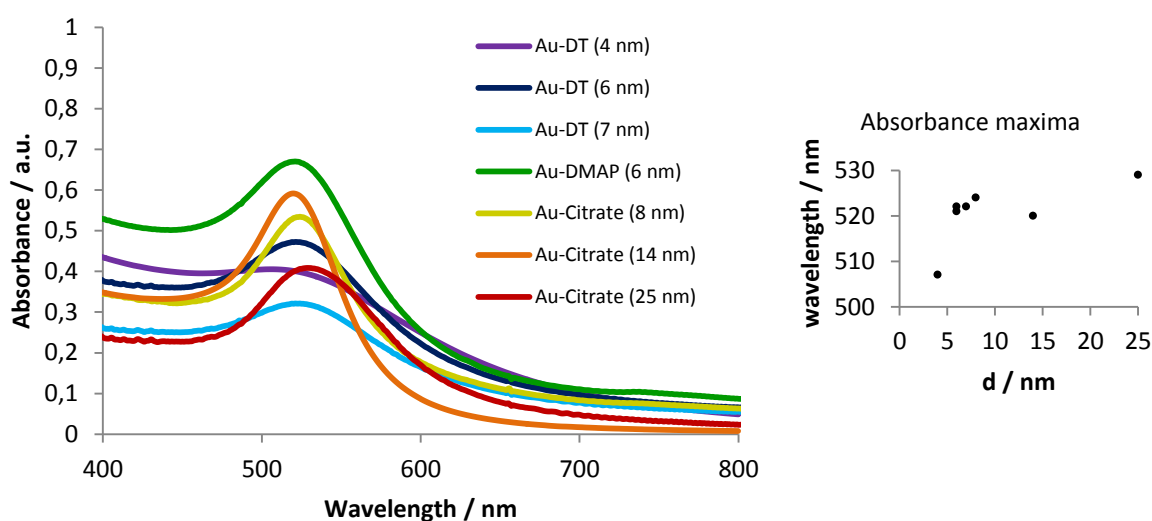


Figure 22: UV/Vis absorption spectra of all gold nanoparticles synthesized. For bigger nanoparticles the maximum of the plasmon resonance shifts to longer wavelengths (inset).

Only for the 4 nm gold nanoparticles is the shape of the absorption spectrum different (Figure 22). The maximum is not as distinct as for the other particles. For small nanoparticles no plasmon resonance can be observed.

4.3 Alloyed Metal Nanoparticles

Besides these gold colloids also silver nanoparticles were synthesized in aqueous solution. Again citrate reduction of the metal salt was performed (Figure 23). To prevent the formation of the insoluble AgCl precipitate all educts have to be added quickly. Alloyed nanoparticles of Au and Ag can also be synthesized via this method by co-reduction of both the gold and silver precursor salts. [115] [116, 117] Co-reduction of the precursor salts gives simple access to different compositions and the elements are equally distributed.

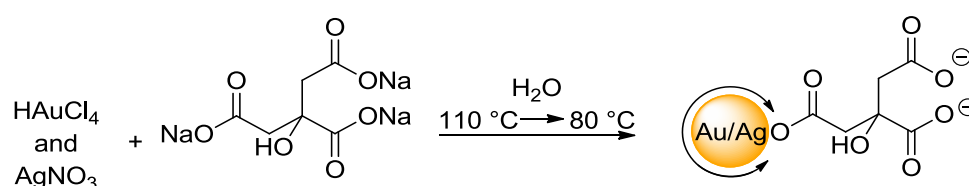


Figure 23: Reaction scheme for the synthesis of alloyed nanoparticles with the citrate reduction route.

Optical properties of the alloyed nanoparticles are plotted in Figure 24. The absorption maximum shifts from 521 nm for pure gold nanoparticles to 413 nm for pure silver nanoparticles corresponding to the surface plasmon resonance respectively; the particle size is nearly the same for all different particles. The maximum shifts linearly in dependence of the molar ratios of Au and Ag indicating a constant distribution of both elements.

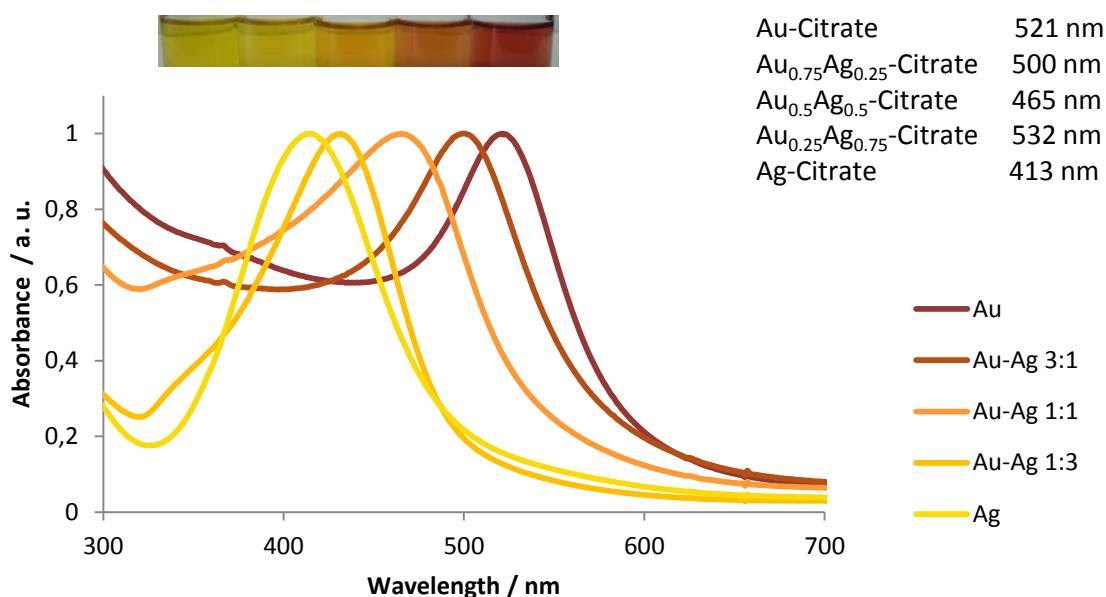


Figure 24: UV/Vis absorption spectra of Au/Ag alloy nanoparticles. The photograph shows the colloidal solutions. The maxima of the plasmon resonance shift linearly between both Au and Ag nanoparticles. The spectra are normalized for a better comparison between the different alloys.

4.4 Ligand Exchange Reactions at Gold Nanoparticles

After the synthesis of the gold nanoparticles ligand exchange reactions were performed. Ligand exchange reactions offer an effective way to modify the properties of nanoparticles such as solubility and stability. For biological applications they need to be stable at physiological conditions meaning water-solubility and pH stability. As the ligands used in the syntheses cannot be functionalized with biomolecules they must be exchanged by different ligands giving both stability and an anchor for further linkage to biomolecules.

Water soluble gold nanoparticles coated with mercaptocarboxylic acids are well-known and versatile for the preparation of multivalent species. [110] The particles can either be obtained by simple ligand exchange starting with Au-Citrate nanoparticles or can be synthesized directly in solution by the reduction of gold(I) or gold(III) salts with suitable ligands. Using the second approach the core size of the nanoparticles can be tuned during the synthesis, but also the size of Au-Citrate nanoparticles can be varied between 3 nm and 60 nm and the size distribution is excellent. [112] Au-Citrate nanoparticles are known to be excellent precursors for ligand exchange reactions but also Au-DMAP and Au-DT exhibit those characteristics. [118]

The gold colloids were stirred at room temperature under atmospheric conditions and the new ligand was added in large amount, while the pH was controlled and held constantly over 8. The

stability of the nanoparticles in solution is extremely affected by the ligands on the surface. There is a risk of aggregation during ligand exchange reactions. A typical reaction is shown in Figure 25. The ligand is added to the nanoparticles solution in excess and the exchange is performed for at least 16 hours at room temperature. The progress of the reaction can be monitored by UV/Vis spectroscopy. Within a ligand exchange the maximum slightly shifts between 2 nm and 5 nm. This is due to the change in dielectric permittivity of the gold nanoparticles caused by the formation of the thiolate monolayer. [119]

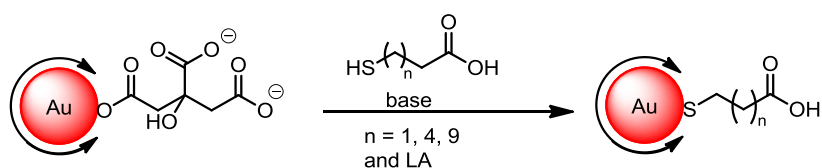


Figure 25: Reaction scheme for the ligand exchange at citrate-stabilized gold nanoparticles with mercaptocarboxylic acids.

The exchange of the citrate ligand by the respective mercaptocarboxylic acids proceeds completely due to the stronger affinity of the thiol moiety to the gold surface and the huge reactant excess. The binding strength between O and Au is more like an electrostatic interaction whereas S and Au form covalent-type bonds. The thiol ligand is bound very tightly on the surface. [75, 120] The stability of the nanoparticles strongly depends on the spacer length. 11-Mercaptoundecanoic acid (MUDA) appeared as a very suitable ligand due to its capability of shielding the core with its flexible chain. The fatty acid chain presumably surrounds the surface, forms a monolayer assembly and stabilizes the nanoparticles. This ability decreases with shorter chain length. With 6-mercaptohexanoic acid (MHA) the stability in aqueous solution is still given but the shortest ligand 3-mercaptopropionic acid (MPA) does not stabilize the particles enough under the reaction conditions of the ligand exchange.

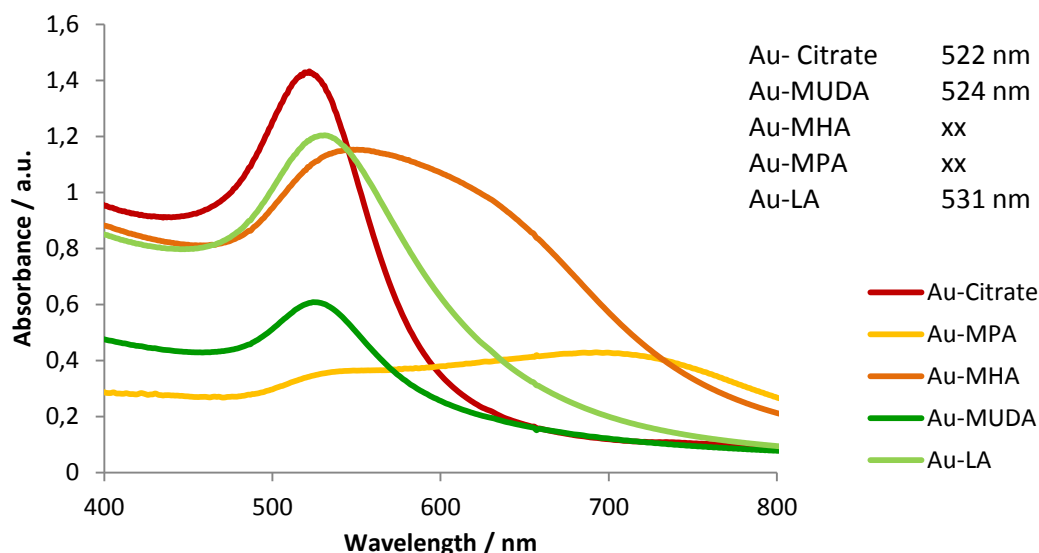


Figure 26: UV/Vis absorption spectra of gold nanoparticles stabilized different ligands compared to Au-Citrate are shown. For short chained ligands MHA and LA no stable solution could be obtained.

In Figure 26 the UV/Vis spectra of both Au-Citrate 14 nm and the gold nanoparticles with the respective ligands are shown. For Au-Citrate the maximum appears clearly at 522 nm. It shifts to 524 nm after the ligand exchange with MUDA. The resulting gold nanoparticles are stable under atmospheric conditions. For the shorter ligands with a chain length of three and six carbon atoms no stable dispersion in water could be achieved with the *in situ* exchange. In both spectra no maximum of the plasmon resonance is observable indicating aggregation of the nanoparticles. A black precipitate is formed which is also visible with the naked eye. Only for MHA-stabilized nanoparticles is a slight absorbance indicated but no stabilization of the particles could be achieved. In addition a ligand with a disulfide anchor was also tested. Lipoic acid (LA) contains two thiol moieties which can be attached at the surface giving more stability for the nanoparticles. A stable colloidal solution with a maximum at 531 nm could be synthesized via the ligand exchange protocol.

Ligand exchange reactions with MUDA at gold nanoparticles with different core sizes were performed. The smaller 4 nm and 7 nm gold nanoparticles were transferred into aqueous solution via two-phase ligand exchange reaction, the bigger 14 nm and 25 nm gold nanoparticles were already dispersed in water and only modified at the surface. All kinds of nanoparticles are stable in aqueous solution and no agglomeration is observable indicated by the plasmon resonance maxima (Figure 27).

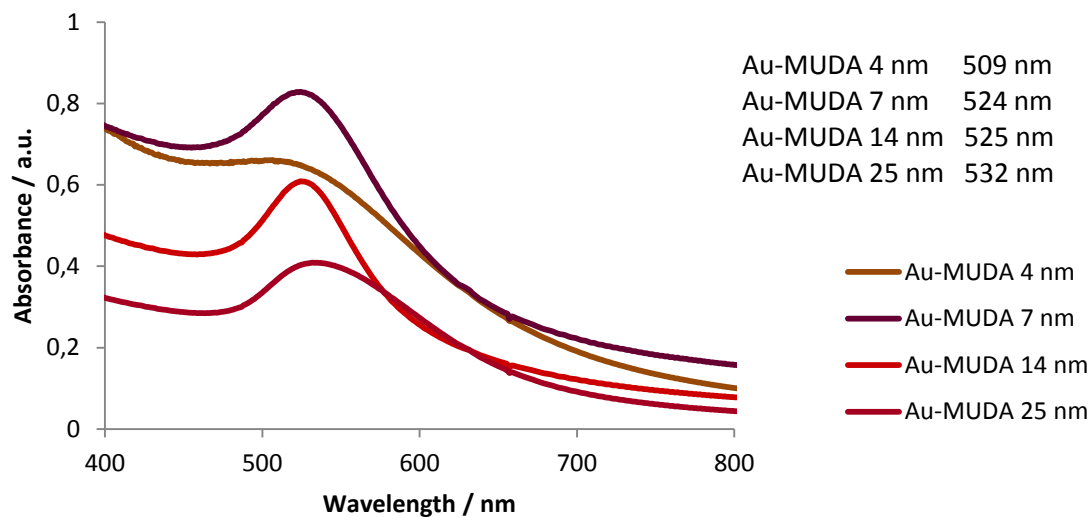


Figure 27: UV/Vis absorption spectra of gold nanoparticles with different sizes after the ligand exchange reaction with MUDA. All colloidal solutions are stable.

Silver nanoparticles and the alloyed compounds were also tested in the ligand exchange with MUDA. Again a red shift for the absorption maxima can be observed. The maxima shift linearly between both pure gold and silver nanoparticles.

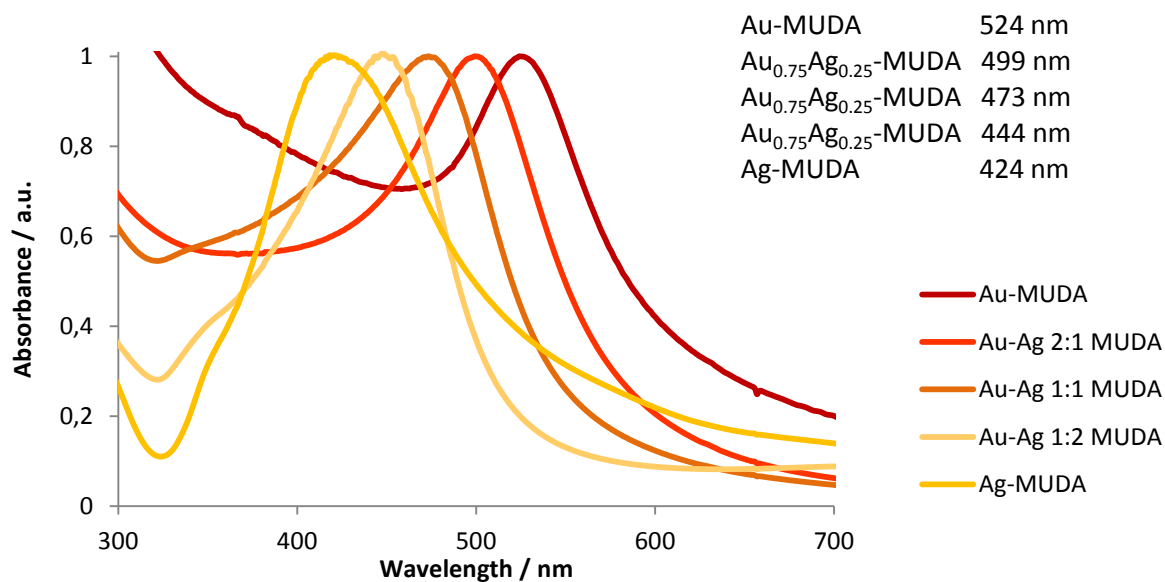


Figure 28: UV/Vis absorption spectra of Au/Ag alloy nanoparticles after the ligand exchange with MUDA. All colloidal solutions are stable. The spectra are normalized for better comparison between the different alloys.

Since MUDA-stabilized gold nanoparticles show excellent stability, a ligand with similar chain length but a terminal alcohol group was also tested. Unfortunately, 11-mercaptoundecanol (MUDOL) is only barely soluble in water even under basic conditions and the resulting gold nanoparticles agglomerate immediately. The absorption spectra show the differences at the plasmon resonance maximum (Figure 29). However with a sulfated hydroxyl group the solubility and stability of the gold nanoparticles in water is good. Within two steps 11-mercaptoundecanol can be sulfated (MUDOLS) with $\text{SO}_3\cdot\text{DMF}$ in good yields and coupled to the surface of gold nanoparticles (see publication chapter 4.10).

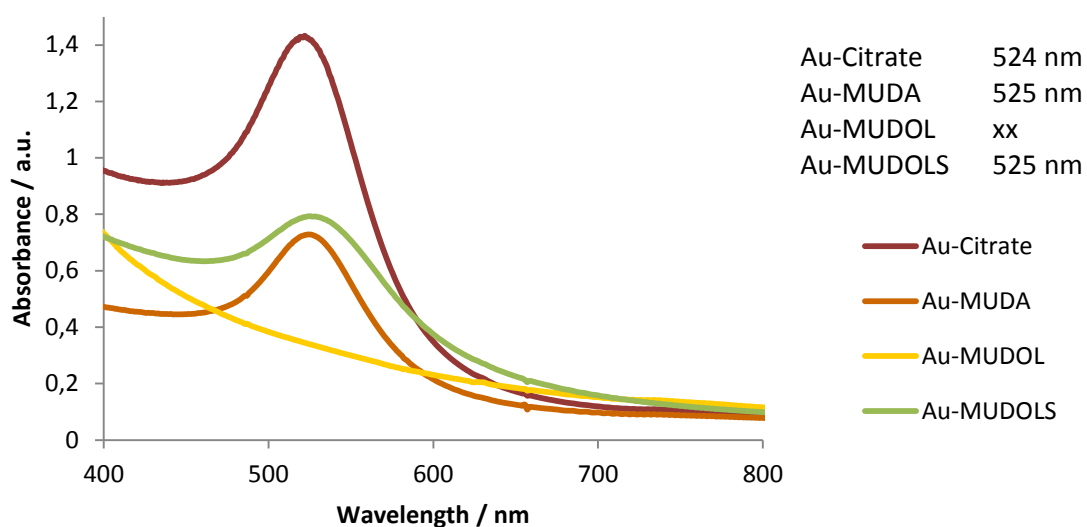


Figure 29: UV/Vis absorption spectra of gold nanoparticles after the ligand exchange with MUDA, MUDOL and MUDOLS. No stable solution of alcohol-terminated nanoparticles could be obtained.

Three different sizes of gold nanoparticles were synthesized with MUDOLS at the surface. After the ligand exchange the plasmon resonance of all three types is still visible and red shifted compared to the precursor (Figure 30). The colloidal solution is stable in water.

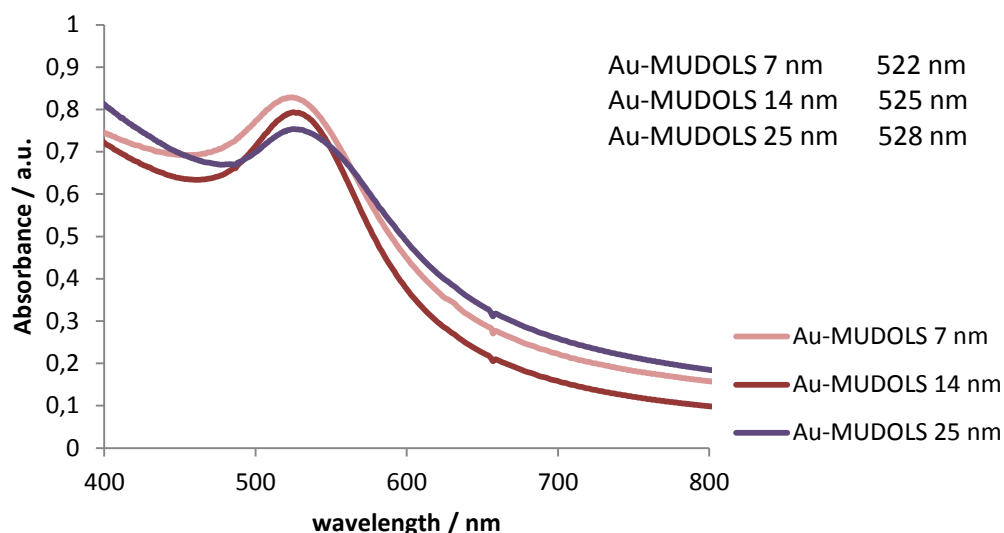


Figure 30: UV/Vis absorption spectra of gold nanoparticles with different core sizes after the ligand exchange with MUDOLS. All colloidal solutions are stable.

Besides MUDA also LA anchoring with two sulfur atoms at the surface showed good colloidal stability. Following the idea to stabilize the nanoparticles with a bidentate anchor the dithiocarbamate (DTC) linker is a useful ligand. Due to its simple synthesis it gained attention for the functionalization of metal nanoparticles. It is formed *in situ* from CS_2 and an amine and can be directly coupled to the gold nanoparticles. [121] DTCs are unstable in their acidic form and are often prepared as metal salts under strong basic conditions. [122] Primary as well as secondary amines can condense with CS_2 . The ligands have a stronger affinity to gold surfaces and form stable conjugates. [123] Thus this method allows for a wide variety of conjugation with biomolecules containing an amine moiety. The method has been used for dopamine functionalization of gold nanoparticles which can be applied in sensing, detection and quantification of small molecules. [124], [125] Not only gold nanoparticles but also quantum dots can be functionalized in the same way with this method. [126] Compared to the previously used alkyl chained linker this can be seen as a *zero-length-linker* which binds the biomolecules close to the surface. For some interactions this might be too short. With γ -aminobutyric acid (GABA) a spacer can be placed between surface and biomolecule. It can be linked to CS_2 via its amino functionality and the carboxylic acid is free for further coupling steps (Figure 31).

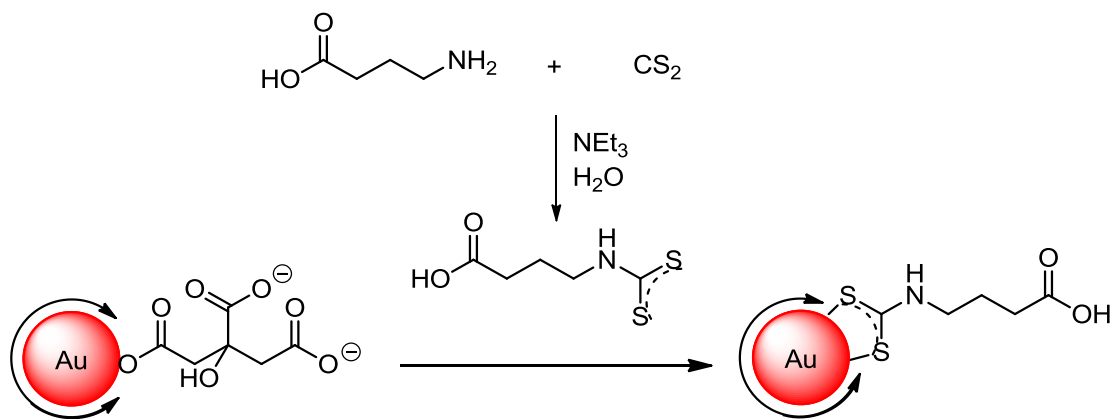


Figure 31: Reaction scheme of the formation of DTC-anchors followed by the ligand exchange at citrate-stabilized gold nanoparticles.

The intermediate product of GABA and CS_2 was formed *in situ* in aqueous solution with ultrasonic treatment. It was not characterized but added directly to gold nanoparticles functionalized with citrate, which were synthesized separately via the *Turkevich* method. The ligand can be exchanged easily using this method and the newly formed conjugates are stable in aqueous solution due to the free carboxylic acid moiety. UV/Vis spectra before and after the reaction are shown in Figure 32.

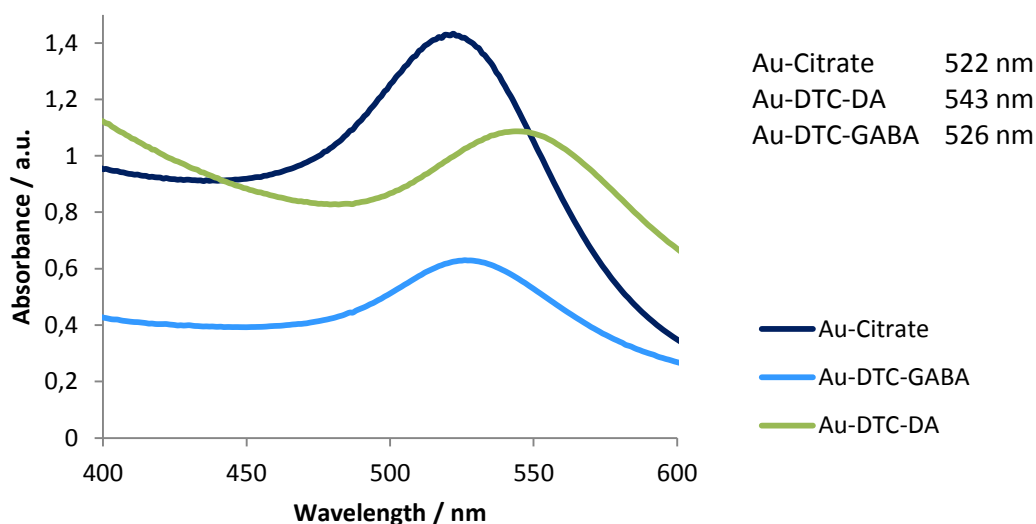


Figure 32: UV/Vis absorption spectra of gold nanoparticles after the exchange with DTC-ligands.

The maximum shifts slightly indicating the modification at the ligand shell. The nanoparticles are still dispersed and did not suffer in size. The DTC linker was also tested with dopamine as

representative for an amine reaction. The UV/Vis spectrum shows a larger shift of the maximum indicating a growth of the particles. Due to the sensitivity of dopamine towards oxidation, the reaction was done under argon atmosphere in degassed water. Nevertheless autooxidation might occur. This problem will be discussed in detail in chapter 4.8 where gold nanoparticles functionalized with biogenic amines are presented. In general multidentate ligands enhance the longtime colloidal stability of nanoparticles in comparison to monodentate ligands. [127] The bidentate lipoic acid (LA) ligand can be compared to DTC-GABA ligands due to nearly the same chain length and the free carboxylic acid giving similar water solubility properties.

4.5 Gold Nanoparticles with Positively Charged Ligands

Besides the already mentioned mercaptocarboxylic acid terminated ligand shells also gold nanoparticles with a free amine moiety were synthesized. Free amino groups can also serve as an anchor for ligands via peptide bond formation for multivalent presentation.

The first attempt for the preparation of amine functionalized gold nanoparticles was a ligand exchange reaction with *N*-acetylcysteamine (NAC-CA) at citrate-stabilized gold nanoparticles followed by deprotection, which was done directly after the coupling reaction (Figure 33). The major advantage of this synthetic strategy is the size control of the particles. This can be set in the synthesis route after *Turkevich*. Moreover, ligand exchange reactions with functionalized thiols are favored and rather efficient. In Figure 33 the reaction way is shown.

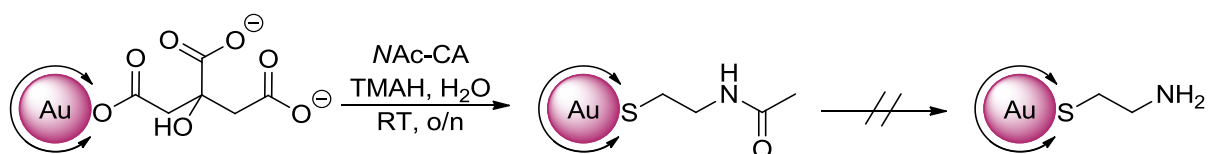


Figure 33: Reaction scheme for the ligand exchange with NAC-CA at Au-Citrate followed by deprotection of the amino moiety.

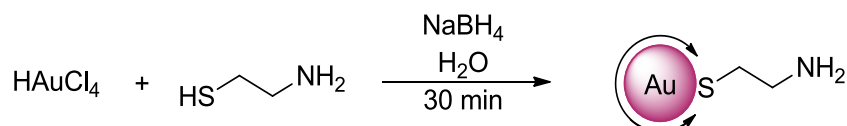
The first step of ligand exchange proceeds completely and the resulting *N*-acetylcysteamine-functionalized gold nanoparticles are stable in aqueous solution. However the deprotection of the amine group could not be realized, even if different methods were tested (Table 5).

Table 5: Reaction conditions for the deprotection of the amino moiety at gold nanoparticles.

Reagent	pH value	result
NaOH, RT	>10	No deprotection
NaOH, reflux, 24 h	>10	Slight deprotection
NaOH, reflux, 3 d	>10	Slight deprotection
4 M HCl, RT	<4	NP not stable

Reaction under basic conditions gave only slight deprotection after three days; reaction in acidic media destroyed the stability of the nanoparticles. Any other deprotection methods in organic solvents were not possible due to the aqueous media needed.

Ligand exchange reaction with cysteamine (CA), 2-aminoethanthiol, gave immediate agglomeration of the nanoparticles. Nevertheless, there are some synthetic routes to gold nanoparticles with cysteamine known in the literature. [90, 128, 129] Most of them refer to the work by *Niidome et al.* about the preparation of amine modified gold nanoparticles. [81] They report the synthesis using HAuCl_4 , CA and NaBH_4 under atmospheric conditions yielding 30 nm nanoparticles (Figure 34). A reproduction of these results under the given conditions was not possible. The resulting nanoparticles were relatively monodisperse but squared, the mean diameter was about 50 nm.

**Figure 34: Reaction scheme for the synthesis of gold nanoparticles with free amino moieties.**

In the following reaction conditions were varied to obtain smaller nanoparticles. The influence of reaction temperature and molar ratios of the reactants were tested. Heating to 40 °C gave no improvement but at 80 °C and 110 °C nearly monodisperse but still squared gold nanoparticles were formed (Figure 35). The molar ratios of gold precursor and the ligand given in the paper were 1:1.5 with only a ratio of 0.002 for the reducing agent NaBH_4 . This resulted in star-like squared nanoparticles but rather polydisperse.

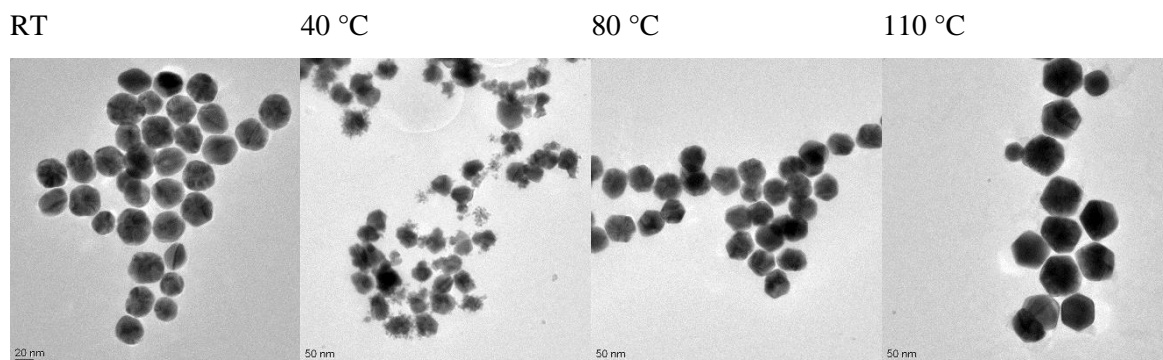


Figure 35: Variation of the reaction temperature for the synthesis of amino-stabilized gold nanoparticles.

The variation of molar ratios did not result in any monodisperse nanoparticles. The size distribution was very broad and a mixture of both small and bigger nanoparticles was achieved when the amount of the reducing agent was increased (Figure 36). The high diversity in sizes can also be observed when NaBH_4 is used as reducing agent in the *Brust-Shiffrin* method. [19] Also cysteamine does not seem to be the best ligand for the stabilization of the nanoparticles as can be concluded from these results. The system is also highly pH-dependent due to the free amino moiety.

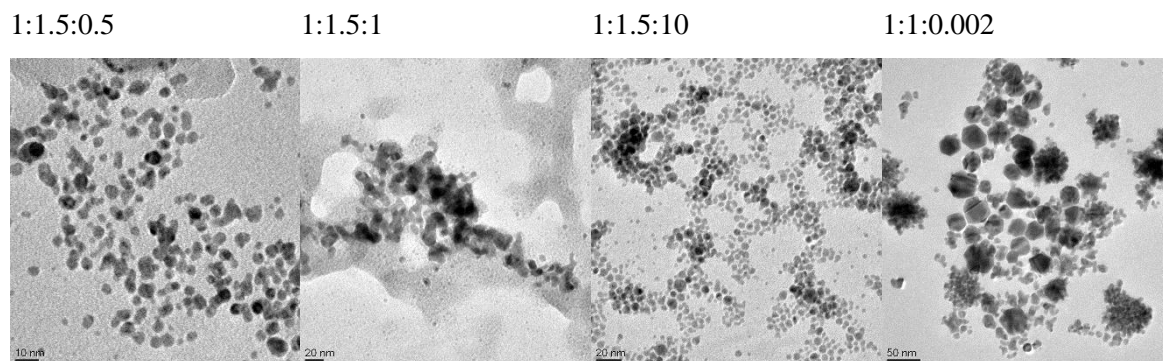


Figure 36: Variation of the molar ratios for the synthesis of amino-stabilized gold nanoparticles.

Even if nearly monodisperse gold nanoparticles could be obtained at higher reaction temperatures the synthesis itself needs to be further optimized. Further parameters have to be found to adjust the diameter of the gold nanoparticles. Nevertheless cysteamine is a promising ligand for functionalization of gold surfaces. The linker itself can be built separately and then immobilized at the surface.

4.6 Mixed Ligand Shells on Gold Nanoparticles

Interactions of nanoparticles with their environment are mainly influenced by the properties of their surface and the functional groups of the ligand shell. These properties can be tuned by the choice of the ligands. A particle shell with (two) different ligands may thus combine different properties, e. g. hydrophobic and hydrophilic properties. [130] *Portilla et al.* presented a simple synthesis approach for mixed ligand monolayers by adding different concentrations of precursor ligands to the nanoparticle solution and solubility and stability in different solvents has thus been achieved in this way. For multivalent presentation of active molecules a surface with only partial functionalization and therefore a reduced density is interesting. It could be shown that the density of active moieties is an important parameter and does have an influence on the potency of multivalent interactions. [107] This concept can be applied for gold nanoparticles with citrate ions at the surface and the ligand exchange with thiolate ligands. The idea was to modify the surface with less than 100% coverage with carboxylic acid anchors but still ensuring water solubility, to investigate whether the degree of coverage has an effect on the interactions.

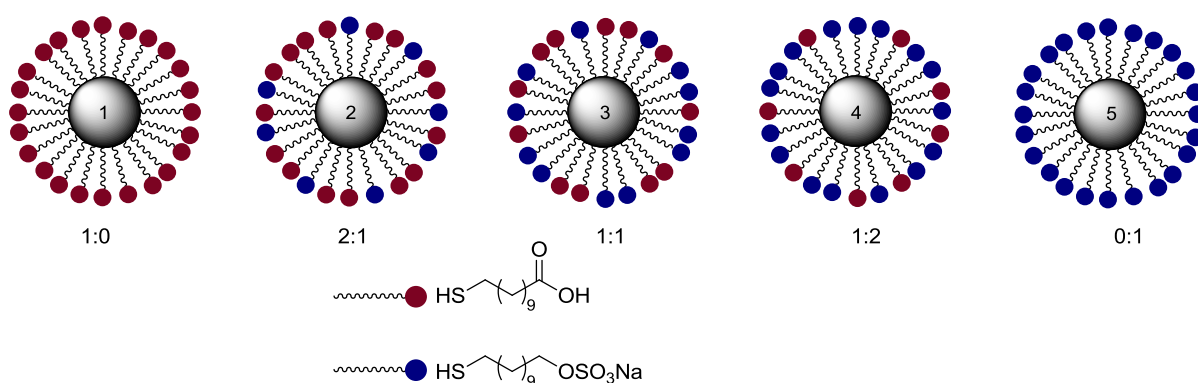


Figure 37: Surface structure of gold nanoparticles with two different ligand containing either carboxylic acid (MUDA) or sulfated alcohol (MUDOLS) termination.

Both MUDA and MUDOLS functionalized gold nanoparticles exhibit excellent stability in aqueous solution. For coupling with biomolecules only free carboxylic acid moieties are relevant and the active surface can be thinned out. Ligand exchange reaction was performed with two different ligands. Stoichiometric mixtures of both MUDA and MUDOLS were added to citrate-stabilized gold nanoparticles and stirred at room temperature. Five different gold nanoparticles were obtained (Figure 37). The solutions were dialyzed against water and characterized with UV/Vis, DLS and *zeta*-potential analysis. As the diameter of the

nanoparticles did not change no characteristic shifts are observable in the UV/Vis spectra (Figure 38).

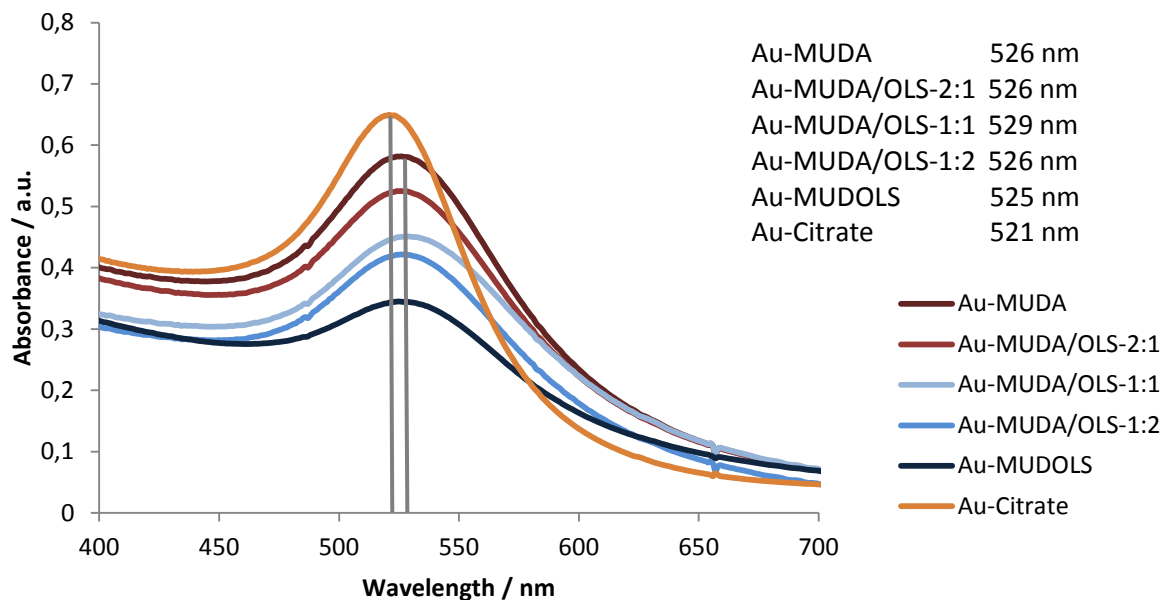


Figure 38: UV/Vis absorption spectra of gold nanoparticles with a mixed ligand shell of both MUDA and MUDOLS are shown. All colloidal solutions are stable.

The composition of the ligand shell was characterized via *zeta*-potential analysis because the surface modifications can be monitored via the change of this value. The *zeta*-potential describes the electrostatic potential near the surface of particles in solution. It depends on the ligands terminating the shell. Compared to citrate-stabilized gold nanoparticles the values for the potential of MUDA and MUDOLS are higher. For both Au-MUDA and Au-MUDOLS it differs significantly. The potentials of the mixed ligand shell nanoparticles correlate linearly (Table 6). With increasing content of negatively charged MUDOLS the value rises. DLS measurements show slightly different diameters of the nanoparticles in solution.

Table 6: Zeta-Potential measurements of gold nanoparticles with different mixed ligand shells.

Type	Shell	d_{hydr} / nm	ζ potential / mV	Conductivity / $\mu\text{S}/\text{cm}$
Au-Citrate	-	17 ± 3	-28 ± 6	1.11
1 Au-MUDA	1:0	24 ± 7	-57 ± 17	8.91
2 Au-MUDA/OLS	2:1	34 ± 4	-58 ± 23	0.67
3 Au-MUDA/OLS	1:1	38 ± 4	-63 ± 12	0.58
4 Au-MUDA/OLS	1:2	32 ± 4	-68 ± 12	0.55
5 Au-MUDOLS	0:1	19 ± 3	-70 ± 13	0.23

Functionalization through coupling of biomolecules to the nanoparticles could be used to evaluate the effect of coverage. The concept could also be transferred to other ligands building a buffer system which might lead to expanded stability in aqueous solution under different pH values.

4.7 Functionalization at the Ligand Periphery

After the synthesis of the gold nanoparticles functionalization of the free carboxylic acid moieties was performed. Peptide coupling using an amine or a biomolecule with an amino moiety can be conducted. There are two strategies of functionalization: full functionalized ligand synthesis prior to reaction with gold nanoparticles using ligand exchange or step by step reactions at the periphery. Both pathways have advantages and each ligand system has to be evaluated independently. Complex molecules are better to be synthesized separately, not only due to required comprehensive characterization of the organic structure. Coupling at the periphery in solution includes simple work up via dialysis but needs full stabilization of the nanoparticles during synthesis. *N*-Hydroxysuccinimide (NHS) or the sulfonated analogues and 1-ethyl-3-(3-dimethylaminopropyl)carbodiimide (EDC) are used to prepare amine-reactive esters in solid-phase immobilization applications. Both are soluble in aqueous and organic solvents and in the presence of carbodiimides they form a semi-stable NHS-ester with carboxylates. It hydrolyzes within hours depending on the pH of the reaction solution but it is sufficiently stable for a coupling process in solution. [131, 132] Reaction of the *o*-acylisourea with amines is also possible but with less yield.

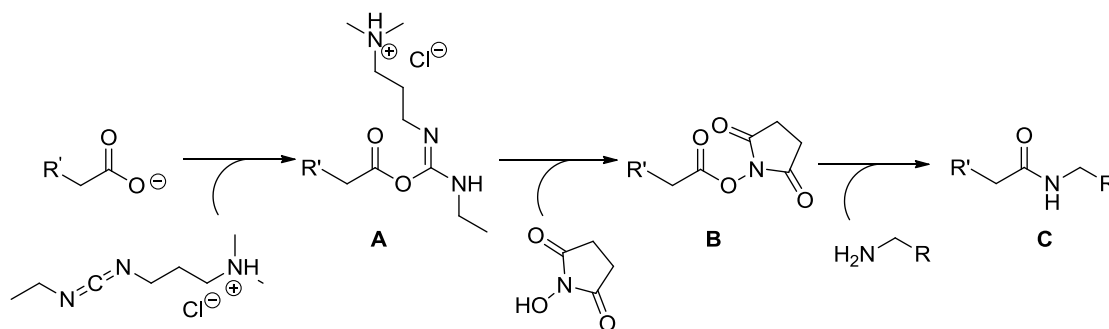


Figure 39: Reaction pathway of the formation of the stable amide bond between carboxylate and amine mediated by EDC and NHS. **A:** unstable reactive o-acylisourea ester, **B:** semi-stable amine-reactive NHS ester, **C:** stable amide bond.

Au-MUDA nanoparticles were mixed together with NHS and EDC under the addition of NaOH and the active ester was formed (Figure 39). Purification and isolation of the product was not possible. Au-MUDA-NHS is not stable enough in aqueous solution. To obtain active-ester coordinated nanoparticles the linker has to be synthesized and then coupled onto the surface of nanoparticles dispersed in organic solvents like DMF. These particles can be coupled with an amine and then transferred into aqueous solution. [133] Dodecanethiol-stabilized gold nanoparticles can serve as precursor material.

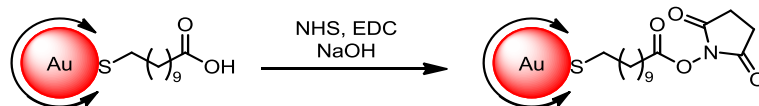


Figure 40: Formation of Au-MUDA-NHS active ester in solution. The product is not stable and hydrolyzed within hours.

As the active ester is stable for only hours coupling with the respective amine has to be done *in situ*. An equivalent of amine can be added to the reaction solution and the amide bond forms immediately (Figure 40 & Figure 41). To ensure full reaction another equivalent of NHS, EDC and amine is added after two hours. After that the solution is purified via dialysis against water. For the stability of the resulting nanoparticles a basic pH is needed, so TMAH or NaOH are added.

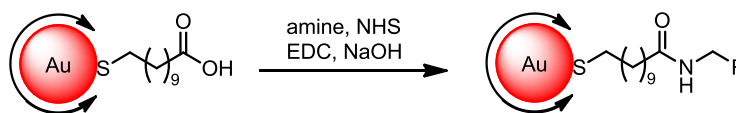


Figure 41: Coupling of amines to MUDA-functionalized gold nanoparticles by a NHS/EDC mediated reaction. The resulting nanoparticles are stable in aqueous solution.

4.8 Functionalization with Bioactive Amines

Gold nanoparticles with a free carboxylate group were functionalized with four different neurotransmitters, bioactive amines responsible for communication between cells (Figure 42). [134] Histamine, dopamine and serotonin are biogenic amines derived from amino acids by decarboxylation. Carbachol is structurally similar to acetylcholine and a stable derivate. It binds to acetylcholinic receptors and acts as a cholinergic agonist. Because of its amino moiety it can be coupled to the gold nanoparticles in the same way as the biogenic amines. All four types are frequently found in organisms. By binding onto the surface the free amino group gets coupled and can no longer participate in receptor recognition. Only a simplified binding moiety is available for the interaction, but several studies proved this to be sufficient for specific interactions. [110]

Immobilization of neurotransmitters on gold nanoparticles is little explored and the biological functionality of the conjugates even less. The amines were coupled onto 14 nm gold nanoparticles with a carboxylic acid terminated shell via the EDC/NHS method (Figure 39).

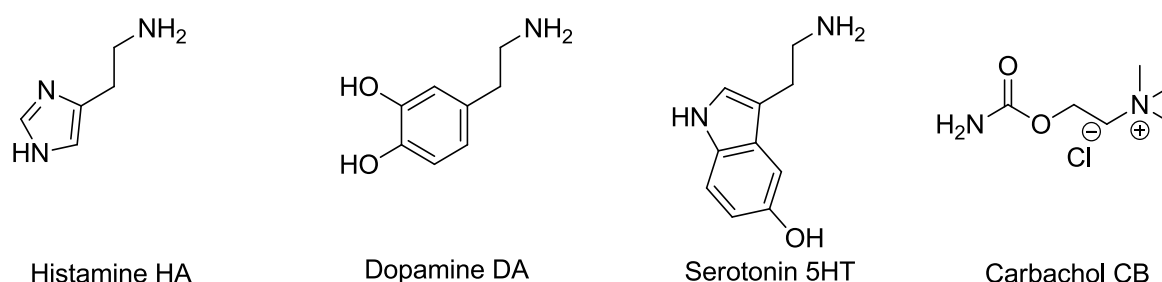


Figure 42: Bioactive amines histamine, dopamine, serotonin (5-hydroxytryptamine) and carbachol.

Immobilization of the amines was accomplished in aqueous solution. MUDA-functionalized gold nanoparticles were mixed with EDC/NHS and NaOH forming the active ester.

Subsequently the bioactive amine was added. All chemicals were added in large amount to ensure complete coupling of the free carboxylic acid.

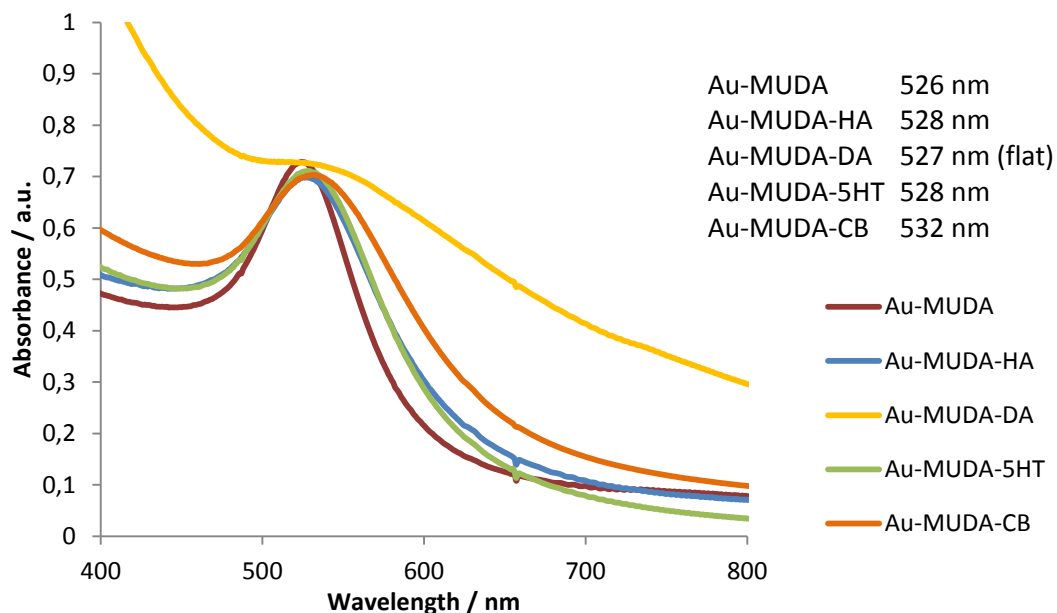


Figure 43: UV/Vis spectra of gold nanoparticles (14 nm) functionalized with histamine (HA), dopamine (DA), serotonin (5HT) and carbachol (CB). Au-MUDA is plotted for comparison with the precursor solution.

Coupling with the molecules histamine and serotonin gave stable nanoparticles; the plasmon resonance maxima are clearly visible in the UV/Vis spectra. Compared to Au-MUDA the maxima shift only slightly to longer wavelengths. Only the maximum of dopamine functionalized gold nanoparticles lost its shape indicating a change of particle dispersity (Figure 43). Also Au-MUDA-CB were stable despite a broadened maximum. This can be explained because of the positively charged ligand shell responsible for electrostatic interactions between the nanoparticles. The colloidal solution is prone to aggregation and the pH value has to be adjusted at values between 8 and 10. Additionally, gold nanoparticles of 7 nm and 25 nm size were functionalized with histamine and dopamine. Histamine functionalized gold nanoparticles were fully characterized in the publication chapter 4.10.

Histamine functionalized gold nanoparticles

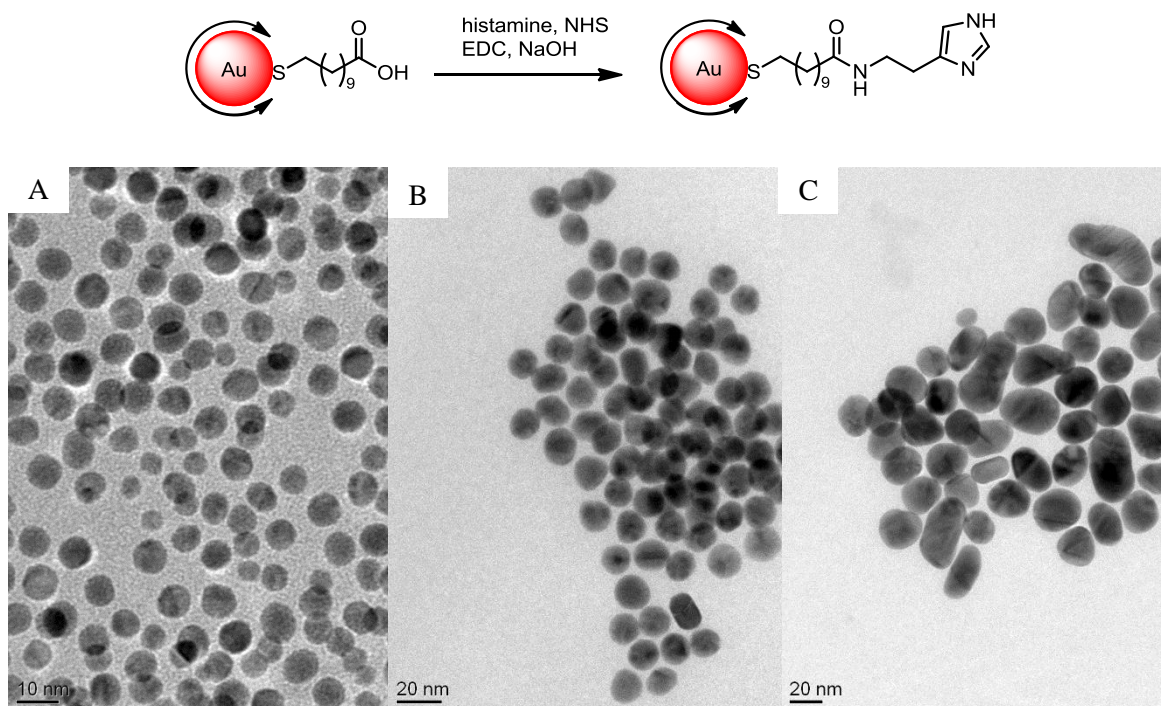


Figure 44: Histamine functionalized gold nanoparticles with three different core sizes: reaction scheme and TEM images. A $d_{\text{TEM}} = 7.3 \pm 0.9$ nm, $d_{\text{hydr}} = 11 \pm 2$ nm; B $d_{\text{TEM}} = 14.7 \pm 1.2$ nm, $d_{\text{hydr}} = 26 \pm 6$ nm; C $d_{\text{TEM}} = 25.7 \pm 1.2$ nm, $d_{\text{hydr}} = 32 \pm 8$ nm.

Histamine functionalized gold nanoparticles were synthesized with three different core sizes (Figure 44). All three core sizes are suitable for biological applications. In the tests of biological functionality the effect of the mean diameter shall be investigated. The relative number of active epitopes depends on the surface provided for immobilization and should effect the potency of the nanoparticles. The histamine functionalized gold nanoparticles are stable at a neutral pH value in contrast to the other gold nanoparticles which need basic conditions. This might be explained by to the buffering capacity of the imidazole moiety.

Dopamine functionalized gold nanoparticles

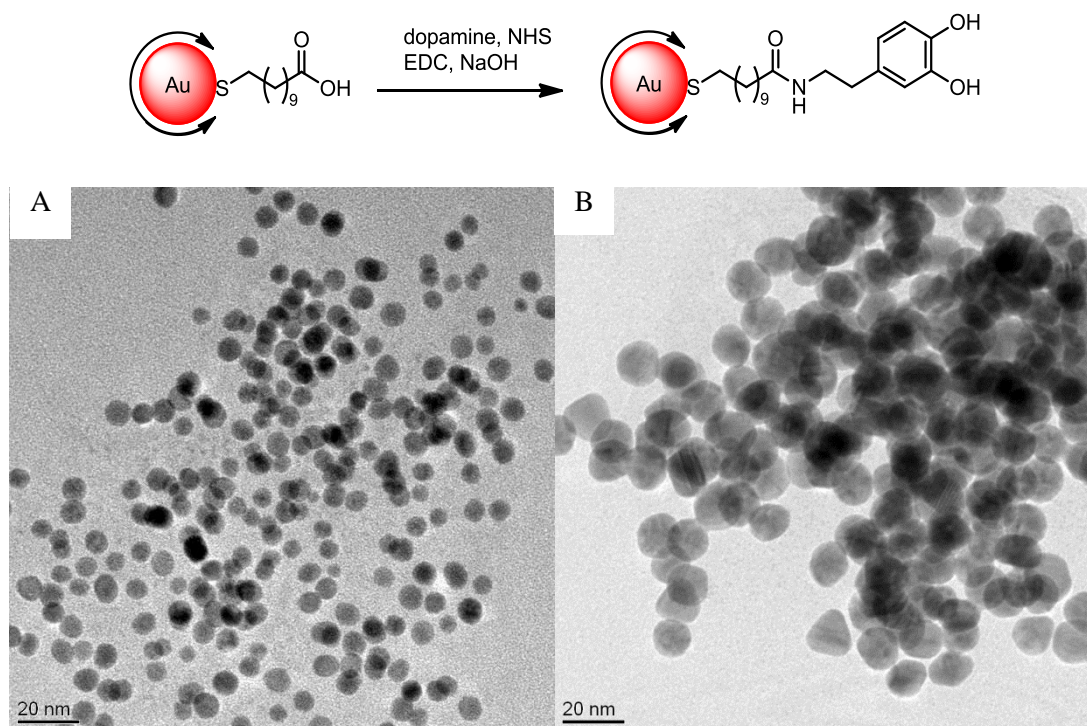


Figure 45: Dopamine functionalized gold nanoparticles with two different core sizes: reaction scheme and TEM images. A $d_{\text{TEM}} = 7.8 \pm 1.2$ nm, $d_{\text{hydr}} = 9 \pm 2$ nm; B $d_{\text{TEM}} = 15 \pm 1$ nm, $d_{\text{hydr}} = 26 \pm 6$ nm.

Only for dopamine functionalization transformation of the nanoparticles was observed. After some hours the nanoparticles agglomerate and the solution turned brown, but is still clear. Figure 45 shows a TEM image after the functionalization. NMR analysis confirms immobilized dopamine molecules at the gold nanoparticles (see Experimental Section). The brown color arises from the formation of polydopamine (Figure 46). The catechol moiety of dopamine is oxidized to a quinone under aerobic conditions and intramolecular cyclization takes place. Another oxidative step and isomerization leads to a 5,6-dihydroxyindole, which can then be oxidized to the analogue quinone.

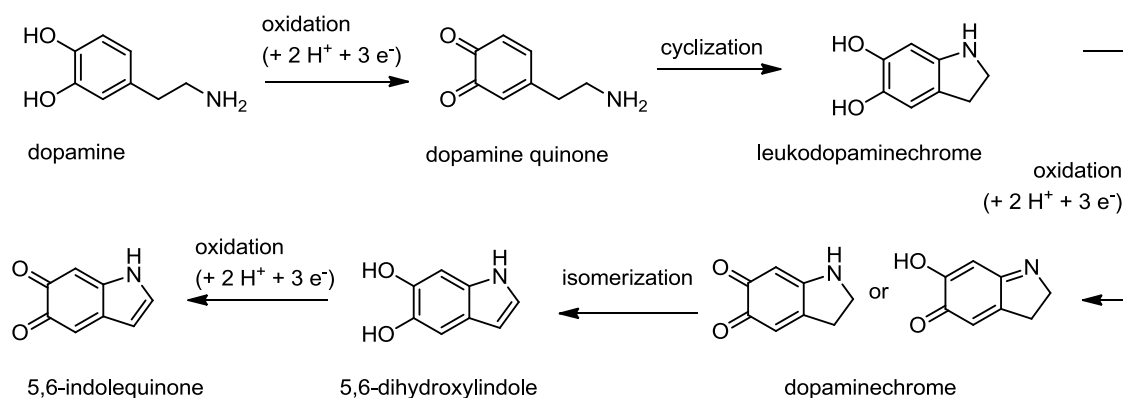


Figure 46: Mechanism of the formation of polydopamine under aerobic conditions. [135]

The surface of the nanoparticles is coated with the polymer but they are still water-soluble. This is formed when dopamine is exposed to an aerobic environment in solution. Oxidation to quinone and intramolecular cyclization leads to 5,6-indolequinone which appears brownish. It forms a non-covalent polymer with supramolecular aggregation. [135] NMR analysis of the ligand shell did not indicate a polymeric layer but only signals from immobilized dopamine. No further investigations on this phenomenon were performed. The synthesized gold nanoparticles with dopamine at the surface were tested for their biological functionality.

There are some applications for dopamine-coated inorganic and organic materials. [136] Noble metal nanoparticles can be used as optical sensing agents for the detection of dopamine. [137] Dopamine can also serve as a reducing agent. [138] Besides the amino group dopamine also contains a catechol moiety. This functional group can also interact with surfaces; the reversed anchor has a free amino moiety where biomolecule can be attached. Iron oxide nanoparticles can be synthesized or functionalized via this method. [139–141] Gold nanoparticles were used as synthesized for the biological applications.

Serotonin functionalized gold nanoparticles

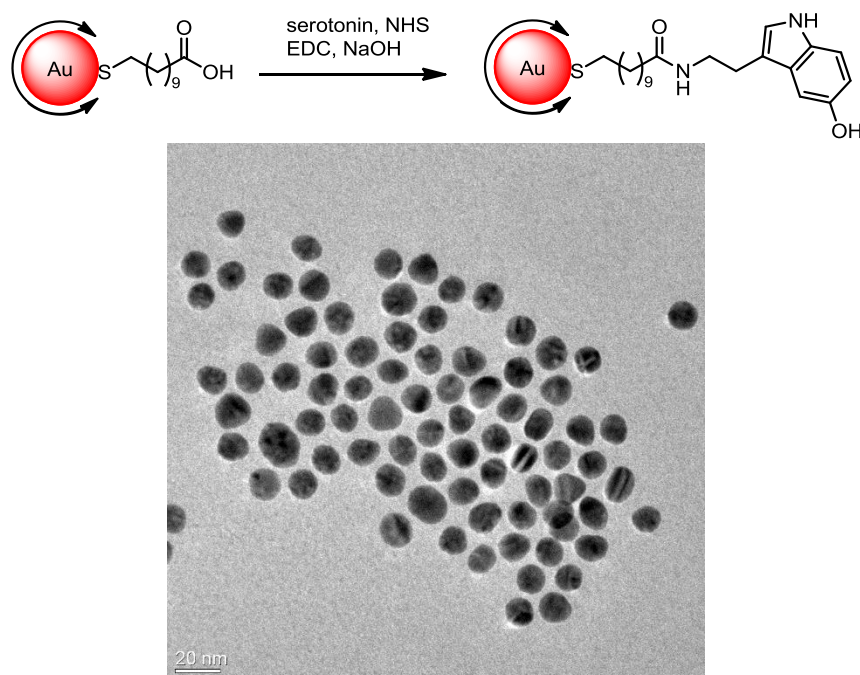


Figure 47: Serotonin functionalized gold nanoparticles: reaction scheme and TEM image. Diameter $d_{\text{TEM}} = 14.1 \pm 0.9$ nm, $d_{\text{hydr}} = 16 \pm 4$ nm.

Gold nanoparticles with serotonin were also synthesized. Figure 47 shows a TEM image of the nanoparticles after functionalization. The hydroxylated indolamine backbone is also prone for oxidation and all reaction steps were performed in degassed water and under argon atmosphere. No change in color of the solution was observable. The plasmon resonance maximum clearly appears at 528 nm (Figure 43). With NMR analysis immobilization of serotonin at the gold nanoparticles surface can be confirmed.

Carbachol functionalized gold nanoparticles

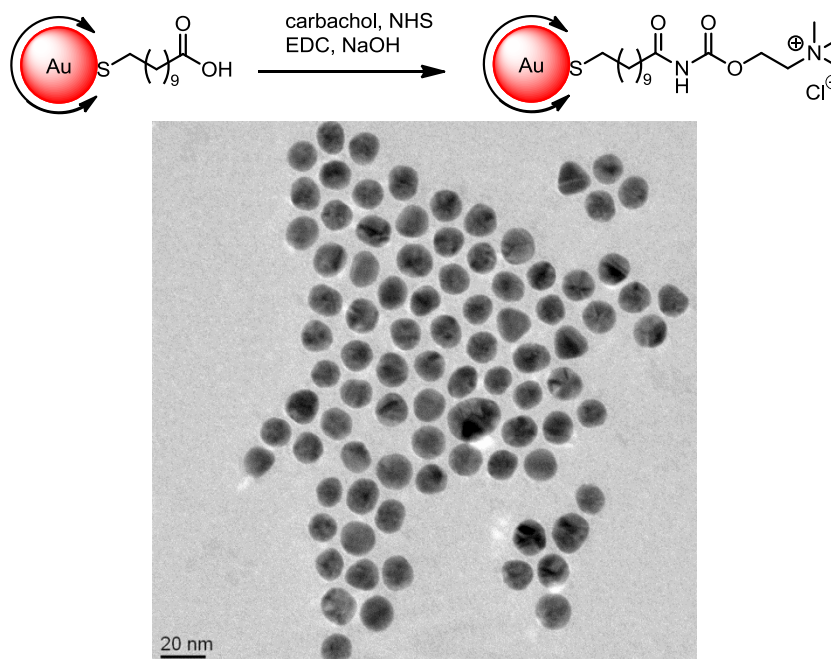


Figure 48: Carbachol functionalized gold nanoparticles: reaction scheme and TEM image. Diameter $d_{\text{TEM}} = 14.5 \pm 0.7$ nm, $d_{\text{hydr}} = 17 \pm 6$ nm.

Gold nanoparticles were also functionalized with the small molecule carbachol. It is a derivative of acetylcholine and can be applied as a drug for the activation of acetylcholine receptors. The molecule possesses a positive charge at the quaternary amine. Immobilization is difficult due to repulsion between the nanoparticles. Figure 48 shows a TEM image of the gold nanoparticles after the functionalization indicating no difference in particle size and dispersity. So the immobilization on gold nanoparticles was indeed successful. NMR analysis confirms immobilized carbachol at the gold nanoparticles (see Experimental Section). Due to interaction with the material of the dialysis tube purification must be done carefully. Time for dialysis should not be longer than 1 hour after which the sample has to be transferred into a new tube. The functionalized gold nanoparticles should be stored in an Eppendorf cup. This phenomenon could also be observed with the amine-modified nanoparticles also inheriting a positive charge. Interactions with both the dialysis material and glass vessel could be observed.

Functionalization of amine-modified gold nanoparticles

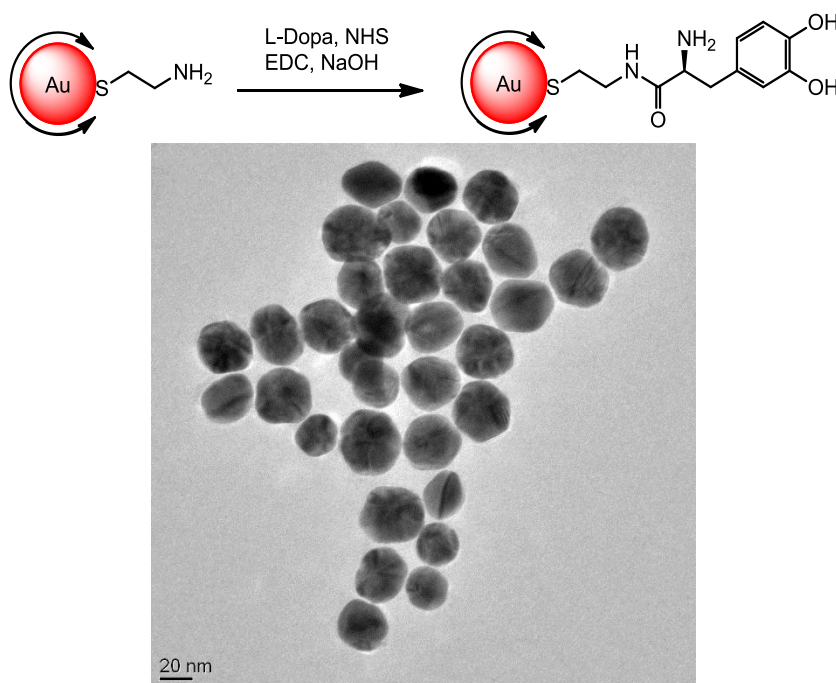


Figure 49: L-Dopa functionalized gold nanoparticles: reaction scheme and TEM image. Diameter

$$d_{\text{TEM}} = 30.7 \pm 7.2 \text{ nm}, d_{\text{hydr}} = 45 \pm 9 \text{ nm}.$$

Coupling partners for gold nanoparticles with free carboxylate moieties need to possess either an amino group for peptide coupling or an alcohol group for esterification. Vice versa, bioactive molecules with a free carboxylic acid moiety can be coupled on gold nanoparticles, but requirement for the nanoparticles is a free amino moiety. As mentioned previously nanoparticles with a positively charged ligand shell are relatively instable and particle growth is difficult to control. Yet the synthesis of 30 nm gold nanoparticles with cysteamine at the surface was successful. Structurally amino acids are very similar to the biogenic amines, because they possess both a carboxylic group and an amino group. Subsequent reaction of amino acids results in peptides which are coupled via peptide (amide) bonds. The immobilization of such small peptides on gold nanoparticles is also an interesting field of research. [142] Here L-Dopa was coupled successfully to the amine-free gold nanoparticles successfully. Figure 49 shows a TEM image after functionalization and NMR analysis confirmed the immobilization (See Experimental Section). Once again a brown coloring of the solution was observed resulting from the autooxidation of the catechol moiety.

4.9 Biological Functionality

The biological functionality of the four synthesized gold nanoparticles was tested. Like many other bioactive substances the neurotransmitters exert their effects by binding to receptors located at the cell surface. The native ligands, molecular histamine, dopamine, serotonin and carbachol, address their particular receptors and subunits. The newly developed conjugates of ligand and gold nanoparticle were tested for the same effects and compared to the native analogues where applicable. Investigations on the ability to induce chloride secretion at receptors on a tissue were done in the research group of Prof. Marin Diener, Institute for Veterinary Physiology at the Justus-Liebig-University Giessen. Gold nanoparticles were administered to rat mucosa mounted in an *Ussing* Chamber. When receptors are stimulated an increase in chloride secretions takes place and a rise in the short circuit (I_{sc}) is observed. Histamine functionalized gold nanoparticles were tested with three different core sizes. All types were able to stimulate the receptors but for the bigger 25 nm nanoparticles the signals were unstable and too low for evaluation. Both 7 nm and 14 nm gold nanoparticles clearly induce a chloride secretion. After the addition of the gold nanoparticles the tissue is treated with the secretagogue forskolin. The cAMP-dependent stimulator is a messenger for proper biological functionality. As it induced a prompt rise in I_{sc} the tissue is not harmed by the nanoparticles. The results from 14 nm gold nanoparticles with histamine were published in *Org. Biomol. Chem.* (see chapter 4.10). The dose-effect curve of 7 nm gold nanoparticles is shown in Figure 50.

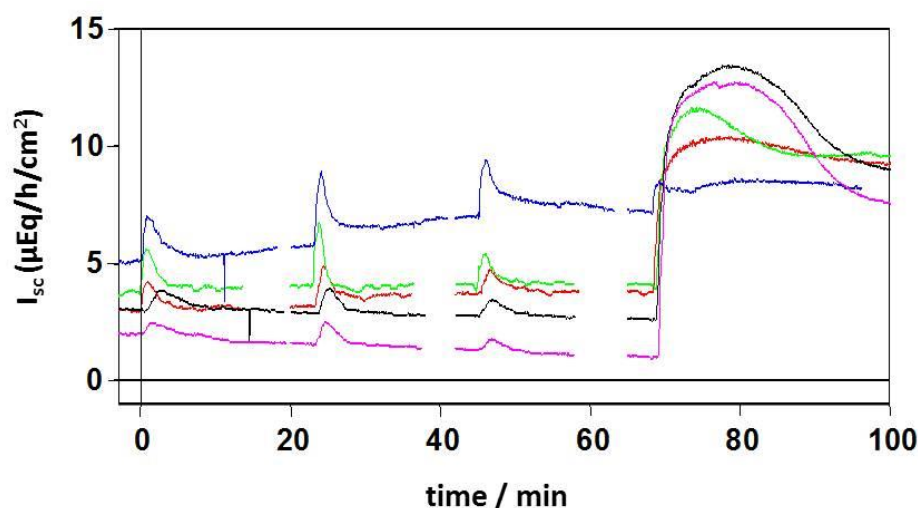


Figure 50: Au-MUDA-HA 7 nm at the serosal side induced a time-dependent increase in the I_{sc} , forskolin was added for the control of proper biological functionality; each peak is an addition of gold nanoparticle samples.

Five different samples were tested.

To verify the signals only coming from histamine-receptor interactions the gold nanoparticles with a free carboxylate moiety were tested. Unfortunately Au-MUDA also evokes an increase in I_{sc} (Figure 51). Gold nanoparticles without derivatized neurotransmitter are able to stimulate receptors. Still, activation concentrations are lower when multivalently presented. Gold nanoparticles with a sulfated epitope were used to verify the signals. Indeed they are only evoked by multivalently presented histamine.

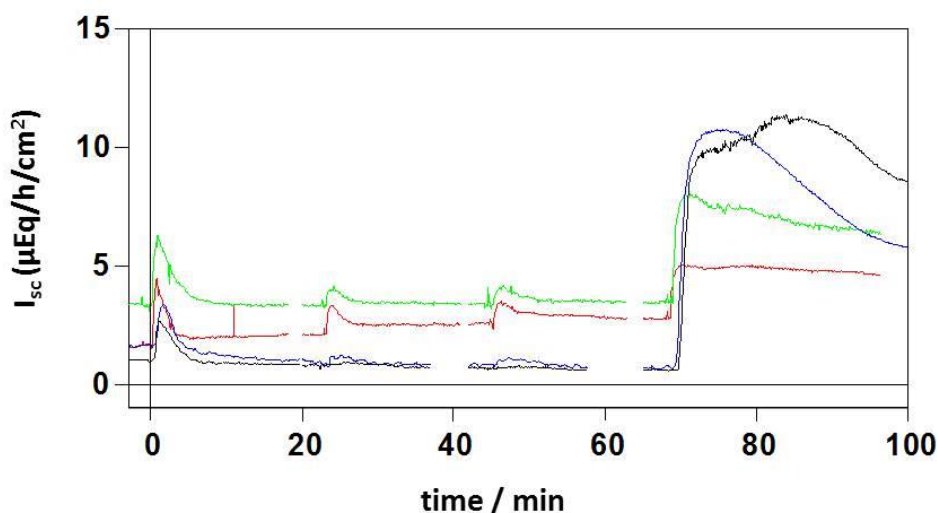


Figure 51: Au-MUDA at the serosal side induced a time-dependent increase in I_{sc} , forskolin was added for the control of proper biological functionality; each peak is an addition of gold nanoparticles. Four different samples were tested.

Gold nanoparticles with dopamine were tested for two different sizes (Figure 52). Again the colloidal solution was added at the serosal side and the increase in I_{sc} was measured. Both 7 nm and 14 nm gold nanoparticles were not able to induce chloride secretion at the administered concentrations. As seen in the results for histamine-coated gold nanoparticles the concentration of effective active moieties is sufficient for the receptor activation. The addition of forskolin confirmed the viability of the tissue.

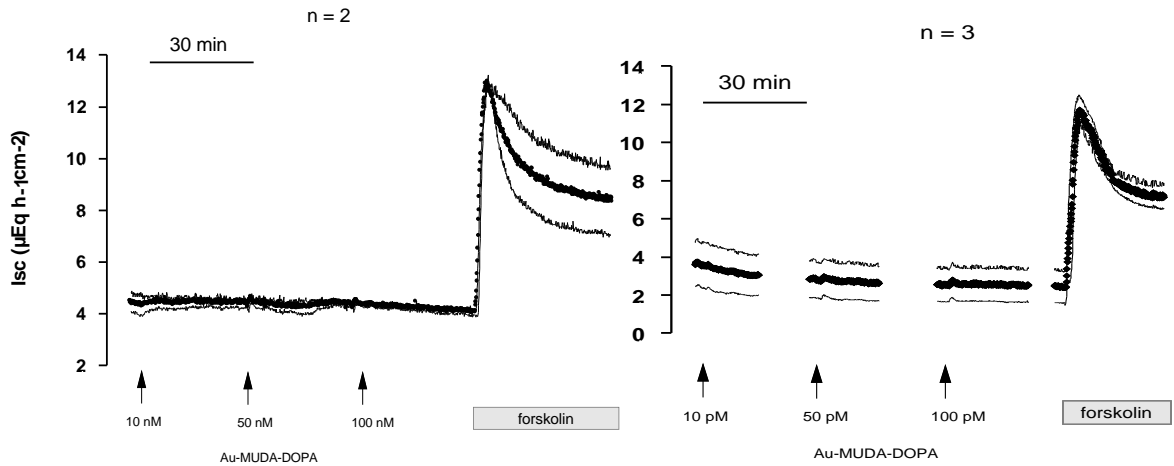


Figure 52: Au-MUDA-DA 7 nm (left) and 14 nm (right) at the serosal side induced a time dependent increase in I_{sc} , forskolin was added for the control of biological functionality.

One possible explanation for the absent signals might be the autooxidation of the catechol moiety. Both colloidal solutions turned brown after exposure to air which indicates the formation of the quinone. Nevertheless there was no cyclization visible in the NMR spectra, up to now no further experiments were done to prove this assumption.

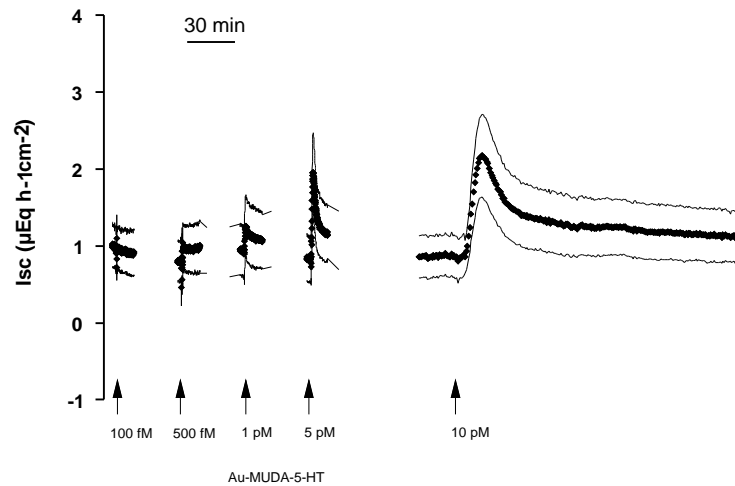


Figure 53: Au-MUDA-5HT at the serosal side induced a time-dependent increase in I_{sc} , forskolin was added for the control of proper biological functionality; each peak is an addition of gold nanoparticles. Four different samples were tested; $n = 7$.

Serotonin-coated 14 nm gold nanoparticles were also tested for the activation of receptors (Figure 53). They induce a concentration-dependent increase in the I_{sc} as did the histamine-coated. The signals correspond more likely to chloride secretion. Since native serotonin

activates different receptor types no definite classification can be made from results. Compared to native serotonin the concentrations for activation are much lower at nanomolar concentrations. Again multivalent presentation of the active moiety enhances the interactions. Serotonin receptors belong to the group of G protein-coupled receptors and ligand-gated ion channels and found in a variety of organisms. Serotonin plays diverse roles in normal physiology, including for example developmental, cardiovascular, gastrointestinal, and endocrinal functions. [143] Studies on multivalent effects on the activation of the 5-HT₃-receptor showed enhanced activity for bivalent ligands. [144] Dendrimeric ligands also showed enhanced affinity at the 5-HT₃ receptor. [145] These are examples for multivalency enhancing activities of natural processes.

Last but not least carbachol-capped 14 nm gold nanoparticles were tested. The stable actelycholine derivative showed excellent affinity to the receptors. The results were compared directly to native carbachol (Figure 54). Both Au-MUDA-CB and native CB induce a concentration-dependent increase in I_{sc} corresponding to chloride secretion.

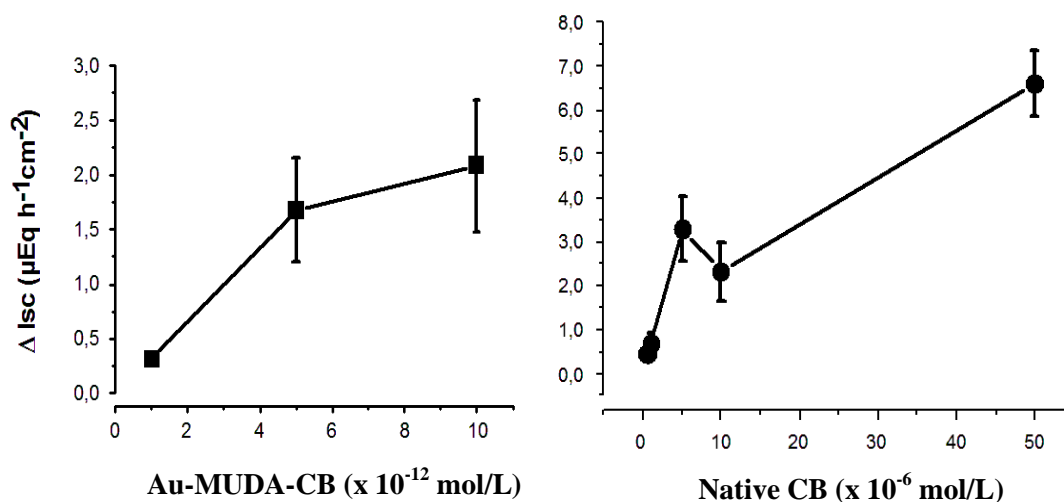


Figure 54: Au-MUDA CB induced an increase in the I_{sc} , native carbachol induced an increase in the I_{sc} at different concentrations; $n = 6$.

The observed activation concentrations are in picomolar, nearly half as much as for the native analogue. A nearly equivalent response is evoked by 1 pM potency between Au-MUDA-CB in comparison to 500 nM native CB indicating a strong increase in potency (Figure 55). The effect of these gold nanoparticles is again supported by the multivalent presentation. The high local density and the special arrangement allow simultaneous binding which enhances the effects.

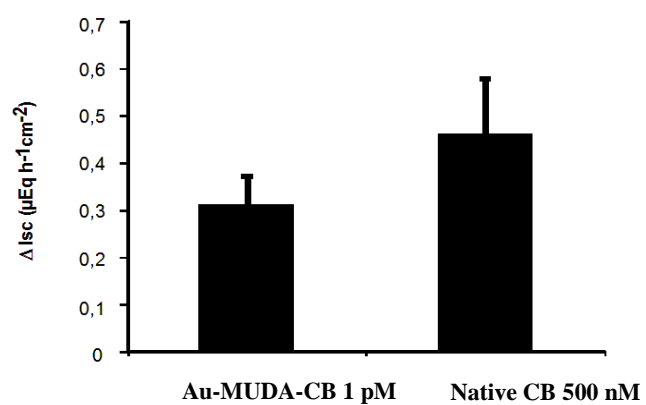


Figure 55: Potency of Au-MUDA-CB versus native carbachol; an equivalent potency between Au-MUDA-CB and carbachol was obtained at 1 pM Au-MUDA-CA and 500 nM CB.

4.10 Effects of Multivalent Histamine Supported on Gold Nanoparticles: Activation of Histamine Receptors by Derivatized Histamine at Subnanomolar Concentrations

This work was published in Organic and Biomolecular Chemistry, 2015, 13, 9984-9992

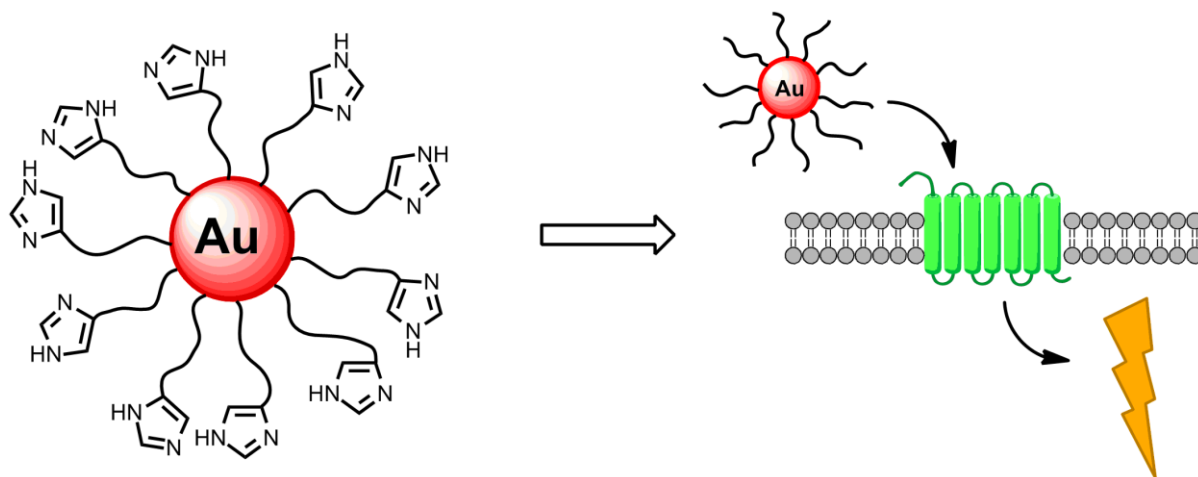
Received 3rd July 2015, Accepted 5th August 2015

First published on the web 20th August 2015

Friederike Gasiorek ^a, Ervice Pouokam ^b, Martin Diener ^{*b}, Sabine Schlecht ^a and Mathias S. Wickleder ^{*a}

^aInstitute of Inorganic and Analytical Chemistry, Justus-Liebig-University, Heinrich-Buff-Ring 58, 35392 Giessen, Germany. E-mail: friederike.gasiorek@anorg.chemie.uni-giessen.de

^bInstitute for Veterinary Physiology and Biochemistry, Justus-Liebig-University, Frankfurter Straße 100, 35392 Giessen, Germany. E-mail: martin.diener@vetmed.uni-giessen.de



Abstract

Colloidal gold nanoparticles with a functionalized ligand shell were synthesized and used as new histamine receptor agonists. Mercaptoundecanoic acid moieties were attached to the surface of the nanoparticles and derivatized with native histamine. The multivalent presentation of the immobilized ligands carried by the gold nanoparticles resulted in extremely low activation concentrations for histamine receptors on rat colonic epithelium. As a functional read-out system, chloride secretion resulting from stimulation of neuronal and epithelial histamine H₁ and H₂ receptors was measured in *Ussing* chamber experiments. These responses were strictly attributed to the histamine entities as histamine-free particles Au-MUDOLS or the monovalent ligand AcS-MUDA-HA proved to be ineffective. The vitality of the tissues used was not impaired by the nanoparticles.

Introduction

During the past 20 years, the number of applications of nano- and microdevices in the fields of biotechnology and biomedicine has been increased drastically. [3, 146] Most promising tools are nanoparticles. [147] They represent nanoscale materials with unique chemical and physical properties due to their size. These are for example optical absorption (metal nanoparticles), photoluminescence (semiconductor quantum dots) or magnetic behavior (iron oxides). Their applicability derives not only from the fact that their dimension range is in the size of some biomolecules like proteins or receptors, but also that through simple surface modification a huge variety of interactions can be achieved. The basic requirement for every application is the proper surface functionalization of the particles, which determines their interaction with the environment. In this study we chose gold nanoparticles as a template because of their well-known synthesis and functionalization with small molecules. [14, 112] Moreover they are biocompatible. We took these particles and applied the concept of multivalency for the interaction with biological tissue. Multivalent presentation of immobilized ligands is a common concept in ligand–receptor interactions and can result in high affinities of ligands that possess only moderate binding constants in a similar concentration range when they are presented in their monovalent form. [105, 106, 148] Simplifying binding structures reduces the synthetic complexity of the molecules immobilized on the nanoparticles and has the advantage of being synthetically well accessible. Multivalent carriers can either inhibit or activate biological processes in a different way than the monovalent analogue. Usually the effective concentration is much lower. [110] There are only few examples where this concept is applied on receptor–ligand interactions with neurotransmitters. *Paolino et al.* synthesized dendrimeric tetravalent ligands for the activation of ligand-gated ion channels. [145] Indeed they found activation

concentrations in the low picomolar range. *Saada et al.* synthesized gold nanoparticles coated with histamine and applied the conjugates for enzyme activation. [111] They also found an enhancement of the activation properties for these conjugates. Mediators such as histamine are key regulators of physiological processes such as ion transport across epithelial barriers. Chloride secretion is one of these processes occurring for example at the colonic epithelium. [149, 150] Such a secretion can be activated via stimulation of histamine H₁ and/or H₂ receptors as previously shown. [151–153] The receptor activity can also be blocked by inhibitors, which are well-known for the histaminic receptors. Mediators or neurotransmitters represent an interesting class of bioactive molecules and yet there is no study on multivalent ligand presentation on biological systems. In this paper we report the immobilization and multivalence of the biogenic amine histamine on gold nanoparticles as well as its biological function in receptor activation.

Results and Discussion

Synthesis of the gold nanoparticles

By attaching histamine derivatives on gold nanoparticles we developed a new conjugate for the interaction with compatible receptors. Water soluble gold nanoparticles with a terminally functionalized thiol shell were prepared and used as a scaffold for the multivalent presentation of histamine. Gold nanoparticles with an average diameter of 14 nm were synthesized by a modification of a well-known method developed by *Turkevich et al.* (Figure 56). [16, 116] In an aqueous solution Au(III) was reduced by sodium citrate which serves not only as reducing agent but also as a ligand to prevent aggregation of the formed particles. Even if the solvent is limited to water or polar equivalents like DMSO, the resulting size of the particles can be defined by the molar ratios of the starting materials, the reaction temperature and time. By this method, gold nanoparticles with a diameter of 14 nm (NP 1, Figure 56) could be obtained. Depending on the size of the particles, the surface is coated with several thousand ligands with respect to the steric demand of a single ligand. The resulting nanoparticles are stabilized by electrostatic repulsion of the negatively charged citrate ions adsorbed on their surface. This layer can be easily replaced by ligands with a stronger binding affinity, such as for example thiols. [70, 118] Thus, in a second step the ligand shell was substituted by a bivalent ligand. Bivalent ligands give access to further functionalization steps at the ligand periphery. One end binds to the surface and gives stability to the particle whereas the other end is exposed to the solution. Depending on the free moiety, the particles possess different stabilities at different pH values.

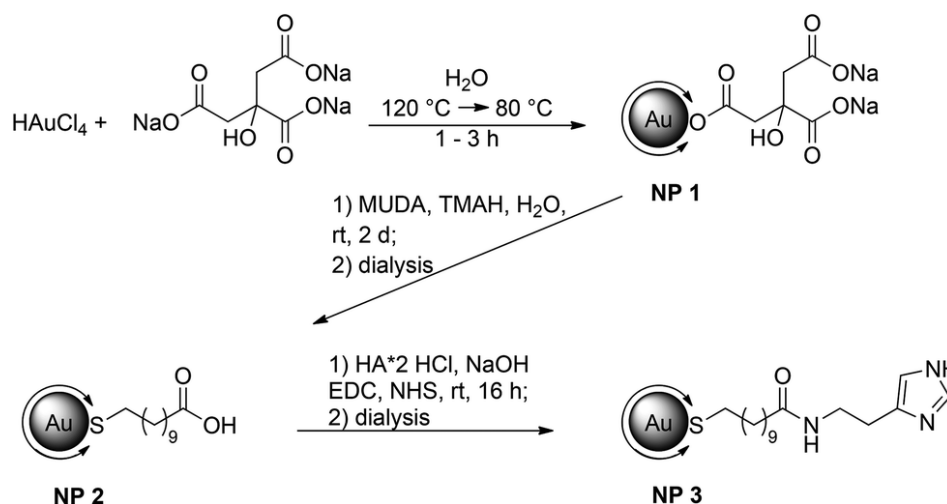


Figure 56: Synthetic procedure for gold nanoparticles with a mean diameter of 14 nm (NP 1) followed by ligand exchange with 11-mercaptoundecanoic acid (NP 2) and functionalization with histamine (NP 3, Au-MUDA-HA). Double arrows at the Au core represent the ligand.

There is a wide variety of ligands suitable for exchange still providing stability in aqueous media. Often poly(ethylene glycol) (PEG) is used as a ligand as it provides enough colloidal stability and reduces nonspecific adsorption. Besides “PEGylation”, ω -functionalized thiol surfactants with free carboxylic acid groups are a versatile type of ligand and are often used in aqueous solution. They offer an additional anchor point for further attachments of biological molecules. Herein we chose 11-mercaptoundecanoic acid (MUDA). On the one hand, a new bond between Au and S with high affinity is built upon transfer, ensuring a complete replacement of citrate due to strong binding affinities. On the other hand, the free carboxylic acid can serve as an anchor for further coupling reactions with amines. In addition, the long alkyl chain provides enough flexibility for the active moiety to interact multivalently with the receptor. The ligand exchange with MUDA giving NP 2 proceeded completely as it is indicated in the infra-red (IR) spectra (Figure 57). The final step towards the fully functionalized nanoparticle was accomplished by peptide coupling with EDC (1-ethyl-3-(3-dimethylaminopropyl)carbodiimide) and NHS (*N*-hydroxysuccinimide). The free carboxylic acid is activated by EDC and forms with NHS in situ a so called ‘active ester’. This reacts easier with amine moieties of e. g. amino acids or peptides.

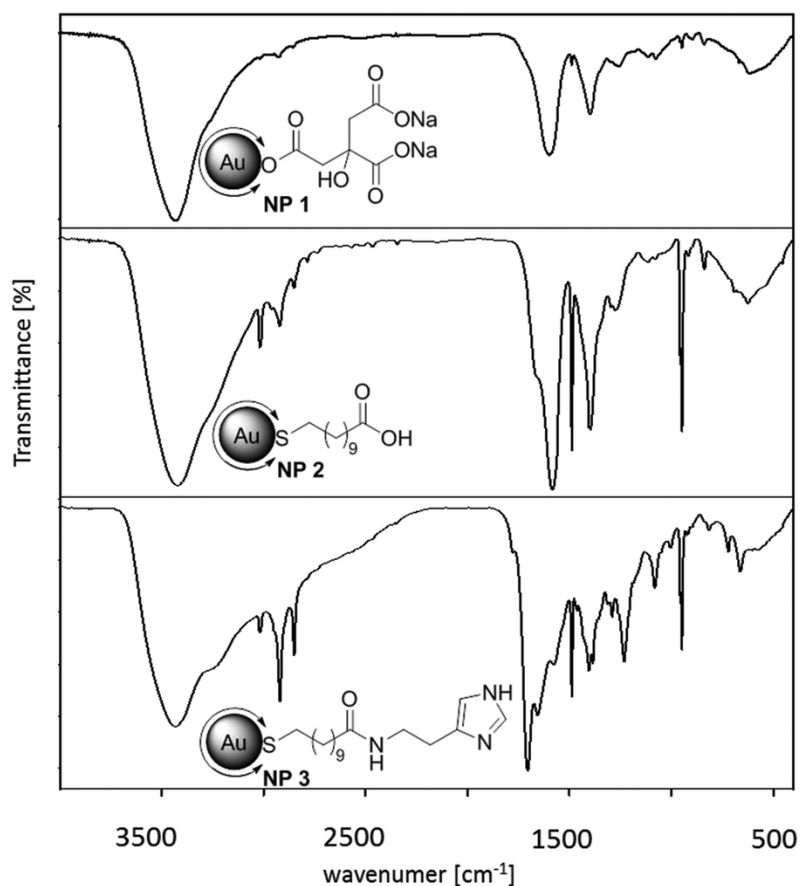


Figure 57: IR spectra of (a) Au–Citrate NP 1, (b) Au–MUDA NP 2 and (c) Au–MUDA–HA NP 3; vibration for the amide bond is found at 1641 cm^{-1} .

Although the prepared NHS ester is sufficiently stable for the reaction, it hydrolyses within hours depending on the pH of the reaction solution. To ensure the coupling, another equivalent of histamine, EDC and NHS were added after two hours. The excess of coupling agents and byproducts of the reaction were removed by purification with dialysis against water (MWCO 3500, three times). The characterization of the synthesized and functionalized nanoparticles NP 1–3 was performed with different methods. For the characterization of the core transmission electron microscope (TEM) images, dynamic light scattering (DLS) measurements and UV/Vis spectroscopy were used. The images shown in Figure 58 indicate that the synthesized nanoparticles have mostly a spherical shape; the average diameter determined by TEM is $14.0 \pm 0.9\text{ nm}$. The hydrodynamic diameter of the nanoparticles in solution obtained by DLS measurements was determined by $16.7 \pm 3.0\text{ nm}$. The absorption maximum was found at 524 nm. The position and form of the maximum is also a hint for the size of the nanoparticles, as it derives from a distinctive plasmon resonance at the gold surface depending on the shape of the material. The obtained data confirmed that the average diameter of the particles cores and the maxima of absorption remained unchanged after ligand exchange reaction and

functionalization. The slight shift can be explained due to the new ligand. The affinity to a gold surface is higher for thiolated ligands than for citrate and therefore effects on the plasmon resonance of the particle. Nonetheless, neither the exchange of the ligands nor the purification via dialysis had an effect on the agglomeration state. Also the functionalization at the ligand periphery did not alter the particles significantly. In addition to these methods, the success of the ligand exchange was verified by IR spectroscopy (Figure 57). Identification of the newly formed amide bond at 1641 cm^{-1} gives evidence for the successful coupling. Again the colloidal solution was purified by dialysis. Unlike the particles with MUDA as ligand shell, the final functionalization with histamine provides a good stability at physiological pH value and in a standard buffer solution for the *Ussing* chamber experiments (see below). The number of the ligands at the surface determined by TGA is about 10.000 for 14 nm gold nanoparticles, however determination is difficult due to small amounts of product. In order to find out whether the size of the nanoparticles could be a limiting factor for their properties, two other sizes were investigated. Following the same synthetic procedure as described above but with different reaction conditions, 25 nm nanoparticles were obtained. Also, 7 nm nanoparticles were prepared using dodecanethiol-protected particles from the *Stucky* method as basic material. [26]

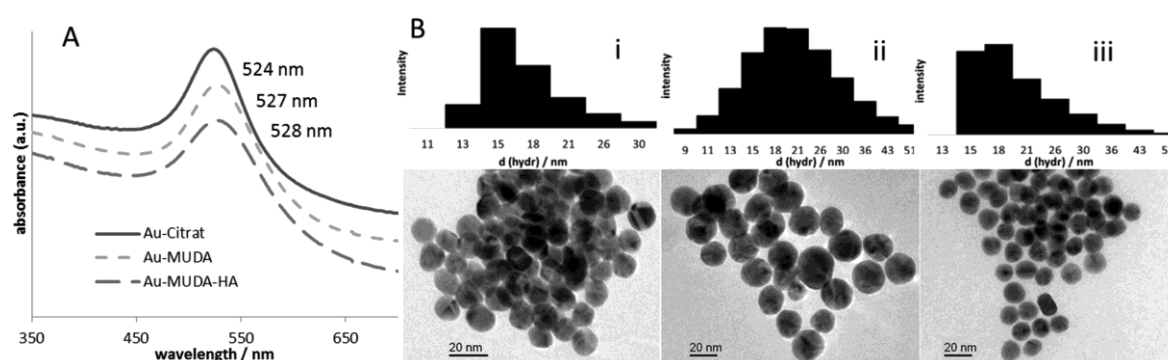


Figure 58: (A) UV/Vis spectra of the stepwise functionalization of Au–Citrate NP 1, Au–MUDA NP 2 and Au–MUDA–HA NP 3 nanoparticles. (B) TEM images and DLS measurements with values for the distribution of the hydrodynamic diameters of (i) Au–Citrate NP 1 $d = 14.0 \pm 0.9\text{ nm}$, $d_{\text{hydr}} = 16.7 \pm 3.0\text{ nm}$, (ii) Au–MUDA NP 2 $d = 14.5 \pm 1.2\text{ nm}$, $d_{\text{hydr}} = 24.1 \pm 6.7\text{ nm}$ and (iii) Au–MUDA–HA NP 3 $d = 14.3 \pm 0.7\text{ nm}$, $d_{\text{hydr}} = 19.3 \pm 2.9\text{ nm}$; d = diameter.

As a negative control for the biochemical application, gold nanoparticles NP 4 (Figure 59) with a sulfated ligand shell were synthesized. We already reported from sulfated ligands for the inhibition of selectin binding. [133] A structurally similar and simple ligand is sulfated 11-mercaptopundecanol (MUDOLS), which can be immobilized on gold nanoparticles in the same

way as mentioned before. Again citrate-stabilized gold nanoparticles NP 1 served as basic material.

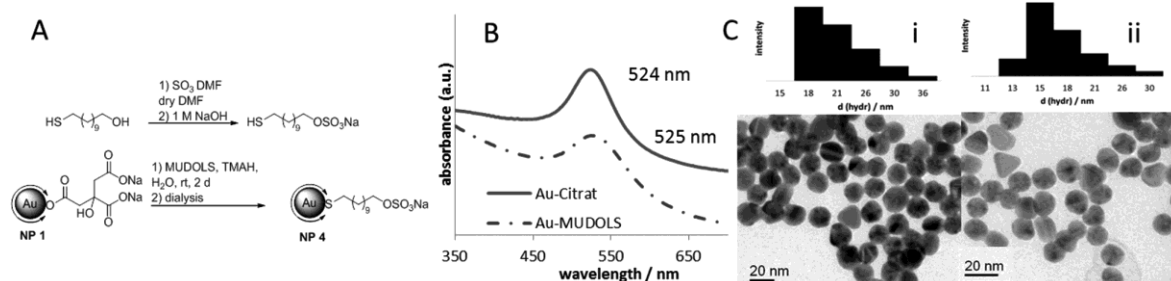


Figure 59: (A) Synthetic procedure for the preparation of Au-MUDOLS NP 4, (B) UV/Vis spectra of Au-Citrate NP 1 and Au-MUDOLS NP 4, (C) TEM images and DLS measurements with values for the distribution of the hydrodynamic diameters of (i) Au-Citrate NP 1 $d = 14.0 \pm 0.9$ nm, $d_{\text{hydr}} = 16.7 \pm 3.0$ nm, (ii) Au-MUDOLS NP 4 $d = 14.3 \pm 1.3$ nm, $d_{\text{hydr}} = 18.6 \pm 2.5$ nm; d = diameter.

The sulfated ligand was synthesized separately and then attached to the surface via ligand exchange reaction. TEM images, DLS measurements and UV/Vis spectra (Figure 59) indicated that the colloidal solution was intact and the nanoparticles were stable. Sulfated nanoparticles showed excellent stability over a wide range of pH value due to interparticle repulsion through a negatively charged ligand shell. Unlike the unsulfated Au-MUDA particles they are perfectly stable at physiological pH.

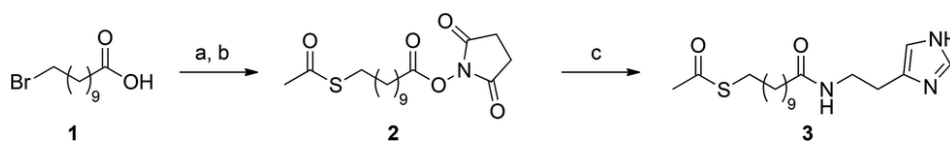


Figure 60: Synthesis of the monovalent analogue AcS-MUDA-HA (3) starting from 11-bromoundecanoic acid 1. Reaction conditions: (a) KSOAc, DMF, 2 h, rt, (b) NHS, DCM, 18 h, rt, (c) EDC, HA·2HCl, NEt₃, DCM, 6 h, rt.

When looking at multivalent effects, the monovalent ligand 3 (Figure 60) also has to be investigated. Thus the complete ligand was synthesized separately. To prevent the formation of a disulfide bond between two molecules, the thiol moiety was protected with an acetyl group.

Functionality of the histamine-nanoparticles

From all the synthesized nanoparticles of different sizes, only the 14 nm nanoparticles yielded consistent effects on short-circuit current (I_{sc}) when they were administered to rat colonic mucosa mounted in *Ussing* chambers. Therefore, this type of particles was used for all subsequent experiments. To investigate the functionality of the Au-MUDA-HA nanoparticles, their ability to induce chloride secretion was compared with that of native histamine, which induces a strong chloride secretion across rat colonic epithelium. [151, 152] Indeed, the histamine-conjugated nanoparticles induced a concentration-dependent increase in I_{sc} , which is a measure for net ion transport across the epithelium (Figure 61).

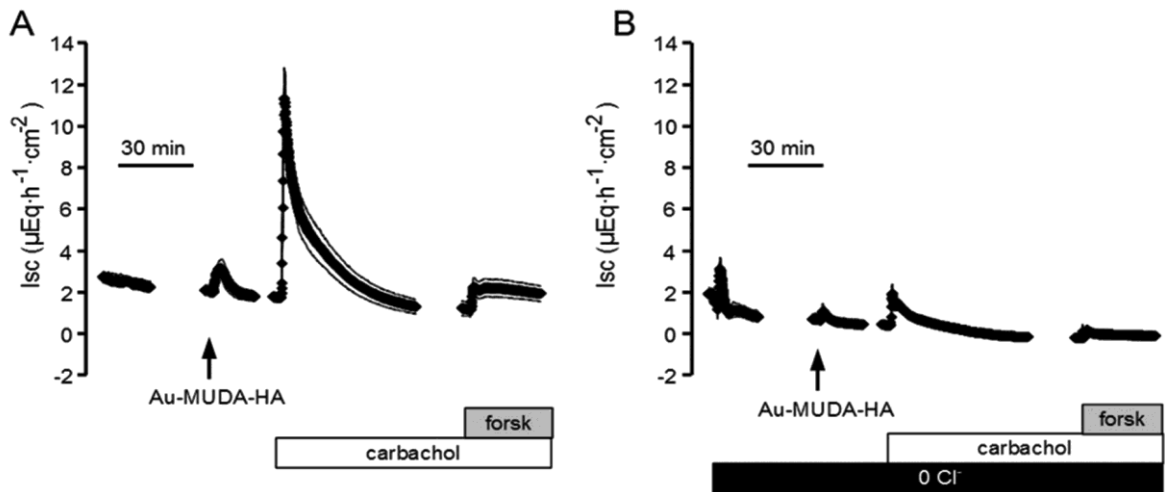


Figure 61: Au-MUDA-HA ($10^{-11} \text{ mol l}^{-1}$ at the serosal side, arrow) induced an increase in I_{sc} (A), which was almost abolished in the absence of chloride (0 Cl^- ; black bar, (B). At the end of the experiments, the secretagogues carbachol ($5 \times 10^{-5} \text{ mol l}^{-1}$ at the serosal side, white bars) and forskolin (forsk; $5 \times 10^{-6} \text{ mol l}^{-1}$ at the mucosal and the serosal side, grey bars, (A & B), known to induce chloride secretion, were administered. Line interruptions are caused by omission of time intervals in order to synchronize the tracings of individual records to the administration of drugs. Values are means (symbols) \pm SEM (parallel continuous lines), $n = 6-8$.

These changes in I_{sc} reflect a secretion of chloride ions as they were abolished in Cl^- -free buffer solution (Figure 61). However, repetitive administration of these particles led to a desensitization of the tissue (Table 7). Thus in all subsequent experiments, each tissue was only exposed once to a single concentration of the Au-MUDA-HA nanoparticles ($10^{-11} \text{ mol l}^{-1}$ at the serosal side). The tissue conductance (G_t) was not significantly changed by the nanoparticles ($10^{-11} \text{ mol l}^{-1}$ at the serosal side); G_t amounted to $14.4 \pm 1.87 \text{ mS cm}^{-2}$ before and $14.7 \pm 1.96 \text{ mS cm}^{-2}$ after administration of the particles ($n = 6$; difference not significant). Viability of the tissue was also not impaired by the Au-MUDA-HA nanoparticles as both the

Ca^{2+} -dependent secretagogue carbachol ($5 \times 10^{-5} \text{ mol l}^{-1}$ at the serosal side), i.e. a stable derivative of acetylcholine, [154], [151] as well as the cAMP-dependent secretagogue forskolin ($5 \times 10^{-6} \text{ mol l}^{-1}$ at the mucosal and the serosal side), which stimulates the intracellular production of cAMP, [155] induced a prompt rise in I_{sc} in all tissues (Figure 61). As the response to histamine evokes chloride secretion in part via stimulation of histamine receptors located on submucosal neurons, the effect of the inhibitory neurotoxin tetrodotoxin, which inhibits the propagation of action potentials via blockade of voltage-dependent Na^+ channels, on the I_{sc} evoked by the Au-MUDA-HA nanoparticles was investigated. [151, 156] Indeed, in the presence of tetrodotoxin ($10^{-6} \text{ mol l}^{-1}$ at the serosal side), the I_{sc} evoked by Au-MUDA-HA ($10^{-11} \text{ mol l}^{-1}$ at the serosal side) only amounted to $0.69 \pm 0.20 \text{ } \mu\text{Eq h}^{-1} \text{ cm}^{-2}$ ($n = 6$) in comparison to $2.92 \pm 0.64 \text{ } \mu\text{Eq h}^{-1} \text{ cm}^{-2}$ in untreated control tissues ($P < 0.05$, $n = 6$).

Table 7: Effects of additive concentrations of Au–MUDA–HA 14 nm on I_{sc} and H_1 and H_2 receptors.

	Increase in short-circuit current ΔI_{sc} ($\mu\text{Eq h}^{-1} \text{ cm}^{-2}$)		
	Au-MUDA-HA 14 nm		
No inhibitor	1.09 ± 0.43^b	$0.61 \pm 0.11^{a,b}$	$0.42 \pm 0.11^{a,b}$
Mepyramine + cimetidine	0.083 ± 0.041^a	0.13 ± 0.033^a	0.13 ± 0.02^a
Cumulative administration of gradually increased concentrations (10^{-11} , 5×10^{-11} , $10^{-10} \text{ mol l}^{-1}$, at the serosal side) of Au–MUDA–HA induced an increase in I_{sc} concomitant with an obvious desensitization of the tissue as indicated by the reduced I_{sc} response after repeated administration. Given is the control response in the absence of any inhibitors and the response to Au–MUDA–HA in the combined presence of mepyramine ($10^{-4} \text{ mol l}^{-1}$ at the serosal side) and cimetidine ($10^{-4} \text{ mol l}^{-1}$ at the serosal side). Values are given as difference to the baseline in I_{sc} just before administration of the corresponding agonist (ΔI_{sc}) and are means \pm SEM, $n = 6$. Different letters (a, b, c) indicate statistically homogenous groups (analysis of variances followed by post hoc test of Tukey).			

The response to native histamine is mediated by stimulation of histamine H_1 and histamine H_2 receptors. [155] In accordance with that observation, the increase in I_{sc} evoked by Au-MUDA-HA ($10^{-11} \text{ mol l}^{-1}$ at the serosal side) was strongly inhibited by a combination of the histamine H_1 receptor blocker, mepyramine ($10^{-4} \text{ mol l}^{-1}$ at the serosal side), and the histamine H_2 receptor blocker, cimetidine ($10^{-4} \text{ mol l}^{-1}$ at the serosal side, Table 7). Mepyramine is a substituted ethylamine derivative, whereas cimetidine has an imidazole ring system similar to native histamine. [157] Both drugs act as competitive inhibitors of the G-protein coupled histamine receptors type 1 [157] and type 2, [158] respectively. Viability of the tissue was not altered, as forskolin, the activator of adenylate cyclase(s), [155] evoked an increase in I_{sc} of

$11.90 \pm 1.10 \mu\text{Eq h}^{-1} \text{cm}^{-2}$ ($n = 6$) in the absence and of $10.72 \pm 1.18 \mu\text{Eq h}^{-1} \text{cm}^{-2}$ ($n = 6$, difference not significant) in the presence of the histamine receptors antagonists.

Controls with histamine-free nanoparticles

In order to make sure that the effects of the nanoparticles are not unspecific artefacts resulting from the assembly components of the particles, controls were performed either with the conjugator AcS-MUDA-HA or with the sulfated moiety Au-MUDOLS. As shown in Figure 62, these components failed to induce a rise in I_{sc} . Furthermore, Au-MUDOLS impaired the viability of the epithelium as it prevented the secretion induced by a subsequent administration of forskolin ($5 \times 10^{-6} \text{ mol l}^{-1}$ at the mucosal and the serosal side).

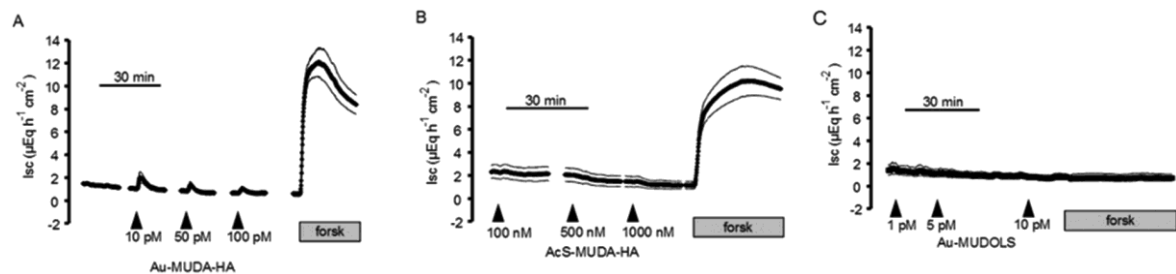


Figure 62: Au-MUDA-HA (10^{-11} , 5×10^{-11} , $10^{-10} \text{ mol l}^{-1}$, administered cumulatively at the serosal side, arrows) induced an increase in I_{sc} . (B) AcS-MUDA-HA (10^{-7} , 5×10^{-7} , $10^{-6} \text{ mol l}^{-1}$, at the serosal side, arrows) was ineffective. (C) Au-MUDOLS (10^{-12} , 5×10^{-12} , $10^{-11} \text{ mol l}^{-1}$, at the serosal side, arrows) failed to change the I_{sc} . All particles except Au-MUDOLS preserved the secretory function of the tissues as they did not impair the effect of the secretagogue forskolin (forsk; $5 \times 10^{-6} \text{ mol l}^{-1}$ at the mucosal and the serosal side, grey bars).

Values are means (symbols) \pm SEM (parallel continuous lines), $n = 4-8$.

Potency of the Au-MUDA-HA nanoparticles

The highest changes in the I_{sc} or the G_t induced by the nanoparticles were obtained at the concentration $10^{-11} \text{ mol l}^{-1}$. For the I_{sc} , the change amounted to $1.09 \pm 0.42 \mu\text{Eq h}^{-1} \text{cm}^{-2}$. When comparing this response with a concentration-response curve of native histamine (Figure 63) it turned out that a comparable increase in I_{sc} ($1.05 \pm 0.24 \mu\text{Eq h}^{-1} \text{cm}^{-2}$) was obtained with histamine in a concentration of $10^{-5} \text{ mol l}^{-1}$ (Figure 63). Assuming a maximum of 10 000 histaminic units at the surface determined by TGA, the relative potency is still some magnitudes higher. In other words, the conjugation to the 14 nm nanoparticles strongly enhanced the potency of histamine to evoke anion secretion.

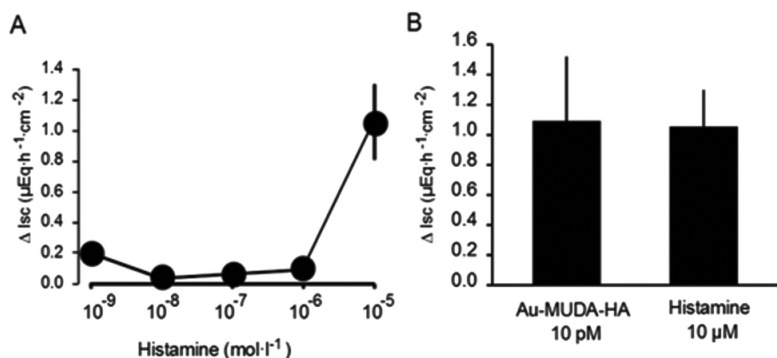


Figure 63: (A) Histamine induced a concentration-dependent increase in I_{sc} . (B) shows the potency of Au–MUDA–HA versus histamine; an equivalent potency between Au–MUDA–HA and histamine was obtained with 10^{-11} mol l^{-1} and 10^{-5} mol l^{-1} , respectively. Values are given as increase in I_{sc} above baseline in short-circuit current (ΔI_{sc}) just before administration of the corresponding drug and are means \pm SEM, $n = 6$ –8.

Conclusion

The gold nanoparticles with an average diameter of 14 nm were loaded with the histamine derivative and showed excellent activation properties in the *Ussing* chamber experiments. Compared to native histamine, the nanoparticles were more effective at extremely low concentrations. It was found that the newly developed conjugate was able to induce a concentration-dependent chloride secretion across rat colonic epithelium via stimulation of histamine H_1 and H_2 receptors. These receptors, which are composed of 487 or 359 amino acids, respectively, belong to the class of G-protein coupled receptors with seven transmembrane spanning regions. Upon binding of the agonist, these receptors induce the exchange of guanosine diphosphate (GDP) against guanosine triphosphate (GTP) at the α -subunit of trimeric GTP-binding proteins. The consequence is the dissociation of the G-protein in the GTP-binding α -subunit and a β/γ -complex and the activation of intracellular enzymes such as phospholipase C or adenylate cyclase, which then activate intracellular second messenger pathways. [159] An explanation for this stimulation might be the high local density of the immobilized ligand. The molecular recognition between the receptors on the surface and ligands bound to the nanoparticles is strengthened through the geometric arrangement given by the spherical shape. The density of the binding moieties allows simultaneous binding resulting in a lower activation concentration. [107] The interaction can be blocked with same inhibitors used for native histamine. To ensure the response originated only from multivalent histamine supported on gold nanoparticles and not from any unspecific interactions with the biological tissue, the monovalent ligand AcS-MUDA-HA or the gold nanoparticles with a simple sulfated moiety from 11-mercaptoundecanol were synthesized and tested in parallel. Indeed, no chloride secretion could be observed. All particles tested in this study preserved the basic functions of the tissues except for Au-MUDOLS. Only the particles with the sulfated moiety harmed the

tissues irreversibly. Among the three sizes of particles tested (7 nm, 14 nm and 25 nm), only the intermediate size 14 nm showed consistent effects on transepithelial Cl^- secretion, indicating a size-dependence. The smaller nanoparticles exhibited unspecific interactions whereas the bigger particles evoked no signal in the *Ussing* chamber experiments. The observed size dependence might correlate with the number of histamine molecules at the surface. The density of immobilized histamine moieties at 14 nm core size and the spatial arrangement are both essential for the activation of histaminic receptors bound on an epithelium. For a detailed insight into the mechanisms of receptor activation further experiments will be conducted on the ligand–receptor-complex which is formed during the activation process. But also the length of the spacer between the particle core and the active moiety influences the interplay, as it was shown in one of our previous studies on multivalent interactions of gold nanoparticles in selectin binding. [133] Further investigations shall be conducted on this influence. In summary the present work is another example for the influence of multivalent interactions in biological systems. This concept can also be transferred to other receptor antagonists and to different neurotransmitters.

Experimental section

All reactions of nanoparticles in aqueous solution were carried out in purified Millipore water. Organic solvents were distilled before use. All chemicals were purchased from commercial sources and used as received. The ligand exchange reactions and coupling reactions were done under inert conditions. All glass vessels were washed with aqua regia and distilled water prior to use. NMR spectra were recorded on Bruker BioSpin Avance III AV600 (600 MHz), AV400 (400 MHz) or AV200 (200 MHz) spectrometers using tetramethylsilane (TMS) as an internal standard with chemical shifts given in ppm relative to TMS ($\delta = 0.00$ ppm) or the respective solvent peaks. ^1H NMR data are reported as follows: chemical shifts (multiplicity [ppm], coupling constants [Hz], integration, classification). Multiplicity is recorded as s = singlet, br s = broadened singlet, d = doublet, t = triplet, q = quartet, m = multiplet. For ^{13}C NMR, chemical shifts and structural assignments are reported where applicable. Because of the rigidity of the alkyl chains in the thiol shells and the resulting large differences in the relaxation times of different protons, no integrals are given for the proton NMR data of the gold colloids. IR spectra were obtained on a Bruker IFS48 spectrometer in ATR mode. Electrospray ionization mass spectra (ESI-MS) were recorded on a Finnigan LCQDuo spectrometer using methanol solutions of the respective. TEM measurements were performed on a Philips CM30 STEM (300 kV, LaB_6 -cathode) equipped with a GATAN digital camera. TEM images were recorded using a digital micrograph. The average particle core sizes were determined by measuring at least 100 individual particles from recorded TEM images. The UV/Vis spectra were plotted with an

Agilent 8453 spectrophotometer (Agilent Technologies Inc., Santa Clara, CA, USA). Dynamic light scattering measurements were performed with a StabiSizer PMX 200C from Particlemetrix (Meerbusch, Germany).

Chemical syntheses

Citrate-coordinated gold nanoparticles NP 1 (Au–Citrate Ø 14 nm). Citrate-coordinated gold nanoparticles were synthesized by a variation of a procedure first published by Turkevich. A solution of 50 mg (0.127 mmol) HAuCl₄·3H₂O in 195 mL of Millipore water was heated to reflux for 20 min. Under vigorous stirring a solution of 224 mg (0.52 mmol) of sodium citrate in 5 mL of Millipore water was added quickly. The reaction mixture was held at 80 °C for 2 h. Then the solution was cooled to 0 °C in an ice bath and filtered (0.2 µm pore size). A clear red solution with a particle concentration of 2.7 nM was obtained and stored at 4 °C.

¹H NMR (400 MHz, D₂O): δ/ppm = 2.61 (bs, CH₂); IR (KBr disc, v/cm⁻¹): 3426.8 (ν_{O-H}), 1598.2 (ν_{C=O}), 1397.6, 1258.4, 618.0; TEM: d = 14.0 ± 0.9 nm; UV/Vis: λ_{max} = 522 nm; DLS: d_{hydr} = 16.7 ± 3.0 nm.

11-Mercaptoundecanoic acid coordinated gold nanoparticles NP 2 (Au–MUDA Ø 14 nm). An amount of 21 mg 11-mercaptoundecanoic acid (0.1 mmol, 10⁵ equiv.) was dissolved in 8.5 mL Millipore water under the addition of 50 µL tetramethylammonium hydroxide (TMAH). 5 mL of a 2.7 nM solution of citrate-protected gold nanoparticles in water was added dropwise and the solution was stirred for 24 h. The nanoparticles solution was dialysed against 300 mL water three times (3500 MWCO). A clear red solution with a particle concentration of 1 nM was obtained and stored at 4 °C.

¹H NMR (400 MHz, D₂O): 3.17 (s, 16H, TMAH), 2.76 (t, CH₂), 2.16 (t, CH₂), 1.73 (quin, CH₂), 1.54 (m, CH₂), 1.40 (m, CH₂), 1.30 (bs, CH₂); IR (KBr disc, v/cm⁻¹): 3422.8, 3018.5, 2920.1 & 2849.8 (ν_{C-H}), 1583.5 (ν_{C=O}), 1487.9, 1396.2, 1274.9, 956.8, 948.2, 625.0; TEM: d = 14.5 ± 1.2 nm, UV/Vis: λ_{max} = 527 nm, DLS: d_{hydr} = 24.1 ± 6.7 nm.

Sodium 11-mercaptoundecyl sulfate coordinated gold nanoparticles NP 4 (Au–MUDOLS Ø 14 nm). An amount of 30 mg 11-mercaptoundecanyl sulfate was dissolved in 8.5 mL Millipore water and 50 µL tetramethylammonium hydroxide (TMAH) was added. 5 mL of a 2.7 nM solution of citrate-protected gold nanoparticles in water was added dropwise and the solution was stirred for 24 h. The nanoparticles solution was dialysed against 300 mL water three times (3500 MWCO) and stored at 4 °C.

¹H NMR (400 MHz, D₂O): δ/ppm = 4.00–3.89 (m, CH₂), 2.70–2.60 (m, CH₂), 1.68–1.51 (m, CH₂), 1.37–1.23 (m, CH₂); IR (KBr disc, v/cm⁻¹): 2918.7 & 2849.9 (ν_{C-H}), 1614.8 (ν_{C=O}),

1470.0, 1261.7 & 1205.1 & 1128.1 ($\nu_{\text{R-OSO}_2\text{-OR}}$), 1068.8, 966.4, 831.8, 718.9, 628.7, 586.3; TEM: $d = 14.3 \pm 1.3$ nm; UV/Vis: $\lambda_{\text{max}} = 525$ nm; DLS: $d_{\text{hydr}} = 18.6 \pm 2.5$ nm.

Synthesis of histamine functionalized gold nanoparticles NP 3 (Au–MUDA–HA Ø 14 nm).

10 mL of a 1 nM solution Au–MUDA were set in a glass vessel washed with aqua regia and distilled water. 18 mg histamine dihydrochloride (0.1 mmol), 17 mg EDC (0.11 mmol) and 15 mg HOBt (0.11 mmol) and 50 μL NEt_3 were added to the nanoparticle solution. The reaction mixture was stirred overnight and subsequently dialysed against water three times (3500 MWCO) and stored at 4 °C.

^1H NMR (400 MHz, D_2O): 7.55 (s, 1H, CH), 6.81 (s, 1H, CH), 2.73–2.86 (m, 2H, $\text{CH}_2(\text{HA})$), 2.57–2.71 (m, 3H, $\text{CH}_2(\text{HA}) + \text{NH}$), 2.41–2.53 (m, 2H), 2.21–2.34 (m, 4H), 2.10–2.21 (m, 3H), 2.03 (t, $J = 7.7$, 1H), 1.52–1.68 (m, 1H), 1.36–1.48 (m, 1H), 1.18 (bs, 8H, CH_2), IR (KBr disc, ν/cm^{-1}): 3018.8, 2921.4 & 2850.0 ($\nu_{\text{C-H}}$), 1641.1 ($\nu_{\text{C=O}}$, amide), 1596.3 ($\nu_{\text{CO-NH}}$), 1488.2, 1404.2, 957.1, 948.6, TEM: $d = 14.3 \pm 0.7$ nm, UV/Vis: $\lambda_{\text{max}} = 528$ nm, DLS: $d_{\text{hydr}} = 19.3 \pm 2.9$ nm.

Sodium 11-mercaptoundecyl sulfate (MUDOLS). In a flame-dried vessel under argon atmosphere, 353 mg of 11-mercaptoundecanol (1.72 mmol, 1 equiv.) was dissolved in 3 mL dry DMF. Separately, 395 mg of $\text{SO}_3 \cdot \text{DMF}$ complex (2.5 mmol, 1.5 equiv.) were dissolved in 1 mL dry DMF and added to the solution. After stirring for 1 h at room temperature the solvent was removed under reduced pressure (OPV) and the residue was dissolved in 4 mL of 1 M NaOH. A white precipitate appeared. 15 mL of ethanol were added and washed three times. The product was dried in vacuum. 280 mg of a colorless solid (0.91 mmol, 53%) could be obtained. The dimer was formed.

^1H NMR (200 MHz, DMSO-d_6): $\delta/\text{ppm} = 3.68$ (t, $J = 6.6$ Hz, 2 H, CH_2), 3.35 (t, $J = 6.3$ Hz, 2H, CH_2), 2.27–2.61 (m, 4H, CH_2), 2.56–2.49 (m, 2H, CH_2), 1.67–1.52 (m, 4H, CH_2), 1.36–1.24 (m, 10H, CH_2); ^{13}C NMR (200 MHz, DMSO-d_6): $\delta/\text{ppm} = 65.6, 60.7, 32.5, 29.1, 29.0, 28.9, 28.8, 28.6, 28.5, 27.7, 25.5$; ESI-MS: $m/z = 633.1593$ ($[\text{M} + \text{Na}]^+$, calcd 633.1612).

11-(Acetylthio)undecanoic acid (AcS–MUDA). 500 mg 11-bromoundecanoic acid (1.89 mmol, 1 equiv.) were dissolved in 70 mL absolute DMF under argon atmosphere. Separately 520 mg potassium thioacetate (4.56 mmol, 2.4 equiv.) were suspended in 8 mL absolute DMF under argon atmosphere and added dropwise to the first solution. The reaction mixture was stirred for 2 hours at room temperature. The precipitate was filtered off, washed several times with water and dried in vacuum. 414 mg of a colorless solid (1.59 mmol, 84%) could be obtained.

^1H NMR (200 MHz, CDCl_3): $\delta/\text{ppm} = 2.79$ (t, $J = 7.17$, 2H, CH_2), 2.27 (t, $J = 7.17$, 2H, CH_2), 2.25 (s, 3H, CH_3), 1.61–1.52 (m, 2H, CH_2), 1.52–1.44 (m, 2H, CH_2), 1.32–1.16 (m, 12H, CH_2);

^{13}C NMR (100 MHz, CDCl_3): δ/ppm = 196.2 (C_q , $\text{C}=\text{O}$, acetyl), 179.4, 33.9, 30.7, 29.5, 29.4, 29.3, 29.2, 29.1, 29.1, 29.0, 28.8, 24.7; ESI-MS: m/z = 283.1335 ($[\text{M} + \text{Na}]^+$, calcd 283.1344).

2,5-Dioxopyrrolidin-1-yl-11-(acetylthio)undecanoate (AcS–MUDA–NHS). 195 mg NHS (1.7 mmol, 1.1 equiv.) and 700 mg AcS–MUDA (1.55 mmol, 1 equiv.) were dissolved in DCM under stirring at room temperature. 350 mg DCC (1.7 mmol, 1.1 equiv.) were separately dissolved in 5 mL DCM and added slowly. After 30 min a white precipitate appeared. The reaction mixture was stirred overnight. The solvent was removed under reduced pressure. 506 mg (1.42 mmol, 92%) of a colorless powder were obtained.

^1H NMR (400 MHz, CDCl_3): δ/ppm = 2.81–2.77 (m, CH_2), 2.53 (t, J = 7.34, 2H, CH_2), 2.25 (s, 3H, CH_3), 1.71–1.63 (m, 2H, CH_2), 1.52–1.47 (m, 2H, CH_2), 1.38–1.17 (m, 12H, CH_2); ^{13}C NMR (100 MHz, CDCl_3): δ/ppm = 196.1 (C_q , $\text{C}=\text{O}$, acetyl), 169.3 ($2 \times \text{C}_q$, $\text{C}=\text{O}$), 168.7 (C_q , $\text{C}=\text{O}$), 30.9 (CH_3), 30.7, 29.5, 29.3, 29.2, 29.2, 29.1, 29.0, 28.8, 28.7, 25.6 ($2 \times \text{CH}_2$), 24.6; ESI-MS: m/z = 380.1502 ($[\text{M} + \text{Na}]^+$, calcd 380.1508).

S-(11-((2-(1H-Imidazol-4-yl)ethyl)amino)-11-oxoundecyl) ethanethioate 4 (AcS–MUDA–HA). 97 mg AcS–MUDA (0.27 mmol, 1 equiv.) were dissolved in DMF to form a clear solution. 34 mg HA·2HCl (0.30 mmol, 1.1 equiv.) and a few drops NEt_3 were added and the solution was stirred overnight. Subsequently 50 mL water were added and a white solid appeared. The precipitate was filtered off and washed three times with water. The crude product was dissolved in CHCl_3 , filtered again and purified via column chromatography ($\text{CHCl}_3/\text{MeOH}$ 9/1 R_f = 0.7). After evaporation 70 mg (0.19 mmol, 70%) of a colorless powder were obtained.

^1H NMR (400 MHz, CDCl_3): δ/ppm = 7.50 (s, 1H, CH), 6.75 (s, 1H, CH), 6.33 (br s, 1H, NH), 3.52–3.42 (m, 2H, $\text{CH}_2(\text{HA})$), 2.79–2.69 (m, 2H, $\text{CH}_2(\text{HA})$), 2.53–2.39 (m, 2H, CH_2), 2.56 (s, 3H, CH_3), 2.10 (t, J = 7.24 Hz, 2H, CH_2), 1.59–1.43 (m, 4H, CH_2), 1.26–1.14 (m, 12H, CH_2); ^{13}C NMR (100 MHz, CDCl_3): δ/ppm = 196.4 (C_q , $\text{C}=\text{O}$, acetyl), 173.7 (C_q , $\text{C}=\text{O}$, amide), 134.8 (CH, C_{ar}), 127.6 (C_q , C_{ar}), 118.6 (CH, C_{ar}), 39.2 ($\text{CH}_2(\text{HA})$), 36.9 ($\text{CH}_2(\text{HA})$), 30.7 (CH_3), 29.5, 29.3, 29.3, 29.2, 29.1, 28.7, 28.4, 26.9, 25.7; ESI-MS: m/z = 354.2221 ($[\text{M} + \text{H}]^+$, calcd 354.2210).

Animals

Female and male Wistar rats with a body mass of 200–250 g were used. The animals were bred and housed at the institute for Veterinary Physiology and Biochemistry of the Justus-Liebig-University Giessen at an ambient temperature of 22.5 °C and air humidity of 50–55% on a 12 h : 12 h light–dark cycle with free access to water and food until the time of the experiment. Experiments were approved by the named animal welfare officer of the Justus Liebig University

(administrative number 487_M) and performed according to the German and European animal welfare law.

Solutions

The standard solution for the *Ussing* chamber experiments was a buffer solution containing (mmol l⁻¹): NaCl 107, KCl 4.5, NaHCO₃ 25, Na₂HPO₄ 1.8, NaH₂PO₄ 0.2, CaCl₂ 1.25, MgSO₄ 1 and glucose 12. The solution was gassed with carbogen (5% CO₂ in 95% O₂, v/v); pH was 7.4. For the Cl⁻-free buffer, NaCl and KCl were substituted by Na gluconate and K gluconate (KGluc), respectively. The Ca²⁺ concentration in the Cl⁻-free buffer was increased to 5.75 mmol l⁻¹ to compensate for the Ca²⁺-buffering properties of gluconate. [160]

Tissue preparation

Animals were killed by stunning followed by exsanguination. The serosa and tunica muscularis were stripped away by hand to obtain a mucosa–submucosa preparation of the distal colon. Briefly, the colon was placed on a small plastic rod with a diameter of 5 mm. A circular incision was made near the anal end with a blunt scalpel, and the serosa together with the tunica muscularis was gently removed in a proximal direction. Two segments of the distal colon of each rat were prepared.

Short-circuit current measurements

The mucosa–submucosa preparation was fixed in a modified *Ussing* chamber bathed with a volume of 3.5 ml on each side of the mucosa. The tissue was incubated at 37 °C and short-circuited by a computer-controlled voltage-clamp device (Ingenieur Büro für Mess- und Datentechnik Mussler, Aachen, Germany) with correction for solution resistance. Tissue conductance (G_t) was measured every minute by the voltage deviation induced by a current pulse ($\pm 50 \mu\text{A}$, duration 200 ms) under open-circuit conditions. Short-circuit current (I_{sc}) was continuously recorded on a chart-recorder. I_{sc} is expressed as $\mu\text{Eq h}^{-1} \text{cm}^{-2}$, i.e. the flux of a monovalent ion per time and area, with $1 \mu\text{Eq h}^{-1} \text{cm}^{-2} = 26.9 \mu\text{A cm}^{-2}$. At the end of each experiment, tissue viability was tested by administration of the cholinergic agonist, carbachol ($5 \times 10^{-5} \text{ mol l}^{-1}$ at the serosal side) and/or the administration of forskolin ($5 \times 10^{-6} \text{ mol l}^{-1}$ at the mucosal and the serosal side), an activator of adenylate cyclase(s), which induce a strong Ca²⁺-respective cAMP-dependent Cl⁻ secretion. [154, 155]

Drugs

Au–MUDOLS, Au–MUDA–HA, carbachol, cimetidine, histamine dihydrochloride, and mepyramine were dissolved in aqueous stock solutions. Forskolin (Calbiochem, Bad Soden, Germany) was dissolved in ethanol (final maximal concentration 0.25%, v/v). Tetrodotoxin was

dissolved in $2 \times 10^{-2} \text{ mol l}^{-1}$ citrate buffer. If not indicated otherwise, drugs were from Sigma, (Taufkirchen, Germany).

Statistics

Results are given as means \pm SEM, with the number (n) of investigated tissues. When means of several groups had to be compared, an analysis of variance was performed followed by post hoc Tukey's-test. For the comparison of two groups, a Mann-Whitney U-test was applied. $P < 0.05$ was considered to be statistically significant.

Acknowledgements

We wish to acknowledge Anne Schulze (Institute of Inorganic and Analytical Chemistry, Justus-Liebig-University at Giessen) for the TEM images.

5. Quantum Dots

5.1 Quantum Dots for Cellular Imaging

Due to their unique optical properties quantum dots (QDs) consisting of CdTe were synthesized and applied as new cell dyes. Preliminary work was done on the development of a synthesis for the preparation of monodisperse quantum dots of Cd and Te or Se. [161] Based on the developed method the chalcogenide precursor was added to a aqueous solution of Cd^{2+} and mercaptocarboxylic acid. Three different types were applied: 2-Mercapto-1-acetic acid (thioglycolic acid, TGA), 3-mercapto-1-propanoic acid (MPA) and 3-mercapto-1-propanesulfonic acid (MPSA) (Figure 64).

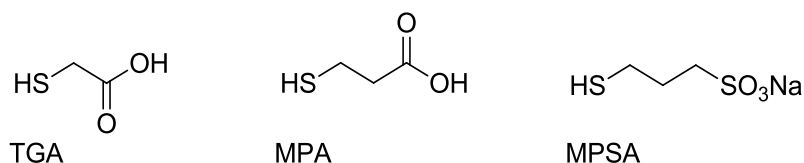


Figure 64: Mercaptocarboxylic acids and -sulfonic acid used for the synthesis of quantum dots.

The reaction mixture was stirred at 100 °C for 3 hours and then cooled down with an ice bath, subsequently the colloidal solution was purified carefully via dialysis against water. Within the molar ratios of 2:1:4.8 for Cd:Te:ligand different rates for the growth of the nanoparticles could be observed. Depending on the ligand the size of the resulting quantum dots can be tuned. [161] The longer the alkyl chain of the ligand the smaller the particles get within the same reaction time. With increasing reaction time the nanoparticles grow larger.

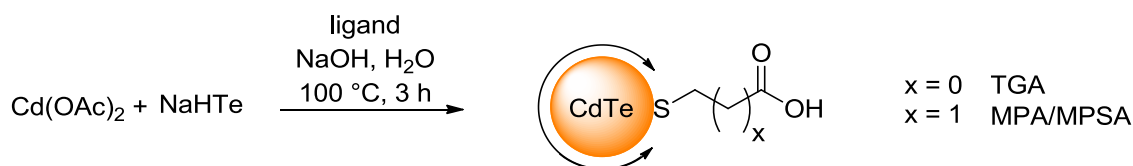


Figure 65: Reaction scheme for the synthesis of CdTe quantum dots in aqueous solution.

CdTe quantum dots with three different surface ligands (Figure 65). All of them showed high emission intensities. For the shortest chain length (TGA) the longest wavelength for the absorption and emission maxima were achieved, indicating different particle growth with different ligands (Figure 66).

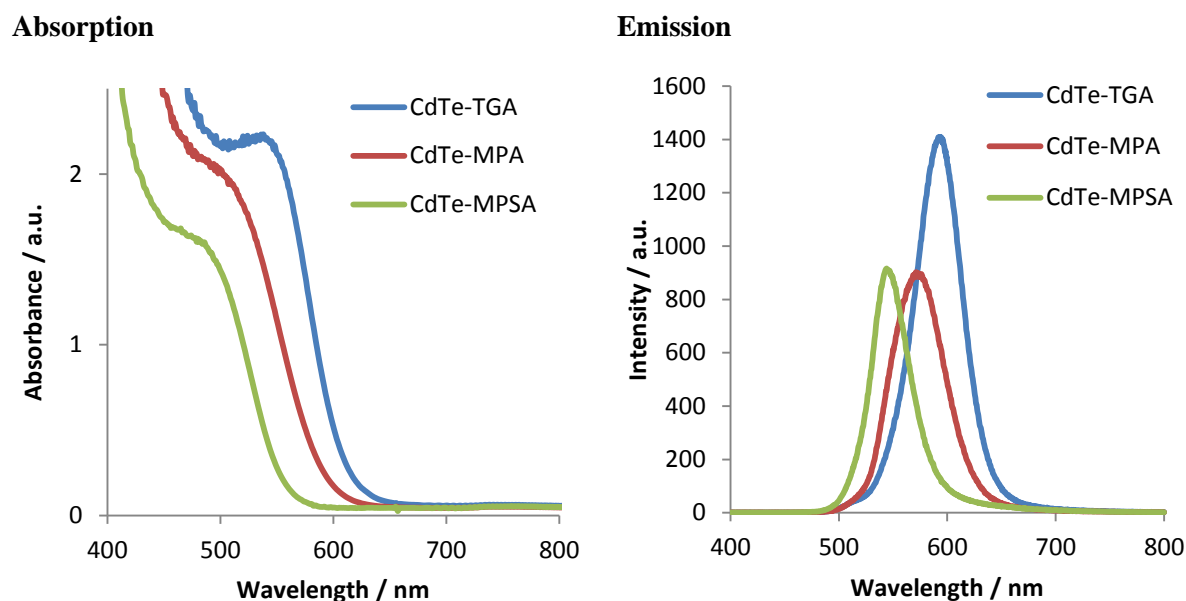


Figure 66: Absorption and emission spectra of CdTe quantum dots.

Additionally CdSe quantum dots were synthesized via the same procedure, but only two different ligands were applied (Figure 67).

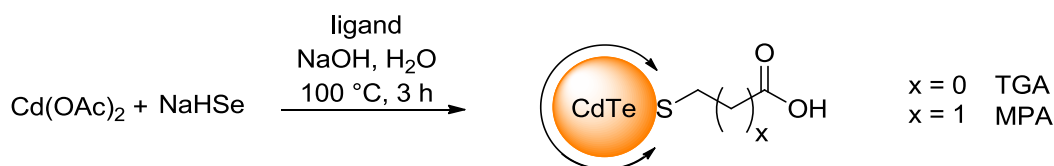


Figure 67: Reaction scheme for the synthesis of CdSe quantum dots in aqueous solution.

The selenide precursor solution is very sensitive to air and must be handled carefully under argon atmosphere. The spectra show only for MPA-stabilized quantum dots absorption properties and

emission intensity (Figure 68). TGA-capped quantum dots could not be obtained. In the absorption spectra a red shift can also be observed for shorter chain length indicating the same particle growth as for CdTe quantum dots.

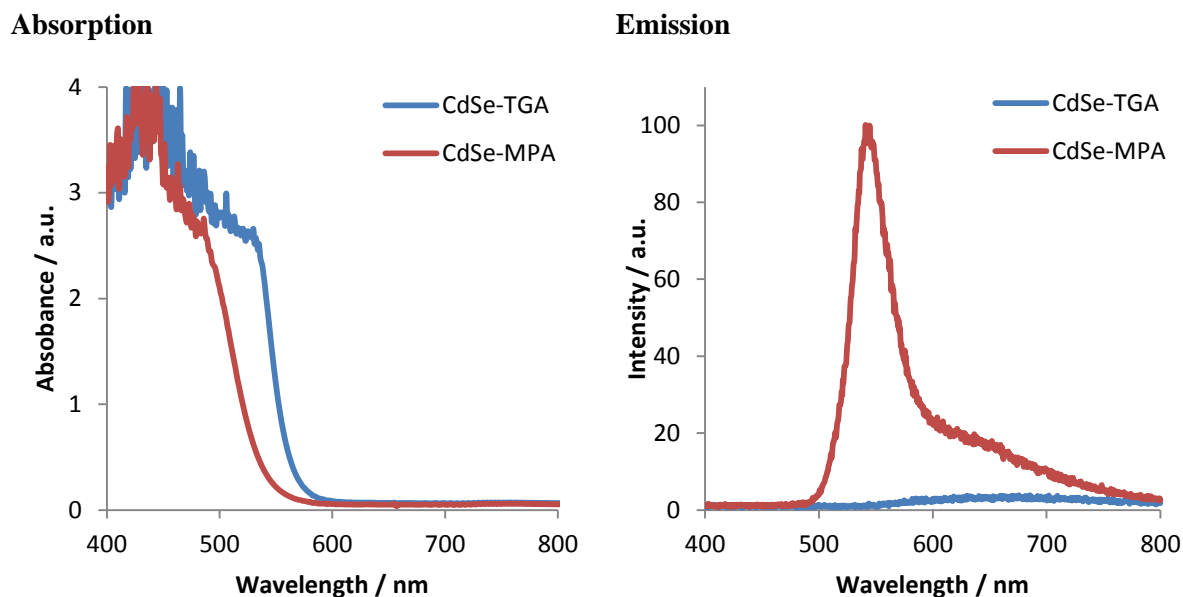


Figure 68: Absorption and emission spectra of CdSe quantum dots.

Furthermore, CdS quantum dots were synthesized via the previously described method (Figure 69). No precursor solution with NaBH_4 needed to be synthesized but Na_2S was dissolved and used directly for the synthesis. Again all reaction steps were carried out under argon atmosphere.

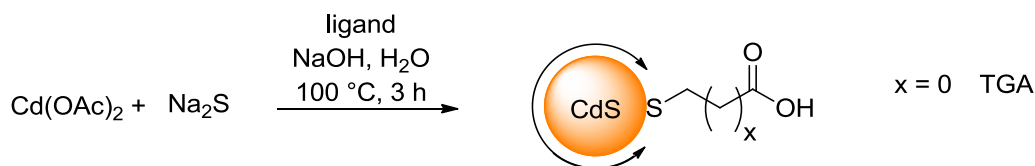


Figure 69: Reaction scheme for the synthesis of CdS quantum dots in aqueous solution.

Both spectra show absorption and emission properties of the colloidal solution indicating the formation of quantum dots (Figure 70), the intensities are however only weak. No further

characterizations of the solution or the nanoparticles were performed. Thus the synthetic parameters must be optimized for creation of CdS quantum dots via the approach in aqueous solution.

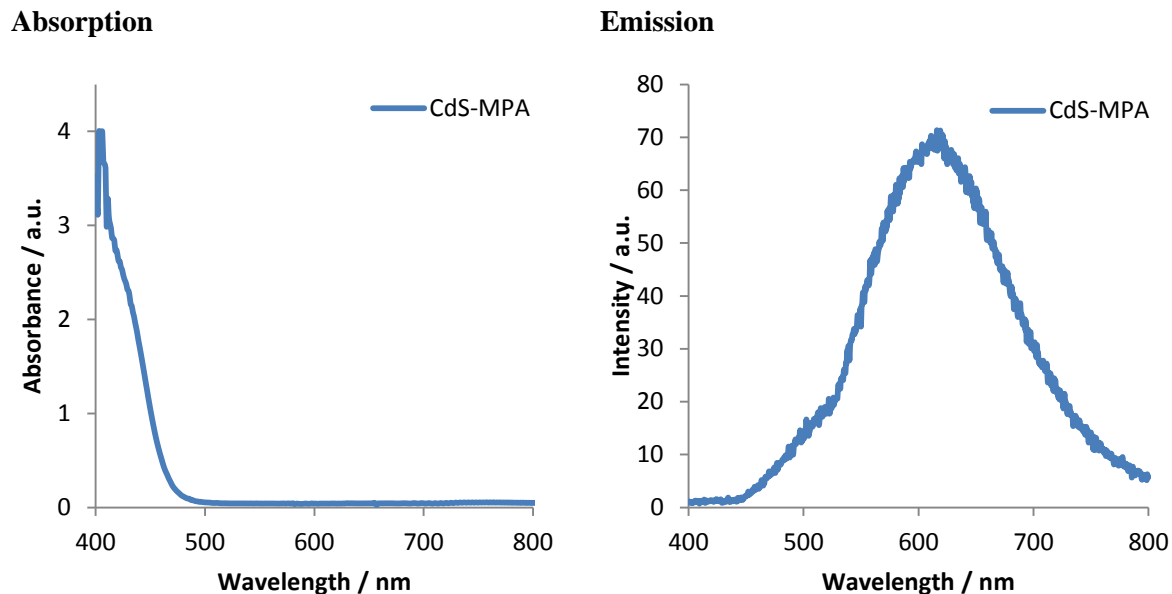


Figure 70: Absorption and emission spectra of CdS quantum dots.

Subsequently, CdTe quantum dots capped with TGA and MPA were covered with a ZnS-shell. This prevents the QDs from the leakage of cytotoxic Cd^{2+} ions, which is essential for biological applications. The passivation was done directly in solution. Precursor solutions of Zn^{2+} and S^{2-} were added and the reaction mixture was stirred at 60°C . Again dialysis was done for purification. From TEM images a mean thickness of 1 nm for the shell can be determined; EDX spot analysis confirmed the layer of ZnS around the quantum dot. The reaction time determines the thickness of the shell.

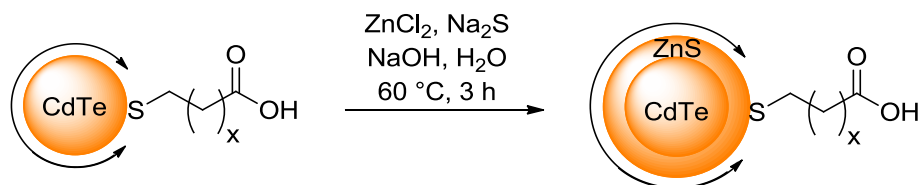


Figure 71: Reaction scheme for the passivation of CdTe quantum dots with a ZnS shell.

The QDs were characterized by TEM and DLS for the determination of the core size and with UV/Vis and fluorescence spectroscopy for the analysis of the optical properties.

For further biological application the optical properties of the synthesized ODs were examined and compared with each other. The properties of the core materials CdTe and CdSe with different ligands were used for comparison and the optical properties before and after passivation were compared.

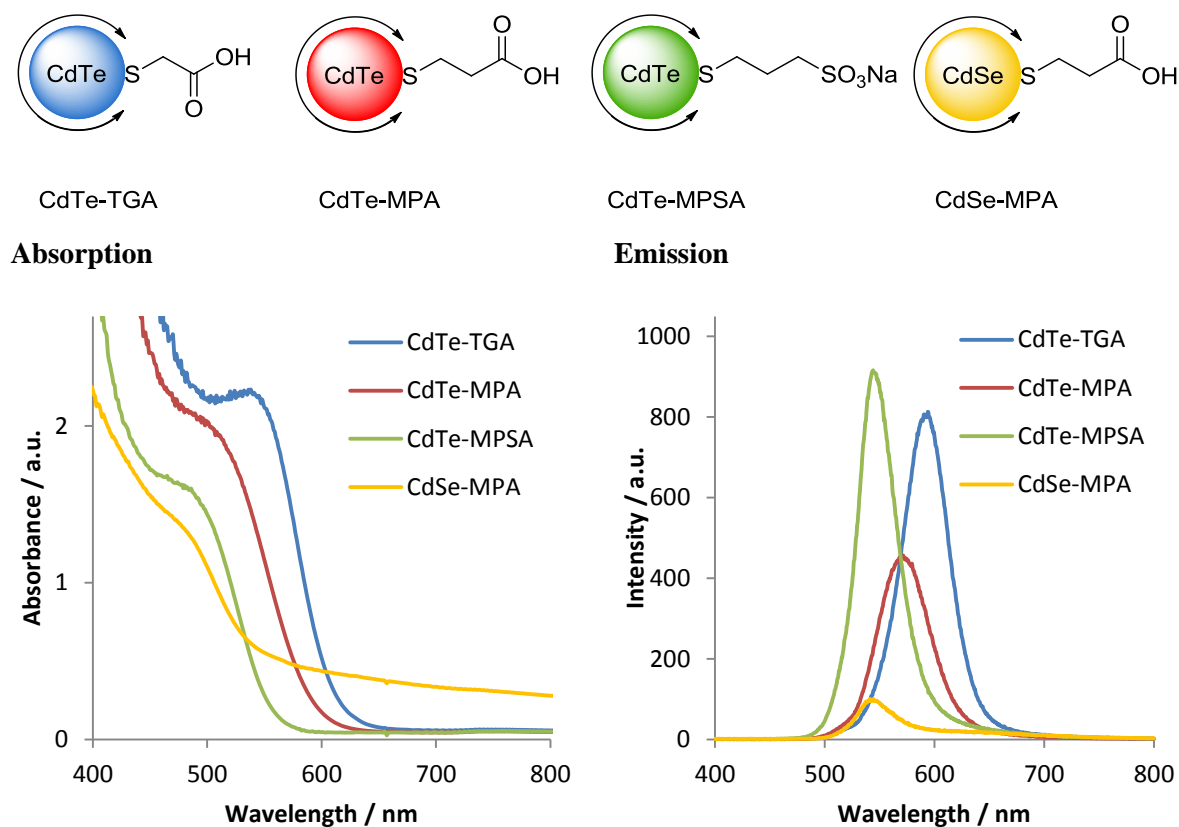


Figure 72: Summary of absorption and emission spectra of CdTe and CdSe quantum dots with different ligands.

The absorption and emission maxima of the QDs with different surface ligands differ as shown in Figure 72. CdTe-based QDs absorb light between 478 nm and 540 nm, the maximum of CdSe-based QDs lies at 473 nm. The emission maximum lies between 544 nm and 594 nm for CdTe QDs and for CdSe at 543 nm. The intensities are also different.

Additionally, passivated QDs were compared to their precursors. Comparing the absorption and emission spectra of both ZnS covered QDs and their unpassivated analogues, the growth and

thickness of the shell has no significant effect on the position of both absorption and emission maxima but on the intensities (Figure 73). The absorption abilities decrease and the emission abilities are higher for both TGA- and MPA-stabilized quantum dots. The spectra are plotted as measured and the concentrations of the sample are similar.

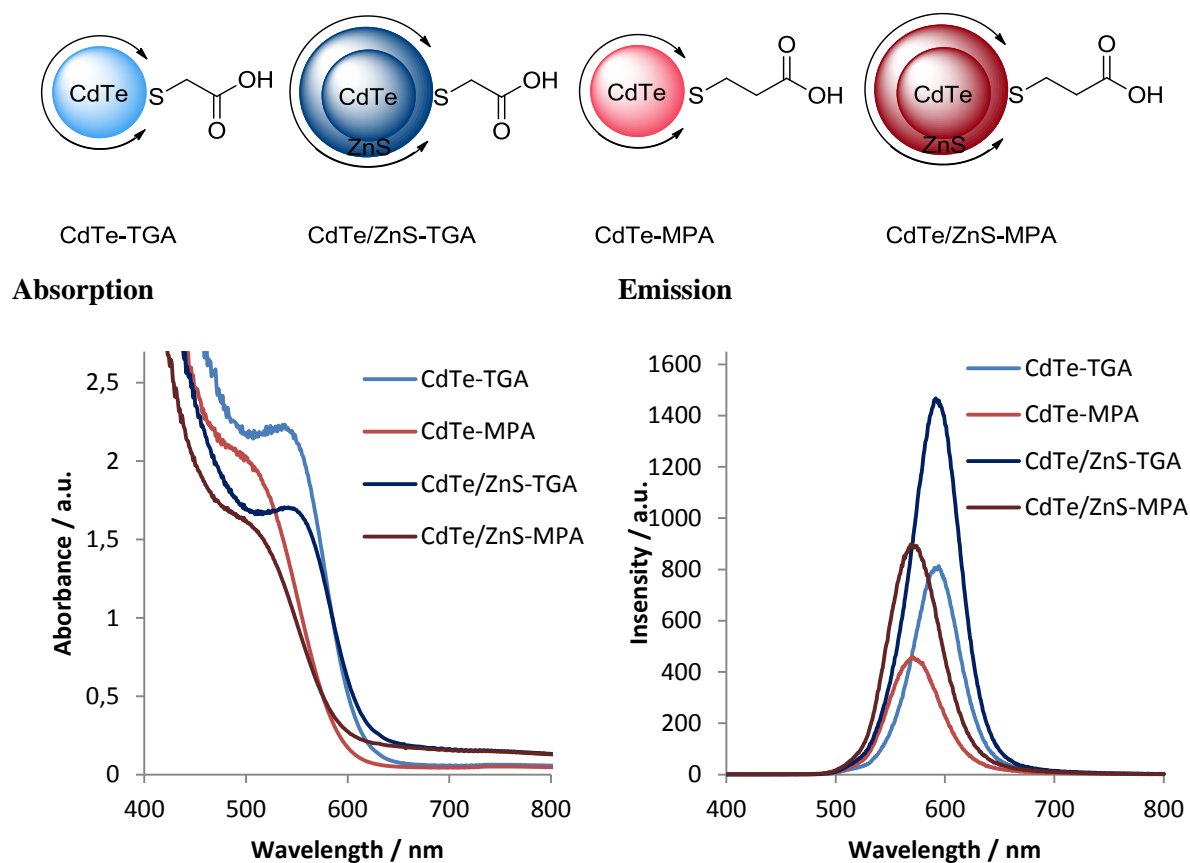


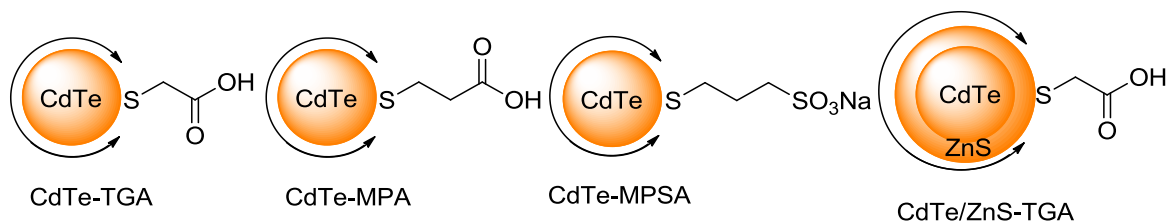
Figure 73: Summary of absorption and emission spectra of passivated CdTe quantum dots and their precursors.

The ZnS-shell is very thin and has only a slight influence on the optical properties. The maxima are shifted to a longer wavelength. Table 8 summarizes the values for absorption and emission maxima of the compared quantum dots. The corresponding diameters determined via TEM and DLS are also shown.

Table 8: Quantum dots stabilized with different ligands and the analogues passivated with a ZnS shell.

	d_{TEM}	d_{hydr}	λ_{abs}	λ_{em}
CdTe-TGA	4.1 ± 0.3 nm	8 ± 2 nm	540 nm	594 nm
CdTe-MPA	4.4 ± 0.4 nm	6 ± 1 nm	498 nm	574 nm
CdTe-MPSA	4.9 ± 0.4 nm	5 ± 1 nm	478 nm	544 nm
CdSe-MPA	3.9 ± 0.2 nm	5 ± 1 nm	473 nm	543 nm
CdTe/ZnS-TGA	4.2 ± 0.2 nm	11 ± 2 nm	542 nm	590 nm
CdTe/ZnS-MPA	4.5 ± 0.4 nm	6 ± 1 nm	500 nm	574 nm

CdTe quantum dots functionalized with three different ligands and the passivated CdTe/ZnS analogues were applied as new cell dyes (Figure 74). The effect of the ligand shell and core composition was investigated in cell uptake studies. Free carboxylic acid moieties were compared with sulfonated moieties and the effect of passivation was investigated. All quantum dots have almost the same diameter and were dispersed in basic solution, the concentration of the stock solution was 9 $\mu\text{mol/L}$. All QDs were stable in the buffer solution and could be used in biological media.

**Figure 74: Overview of CdTe quantum dots used for biological applications.**

The tests were done by Ervice Pouokam, research group Prof. Diener, Institute of Veterinary Physiology, Justus-Liebig University Giessen. The tested cells were rat colonic epithelial cells forming crypts. Mucosa-submucosa preparations obtained from rat colon were fixed on a plastic holder with tissue adhesive and incubated for about 7 min in an EDTA solution, then vibrated for about 30 s in order to obtain crypts. A stock solution of the QDs was diluted to 2.25 $\mu\text{mol/L}$. The QDs were collected in a high- K^+ gluconate Tyrode buffer and pipetted onto poly-L-lysine-coated cover glasses ($\varnothing = 23$ mm). The crypts were allowed to settle down at room temperature and attach onto the surface of the cover glasses for about 30 min. The cover glass was then mounted in a

chamber and the volume adjusted to 2 ml. After selecting at least nine regions of interest (ROIs; 3 in the depth of the crypt, 3 in the middle and 3 at the surface), corresponding each approximately to a cell, five excitation flashes were launched at 350 nm with the following durations: 5 ms, 10 ms, 20 ms, 50 ms and 100 ms. The resulting fluorescence was recorded live and the data stored. Then the stock solution of the QDs was added into the chamber to yield a final concentration of 2.25 $\mu\text{mol/L}$ without changing the volume. After an incubation period of 1 hour at room temperature, the chamber was rinsed twice with fresh Tyrode buffer to remove excess QDs and the same excitation protocol as before incubation was run. This allowed for tracking the changes of the fluorescence in the same ROIs.

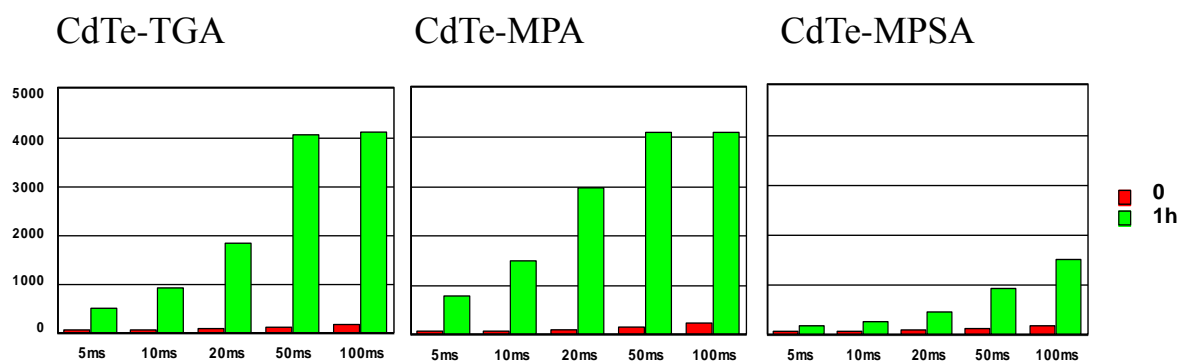


Figure 75: Crypts incubated with the QDs for 1 h in a Tyrode buffer solution; fluorescence intensity before and afterwards was compared. X-axis exposure time, Y-axis in arbitrary units.

All quantum dots tested showed a cell uptake after 1 hour incubation. TGA stabilized quantum dots also showed coloration of the background. This suggests unspecific interactions with biological tissues. The different core sizes seem not to effect the interactions. The experiments showed that QDs with a carboxylic acid terminated shell have a better cell uptake than their sulfonated analogues (Figure 75). The negative charge of the sulfonate group seems to restrain the quantum dots from entering the cells. Depending on the pH value of the cellular environment carboxylic acid moieties are both protonated and deprotonated. The reduced amount of effective charge seems to support the uptake.

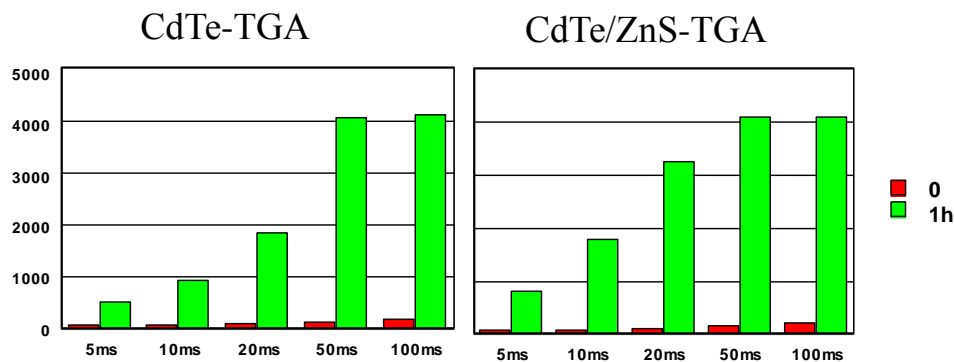


Figure 76: Crypts incubated with the QDs for 1 h in a Tyrode buffer solution; fluorescence intensity before and afterwards was compared. X-axis exposure time, Y-axis in arbitrary units.

The experiments showed that the passivated quantum dots had a faster uptake, but did not change significantly after time (Figure 76). Passivated QDs gave better results, which proves the shell prevents of Cd^{2+} leakage. CdTe/ZnS with thioglycolic acid at the surface gave best results in the cell uptake studies.

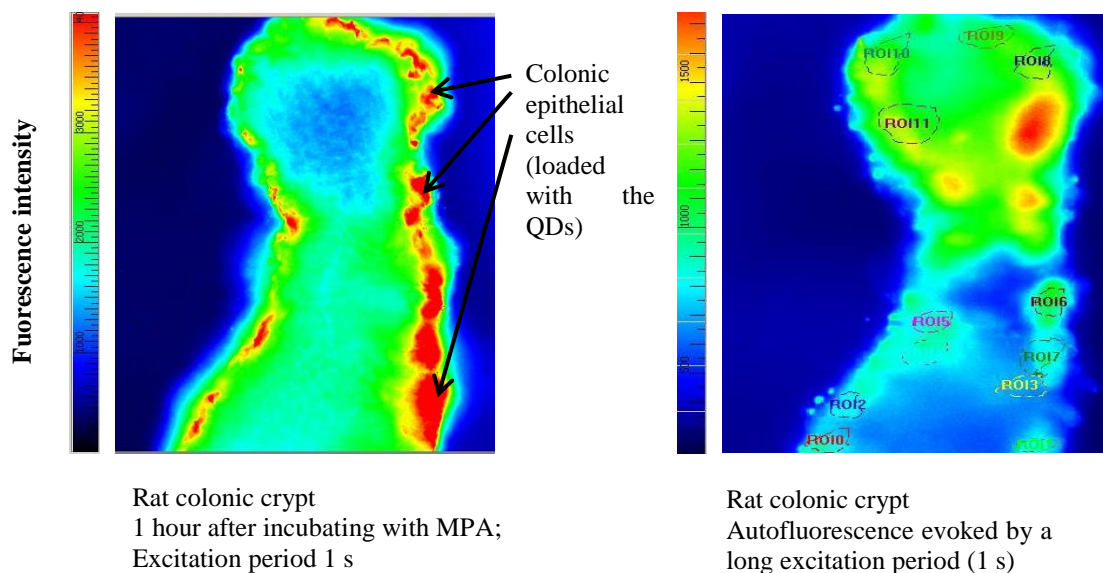


Figure 77: Crypts incubated with the QDs for 1 h in a buffer solution (tyrode).

Figure 77 shows an image of the cells incubated with quantum dots for one hour. It shows on the left hand an image of the cells incubated with quantum dots for one hour. Areas of high

fluorescence intensity are shown in red. Compared with the autofluorescence of the cells on the right hand, it appears that QDs have crossed the cell membrane and accumulated within the cells.

Further experiments must show where the quantum dots are located in the cell. Higher resolution of the images is needed to explain the mechanism behind this. The experiments show that mercaptocarboxylic acid terminated quantum dots are suitable for cell imaging but need to be passivated with a ZnS shell. These results also indicate that no further functionalization at the ligand periphery is needed for cell uptake. With specific epitopes however these quantum dots might be able to target cellular compartments. The synthesized quantum dots are equivalent to organic dyes for cellular imaging with several advantages: Within the choice of ligand, core material or core composition optical properties of the QDs can be tuned easily.

5.2 The Ternary System $\text{CdTe}_x\text{Se}_{1-x}$ -MPA

The ternary system of $\text{CdTe}_x\text{Se}_{1-x}$ was synthesized with different molar ratios of tellurium and selenium. For stabilization of the nanoparticles the short ligand MPA was chosen. The $\text{CdTe}_x\text{Se}_{1-x}$ quantum dots were prepared via the conventional synthesis in aqueous solution under inert conditions. The precursor solutions were prepared out of tellurium or selenium powder reduced in situ with NaBH_4 under inert conditions. Different molar ratios of NaHTe and NaHSe were added at the beginning, the reaction temperature and time were held constant at $100\text{ }^\circ\text{C}$ and 4 h, subsequently the resulting nanoparticles were purified via dialysis in water

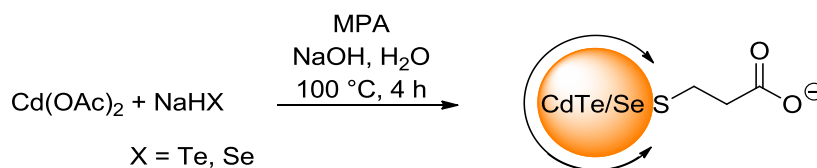


Figure 78: Synthetic procedure for the mixed crystal system $\text{CdTe}_x\text{Se}_{1-x}$.

The structural and optical properties of the resulting quantum dots were determined. Characterization was done by UV/Vis and emission spectroscopy, XRD analysis and EDX spot analysis. With an increasing percentage of telluride anions in the system the absorption maximum shifts to a higher and the emission maximum shifts to a lower wavelength (Figure 79). For CdSe -MPA QDs an absorption maximum of 485 nm and an emission maximum of 585 nm was observed,

and for CdTe-MPA 520 nm and 555 nm respectively. A linear correlation for the mixed analogues was found (Figure 79).

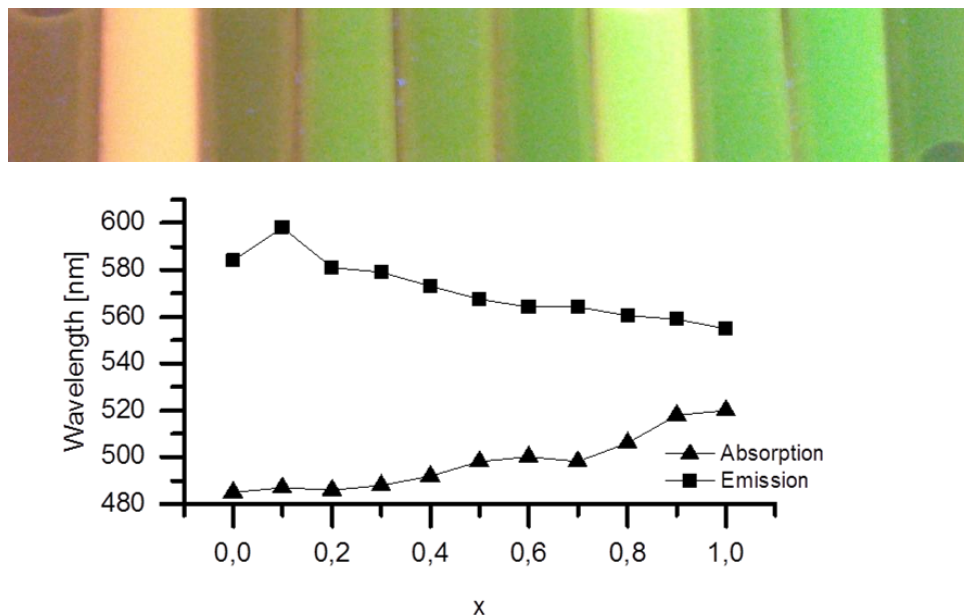


Figure 79: Emission ($\lambda_{\text{ex}} = 350$ nm) and absorption maxima of $\text{CdTe}_x\text{Se}_{1-x}$ -MPA with $x = 0.0$ to $x = 1.0$ Inset: Photography of $\text{CdTe}_x\text{Se}_{1-x}$ -MPA with $x = 0.1$ to $x = 1$ under the UV lamp ($\lambda_{\text{ex}} = 366$ nm).

XRD patterns of MPA-capped $\text{CdTe}_x\text{Se}_{1-x}$ show that the reflections shift linearly between those of the binary compounds of CdTe and CdSe according to Vegard's law (Figure 80). This indicates a solid solution meaning both compounds form a mixed crystal system without miscibility gap. This is possible due to the fact that both CdTe and CdSe have a cubic crystal structure with tellurium and selenium atoms statistically occupying the anion sub lattice. The reflections in the XRD patterns are broadened due to nanostructuring. A mean diameter of 3 nm can be calculated using the Scherrer equation. [162]

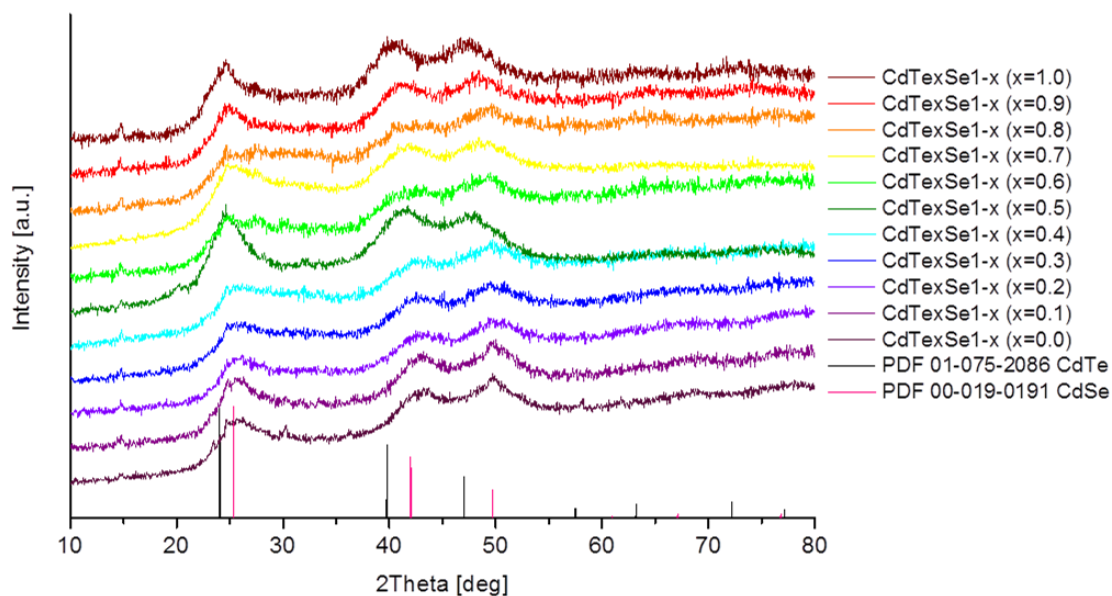


Figure 80: XRD patterns of CdTe_xSe_{1-x}-MPA with $x = 0.0$ to $x = 1$. Both binary compounds CdTe and CdSe are also shown for comparison with the mixed crystal system.

TEM measurements show monodisperse nanoparticles with a mean diameter between 2.3 nm and 2.9 nm and nearly monodisperse. Thus, the growth mechanism for the quantum dots does not depend on the precursor solution. EDX spot analysis revealed a homogeneous distribution of the constituting elements within the particles. The values found correspond to the nominal composition of the mixed crystals (Table 9).

Table 9: Overview CdTe_xSe_{1-x}-MPA quantum dots: diameter, composition, absorption and emission maxima.

x	d _{TEM}	EDX Te/Se	λ_{abs}	λ_{em}
0	2.6 ± 0.2 nm	0.00/1.00	485 nm	584 nm
0.1	2.4 ± 0.3 nm	0.13/0.87	487 nm	598 nm
0.2	2.9 ± 0.2 nm	0.24/0.76	486 nm	581 nm
0.3	2.3 ± 0.3 nm	0.30/0.70	488 nm	579 nm
0.4	2.5 ± 0.2 nm	0.38/0.62	492 nm	573 nm
0.5	2.6 ± 0.2 nm	0.61/0.39	498 nm	567.5 nm
0.6	2.5 ± 0.3 nm	0.68/0.32	500 nm	564 nm
0.7	2.3 ± 0.3 nm	0.68/0.32	498 nm	564 nm
0.8	2.5 ± 0.2 nm	0.60/0.40	506 nm	560.5 nm
0.9	2.5 ± 0.2 nm	0.88/0.12	518 nm	559 nm
1.0	2.6 ± 0.2 nm	1.00/0.00	520 nm	555 nm

Because of their already given water solubility and stability, these quantum dots are versatile tools for biological applications such as cell imaging. They can also be functionalized with bioactive substances via peptide coupling at the carboxylic acid.

Within this work different methods for the tuning of optical properties of quantum dots were presented. On the one hand different ligands used in the synthesis can result in different QDs. On the other hand different core materials can be used. Synthesis of mixed crystal systems can combine elements and shift the absorption and emission maxima between both compounds.

Another aspect responsible for optical properties is the crystallinity of the inorganic core. Experiments showed that with higher crystallinity the maxima are shifted to longer wavelengths. This can be achieved by the use of microwave irradiation, high temperatures and high pressures.

6. Summary/Zusammenfassung

6.1 Summary

In conclusion this work presents a successful application of newly developed conjugates of bioactive molecule and nanoparticle. A remarkable enhancement of receptor activation was achieved by multivalent presentation of active moieties supported on gold nanoparticles.

For this purpose diverse gold nanoparticles were synthesized and functionalized with biogenic amines. Different synthetic approaches were used to obtain gold nanoparticles between 4 nm and 25 nm. Small gold nanoparticles of 4 nm, 6 nm and 7 nm were synthesized in organic solution; larger gold nanoparticles of 14 nm and 25 nm were synthesized by citrate reduction of the precursor salt in aqueous solution. All types were rather monodisperse in size. Next they were equipped with mercaptocarboxylic acids of different chain lengths via ligand exchange reaction making all gold nanoparticles water soluble. This kind of ligand provides an additional group for functionalization at the ligand periphery. Only with 11-mercaptoundecanoic acid (MUDA) was the resulting colloidal solution stable and could be used for further modifications. Molecules possessing an amino group can be coupled onto the gold nanoparticles via EDC/NHS (1-ethyl-3-(3-dimethylaminopropyl)carbodiimide/*N*-hydroxysuccinimide) mediated peptide coupling reaction. Four different amines were immobilized on gold nanoparticles of 14 nm diameter: histamine (Au-MUDA-HA), dopamine (Au-MUDA-DA), serotonin (Au-MUDA-5HT) and carbachol (Au-MUDA-CB).

Histamine functionalized 14 nm gold nanoparticles were applied as new agonists in ligand-receptor interaction (Figure 81). As a functional read-out system, chloride secretion resulting from stimulation of neuronal and epithelial histamine H₁ and H₂ receptors was measured in *Ussing* chamber experiments. Compared to native histamine the multivalent presentation of histamine resulted in a potentiation of activation ability. Extremely low concentrations were necessary to induce a chloride secretion across rat colonic epithelium. For comparison the monovalent analogue AcS-MUDA-HA and gold nanoparticles without an active moiety Au-MUDOLS were also synthesized and tested. The measured effects could be attributed to Au-MUDA-HA as both references showed no activity at low concentrations. Only Au-MUDOLS harmed the tissue irreversibly. The observed effects could be explained by a high local density of histaminic moieties

in close proximity. Tests with 7 nm and 25 nm gold nanoparticles did not show consistent results in the experimental setup and no statement of size dependence can be made.

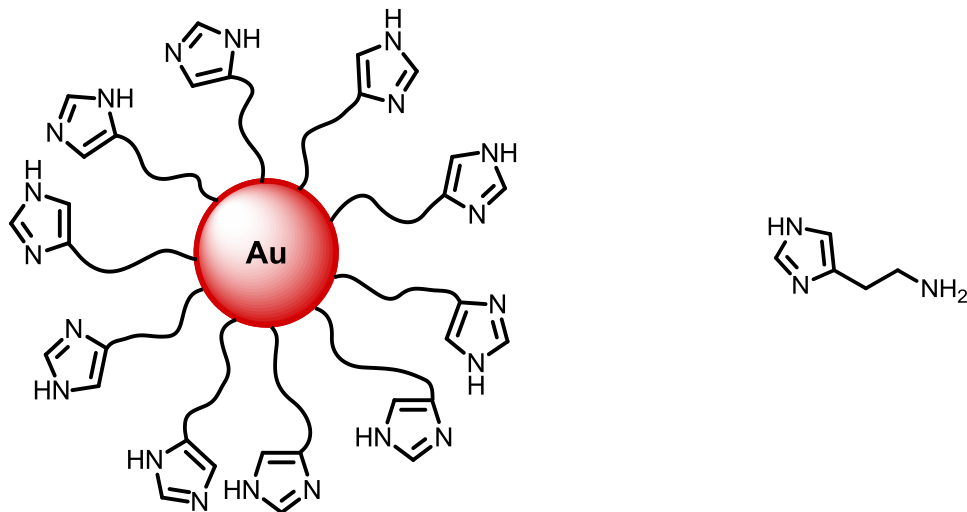


Figure 81: Histamine functionalized gold nanoparticles and native histamine.

Dopamine functionalized gold nanoparticles Au-MUDA-DA were not able to induce a chloride secretion at the administered concentrations. The colloidal solution changed color indicating an alteration. However multivalent presentation of serotonin on the gold nanoparticles Au-MUDA-5HT was effective. Chloride secretion could be measured in *Ussing* chamber experiments. Again very low concentrations were needed for activation of receptors. The stable acetylcholine derivative carbachol immobilized at the gold nanoparticles Au-MUDA-CB also showed excellent results in *Ussing* chamber experiments. Au-MUDA-CB evoked a response at picomolar concentrations. Gold nanoparticles with only free carboxylate moieties Au-MUDA were not inert in the experimental setup and they were able to activate receptors unspecifically. Again all enhanced interactions can be referred to the multivalent supporting of the active moieties.

In a further part of this work quantum dots (QDs) for cellular imaging were synthesized. CdTe and CdSe based nanoparticles emit in the visible spectrum of light when their core size is smaller than the Exciton bohr radius. QDs were synthesized directly in aqueous solution using different mercaptocarboxylic acids as capping ligands. The optical properties were determined. For biological application the QDs were covered with a ZnS shell. The presence of the additional shell has only slight influence on the optical properties of the QDs. Both passivated and unpassivated nanoparticles were applied for cell imaging. Carboxylic acid terminated QDs showed a better cell

uptake than the sulfonated analogue, passivated QDs showed a faster cell uptake. CdTe/ZnS-TGA (thioglycolic acid) showed the best results in the cell imaging study.

Additionally the ternary system consisting of both parts of CdTe and CdSe was synthesized and characterized. Optical properties of the mixed crystal system shift linearly between both binary compounds. The size of the QDs did not differ significantly. This synthetic method can be used for fine tuning of emitting-properties without changing the particle size, which is necessary in some biological applications.

6.2 Zusammenfassung

In dieser Arbeit wurde eine erfolgreiche Anwendung von neu entwickelten Konjugaten aus bioaktivem Molekül und Nanopartikel vorgestellt. Es konnte eine erhebliche Verbesserung in der Rezeptoraktivierung durch multivalente Präsentation von aktiven Substanzen auf Goldnanopartikeln erzielt werden.

Hierzu wurden diverse Goldnanopartikel synthetisiert und funktionalisiert. Verschiedene synthetische Ansätze wurden ausgewählt, um Goldnanopartikel zwischen 4 nm und 25 nm zu erhalten. Kleine Goldnanopartikel mit 4 nm, 6 nm und 7 nm Größe wurden in organischer Lösung hergestellt, größere Goldnanopartikel mit 14 nm und 25 nm Größe wurden mittels Citrat-Reduktion eines Goldsalzes synthetisiert. Alle dargestellten Partikel waren relativ monodispers in ihrer Form. Anschließend wurden Mercaptocarbonsäuren verschiedener Kettenlängen mittels Ligandenaustauschreaktion auf die Partikel gebracht, wodurch auch die Partikel aus der organischen Synthese wasserlöslich wurden. Diese Art Liganden beinhaltet eine zusätzliche funktionelle Gruppe zur Funktionalisierung an der Ligandenperipherie. Nur mit 11-Mercaptoundecansäure (MUDA) konnten stabile kolloidale Lösungen erhalten werden, die für weitere Modifikationen genutzt werden können. Moleküle mit einer Aminogruppe können über EDC/NHS (1-Ethyl-3-(3-dimethylaminopropyl)carbodiimide/*N*-Hydroxysuccinimide) vermittelte Peptidkupplung auf den Goldnanopartikeln angebracht werden. Vier verschiedene Amine wurden auf Goldnanopartikel mit 14 nm Durchmesser immobilisiert: Histamin (Au-MUDA-HA), Dopamin (Au-MUDA-DA), Serotonin (Au-MUDA-5HT) und Carbachol (Au-MUDA-CB).

Histamin-funktionalisierte Goldnanopartikel mit 14 nm Größe wurden als neue Agonisten in der Ligand-Rezeptor-Wechselwirkung (Abbildung 81) angewendet. Gemessen wurde die Chlorid-Sekretion durch die Stimulierung von neuronalen und epithelialen Histamin H₁ und H₂ Rezeptoren

in *Ussing*-Kammer-Experimenten gemessen. Im Vergleich zu nativem Histamin führte die multivalente Präsentation von Histamin zu einer Potenzierung der Aktivierungsfähigkeit. Es waren extrem niedrigen Konzentrationen notwendig, um eine Chlorid-Sekretion am Ratten Kolonepithel zu induzieren. Zum Vergleich wurden auch das monovalente Analogon AcS-MUDA-HA und Goldnanopartikel ohne eine aktive Einheit Au-MUDOLS synthetisiert und getestet. Die gemessenen Effekte konnten so Au-MUDA-HA zugeschrieben werden, da beide Referenzen keine Aktivität bei geringen Konzentrationen zeigten. Nur Au-MUDOLS zerstörte das Gewebe irreversibel. Die beobachteten Effekte können durch eine hohe lokale Dichte von Histamin-Einheiten in unmittelbarer Nähe erklärt werden. Die ebenfalls getesteten Goldnanopartikel mit 7 nm und 25 nm Größe zeigten keine konsistenten Ergebnisse und es kann keine Aussage über die Größenabhängigkeit gemacht werden.

Dopamin-funktionalisierte Goldnanopartikel Au-MUDA-DA waren nicht in der Lage, ein Chlorid-Sekretion bei den verabreichten Konzentrationen zu induzieren. Die Farbänderung der kolloidalen Lösung deutet darauf hin, dass eine Veränderung der Struktur stattgefunden hat. Allerdings zeigte die multivalente Präsentation von Serotonin auf den Goldnanopartikeln Au-MUDA-5HT eine Wirkung. Eine Chlorid-Sekretion konnte in den *Ussing*-Kammer-Experimenten gemessen werden. Auch hier wurden sehr geringe Konzentrationen für die Aktivierung der Rezeptoren benötigt. Das stabile Acetylcholin-Derivat Carbachol immobilisiert auf Goldnanopartikeln Au-MUDA-CB zeigte auch hervorragende Ergebnisse in den *Ussing*-Kammer-Experimenten. Au-MUDA-CB zeigte eine Antwort im pikomolaren Bereich auf. Goldnanopartikel mit nur freien Carboxylat-Einheiten Au-MUDA waren nicht inert; sie waren in der Lage, Rezeptoren unspezifisch zu aktivieren. Alle gemessenen Effekte können der multivalenten Präsentation der aktiven Einheiten zugeschrieben werden.

Im anderen Teil dieser Arbeit wurden Quantenpunkte (QDs) für zelluläre Bildgebung synthetisiert. CdTe- und CdSe- basierte Nanopartikel emittieren im sichtbaren Bereich des Lichtes, wenn ihre Kerngröße kleiner als der Exciton-Bohr-Radius ist. QDs wurden direkt in wässriger Lösung unter Verwendung verschiedener Mercaptocarbonsäuren als Capping-Liganden synthetisiert. Die optischen Eigenschaften wurden bestimmt. Für die biologischen Anwendungen wurden die QDs mit einer ZnS-Schale ummantelt. Das Vorhandensein der zusätzlichen Hülle hat nur geringen Einfluss auf die optischen Eigenschaften der Quantenpunkte. Beide passivierten und nicht passivierten Nanopartikel wurden zur zellulären Bildgebung angewendet. Carbonsäuren terminierte QDs zeigten eine bessere Zellaufnahme als die sulfonierten Analogen, passivierte QDs zeigten eine schnellere Zellaufnahme. CdTe/ZnS-TGA (Thioglycolsäure) wiesen die besten Ergebnisse in der Studie auf.

Zusätzlich wurde das ternäre System, bestehend aus $\text{CdTe}_x\text{Se}_{1-x}$, synthetisiert und charakterisiert. Die optischen Eigenschaften des Mischkristallsystems liegen zwischen den beiden binären Verbindungen und korrelieren linear mit der Zusammensetzung. In der Größe der QDs lag keine signifikante Abweichung. Diese Synthesemethode kann für die Feinabstimmung der Emissions-Eigenschaften genutzt werden, ohne dass die Partikelgröße dabei verändert wird, was in einigen biologischen Anwendungen notwendig ist.

7. Outlook

After the successful immobilization of the four neurotransmitters and the ability of these conjugates to activate receptors, further experiments will be done to explain these multivalent interactions as there is little research in this field of interest. Histamine functionalized gold nanoparticles with a diameter of 14 nm were proved to act as their monovalent analogues and were excellent activators for receptor functionality. Another attempt can be made on the synthesis of dopamine functionalized gold nanoparticles. These conjugates have versatile applications. Because of the basic pH value, the catechol moiety oxidized *in situ*, reaction conditions and synthetic strategy must be optimized. The multivalent presentation of carbachol on 14 nm gold nanoparticles also showed encouraging first results. The effect of those conjugates on the cholinergic systems should be studied in depth.

Investigations ought to be done on the reactivity of receptor blockers immobilized on gold nanoparticles. It can be presumed that the activation concentration of multivalently presented blockers is also lower than that of the molecular agents. The use of receptor blockers is far more widespread and applied in therapy. Atropine is an interesting representative of receptor blockers. It addresses muscarinic receptors and is an anticholinergic blocking the effect of acetylcholine in the body. Immobilization cannot be accomplished as before, the molecule first has to be modified and provided with a linker anchoring at the gold surface.

Moreover the size dependence of the effects should be investigated in detail. A variety of nanoparticles with different core sizes but the same ligands at the surface can be compared in their activating ability. The core materials can also be exchanged for cheaper materials or materials with additional properties and used for biological tests. Iron oxide based nanoparticles can also be synthesized relatively easily in different core sizes from affordable precursors and their biocompatibility is also very high. Furthermore they inherit the property of superparamagnetism. A direct synthesis in aqueous solution yielding monodisperse nanoparticles could be developed.

Another closer look ought to be taken at the molecular interactions at the interface between nanoparticle and receptor. The multivalent interactions contributing to the huge potency of the conjugates can be determined in detail helping to understand the mechanisms. Sophisticated cell analysis can be used to gain insight in subcellular structures and reactions. This might help to develop new nanomaterials for therapy. For this purpose the nanoparticles can be equipped with a

fluorescent dye. With the help of fluorescence microscopy the location of the nanoparticles in the tissue can be visualized. It should also be examined whether the gold nanoparticles are able to overcome barriers like cell walls. The surface can be covered with ligands favoring a cross over membranes. If this is successful it might be possible to set a controlled transport across the barrier. Here again a size dependency should be investigated. Functionalized quantum dots can also be applied for cell imaging to give information about the remains of the nanoparticulate materials.

Besides all these applications also the toxicity of the nanoparticles should be kept in mind. Size and ligand dependent cytotoxicity can often be observed for nanoparticles in biological systems. Especially the gold core and the time in the body after the reaction should be investigated in detail. Biocompatibility of the nanoparticles is crucial for further applications.

Multivalent presentation of active substances proved to enhance the interactions and gives promising outlook. Systematic investigations and the synthesis of novel conjugates will open the door to new developments in nanomedicine and nanomaterial based applications.

8. Experimental Section

8.1 Chemicals, Solvents and Consumables

All chemicals were purchased from Acros Organics, Alfa Aesar, Sigma Aldrich, Merck, Novabiochem or Fluka at the highest purity grade available, solvents were purchased anhydrous and with 99.9% purity unless otherwise noted. All solvents were distilled prior to use. All reactions under inert conditions were carried out in argon atmosphere (99.99%, Messer Griesheim) employing oven- and flame-dried glassware.

Dry DMF was prepared as followed: DMF was refluxed under argon with sodium and benzophenone for several hours until the solution turned blue. Anhydrous DMF was stored over molecular sieve 4 Å under argon.

For the synthesis of nanoparticles ultrapure water from Millipore was used.

For dialysis of the particle solution a membrane of regenerated cellulose with different pore size by Roth was used. The membrane was treated according to the producer which means soaking for 30 min in distilled water followed by washing. All dialyses were prepared at room temperature in the given solvent for a given time.

Flash column chromatography and filtration was performed using Merck silica gel 60 Å (0.040 – 0.063 mm mesh size). Analytical thin-layer chromatography (TLC) was performed using pre-coated polyester sheets Polygram® SIL G/UV254 Machery-Nagel, 0.2 mm silica gel with fluorescent indicator.

8.2 Analytics

NMR Analysis:

^1H and ^{13}C NMR spectra were recorded on Bruker BioSpin Avance III AV600 (600 MHz), AV400 (400 MHz) or AV200 (200 MHz) spectrometers using TMS as an internal standard with chemical shifts given in ppm relative to TMS ($\delta = 0.00$ ppm) or the respective solvent peaks. ^1H NMR data

are reported as follows: chemical shifts (multiplicity [ppm], coupling constants [Hz], integration, classification). Multiplicity is recorded as s = singlet, br s = broadened singlet, d = doublet, t = triplet, q quartet, m = multiplet. For ^{13}C NMR, chemical shifts and structural assignments are reported where applicable.

IR:

The IR measurements were performed on a Bruker Alpha IR spectrometer utilizing KBr cells ($d = 0.5\text{ mm}$).

UV/Vis:

The UV/Vis spectra were recorded with an Agilent 8453 spectrophotometer (Agilent Technologies Inc., Santa Clara, CA, USA).

CHN-Analysis:

Elemental analyses were obtained with a Carlo Erba 1106 (balance: Mettler Toledo UMX-2) analyzer.

ESI:

Mass spectra were recorded on a Finnigan LCQDuo spectrometer using methanol solutions of the respective compounds.

TEM:

The characterization of the particle cores was accomplished by a transmission electron microscope CM30/STEM by Philips with a LaB_6 cathode, 300 kV equipped with a GATAN digital camera. 10 μL of the colloidal solution was placed on a carbon-coated copper grid, followed by natural evaporation of the solvent at room temperature. For determination of the size and standard deviation 100 particles were measured.

DLS and ζ -potential:

The hydrodynamic radius in solution was determined by a STABISIZER PMX-200 from Particle Metrix GmbH via dynamic light scattering setting set zero 20 s, 3 x 180 s per run, 3 runs. Zeta-potentials were measured on a NanoZS by Malvern.

XRD:

The crystal structure of the nanoparticles was verified by powder X-ray diffraction in reflection mode on a PANalytical X'Pert PRO instrument with Cu K $_{\alpha}$ radiation ($\lambda = 1.54 \text{ \AA}$) at an operating voltage of 40 kV and a current of 40 mA (divergence aperture 2°).

Crystallite size was calculated with Scherrer equation (d = crystallite size, k = shape factor 0.9, λ = irradiation wavelength, $\beta_{1/2}$ = reflection width at half height, θ = diffraction angle).

$$d = \frac{k \cdot \lambda}{\beta_{1/2} \cdot \cos \theta}$$

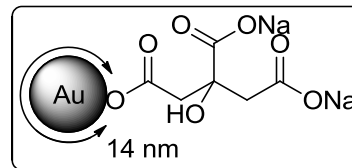
TGA:

Thermogravimetric measurements were done with a Netzsch STA409PC thermoscale with an attached quadrupole mass spectrometer QMG421 by Balzers, ionization energy 70 eV.

8.3 Synthesis of the Nanoparticles

Citrate-coordinated gold nanoparticles (Au-Citrate Ø 14 nm)

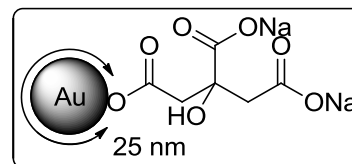
A solution of 50 mg (0.127 mmol) $\text{HAuCl}_4 \cdot 3 \text{H}_2\text{O}$ in 195 mL of Millipore water was heated to reflux for 20 min. Under vigorous stirring a solution of 224 mg (0.52 mmol) of sodium citrate in 5 mL of Millipore water was added quickly. The reaction mixture was held at 80 °C for 2 h. Then the solution was cooled to 0 °C in an ice bath and filtered (0.2 μm pore size). A clear red solution with a particle concentration of 2.7 nM was obtained and stored at 4 °C.



^1H NMR (400 MHz, D_2O): δ/ppm = 2.61 (bs, CH_2); **IR** (KBr disc): ν/cm^{-1} = 3426.8 ($\nu_{\text{O-H}}$), 1598.2 ($\nu_{\text{C=O}}$), 1397.6, 1258.4, 618.0; **TEM**: $d = 14.0 \pm 0.9 \text{ nm}$; **UV/Vis**: $\lambda_{\text{max}} = 522 \text{ nm}$; **DLS**: $d_{\text{hydr}} = 17 \pm 3 \text{ nm}$.

Citrate-coordinated gold nanoparticles (Au-Citrate Ø 25 nm)

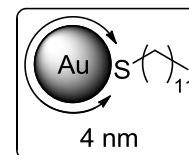
A solution of 2.5 mg (0.018 mmol) $\text{HAuCl}_4 \cdot 3 \text{H}_2\text{O}$ in 72 mL of Millipore water was heated to reflux for 10 min. Under vigorous stirring a solution of 9 mg (0.03 mmol) of sodium citrate in 0.9 mL of Millipore water was added quickly. The reaction mixture was held at 80 °C for 30 min. The solution turned first blue then purple. Subsequently the solution was cooled to 0 °C in an ice bath and filtered (0.2 μm pore size). A clear red solution with a particle concentration of 0.5 nM was obtained and stored at 4 °C.



^1H NMR (400 MHz, D_2O): δ/ppm = 3.12 (bs, OH), 2.75 (d, $J = 15.4 \text{ Hz}$, 2 H, CH_2), 2.64 (d, $J = 15.4 \text{ Hz}$, 2 H, CH_2); **IR** (KBr disc): ν/cm^{-1} = 3426.8 ($\nu_{\text{O-H}}$), 1598.2 ($\nu_{\text{C=O}}$), 1397.6, 1258.4, 618.0; **TEM**: $d = 25.3 \pm 2.4 \text{ nm}$; **UV/Vis**: $\lambda_{\text{max}} = 529 \text{ nm}$; **DLS**: $d_{\text{hydr}} = 26 \pm 10 \text{ nm}$.

DT-coordinated gold nanoparticles (Au-DT Ø 4 nm)

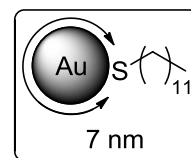
62 mg AuPPh_3Cl (0.125 mmol) were mixed with 0.06 mL 1-dodecanethiol (0.25 mmol, 2 equiv.) in 10 mL chloroform to form a clear solution. An amount of 108 mg (1.25 mmol, 10 equiv.) of *tert*-butylamin-borane complex was added and the solution turned dark red. The mixture was heated with stirring at 65 °C for 5 h and then cooled down to room



temperature. Then 40 mL of ethanol were added and the precipitate separated by centrifugation. The black powder was washed with ethanol three times, dried under vacuum. The gold nanoparticles were resolved in 10 mL of chloroform to give a dark red solution with a particle concentration of 6.3 μM .

^1H NMR (400 MHz, CDCl_3): δ/ppm = 1.59-1.52 (m, 6 H, CH_2), 1.43-1.39 (m, 2 H, CH_2), 1.30-1.22 (m, 10 H, CH_2), 1.13-1.09 (m, 4 H, CH_2), 0.88 (t, J = 6.9 Hz, 3 H, CH_3); **IR** (KBr disc): ν/cm^{-1} = 2921.8 (s, $\nu_{\text{C-H}}$), 2850.9 (s, $\nu_{\text{C-H}}$), 1488.0, 1385.6, 948.3; **TEM**: $d = 4.0 \pm 1.0$ nm; **UV/Vis**: $\lambda_{\text{max}} = 507$ nm, **DLS**: $d_{\text{hydr}} = 5 \pm 1$ nm.

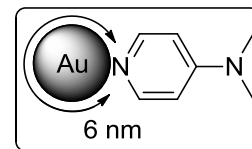
DT-coordinated gold nanoparticles (Au-DT \varnothing 7 nm)



247 mg AuPPh_3Cl (0.5 mmol) were mixed with 0.25 mL 1-dodecanethiol (1 mmol, 2 equiv.) in 40 mL toluene to form a clear solution. An amount of 435 mg (5 mmol, 10 equiv.) of *tert*-butylamin-borane complex was added and the solution turned dark red. The mixture was heated with stirring at 55 $^\circ\text{C}$ for one hour and then cooled down to room temperature. Then 40 mL of ethanol were added and the precipitate separated by centrifugation. The black powder was washed with ethanol three times, dried under vacuum. The gold nanoparticles were resolved in 10 mL of chloroform to give a dark red solution with a particle concentration of 7.5 μM . The use of benzene instead of toluene results in gold nanoparticles with a mean diameter of 6 nm.

^1H NMR (400 MHz, CDCl_3): δ/ppm = 1.60-1.49 (m, 10 H, CH_2), 1.33-1.19 (m, 12 H, CH_2), 0.88 (t, J = 7.2 Hz, 3 H, CH_3); **IR** (KBr disc): ν/cm^{-1} = 2917.1 (s, $\nu_{\text{C-H}}$), 2844.2 (s, $\nu_{\text{C-H}}$), 1454.8, 1432.8, 716.1, 687.7, 517.7; **TEM**: $d = 7.1 \pm 0.8$ nm; **UV/Vis**: $\lambda_{\text{max}} = 518$ nm; **DLS**: $d_{\text{hydr}} = 8 \pm 1$ nm.

DMAP-coordinated gold nanoparticles (Au-DMAP \varnothing 6 nm)

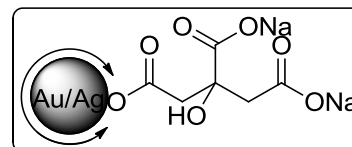


An aqueous solution of HAuCl_4 (24 mg in 2 mL) was added to a solution of tetraoctylammonium bromide (TOAB) in toluene (153 mg in 5 mL) and the mixture was stirred until all the tetrachloroaurate had transferred into the organic phase, to give a deep orange solution. A fresh solution of NaBH_4 (27 mg in 1.5 mL) was added slowly whilst stirring. The toluene phase immediately turned to ruby red. After stirring for 18 hours, the toluene phase containing TOAB-stabilized gold NPs was washed with 0.1 M H_2SO_4 , 0.1 M NaOH and H_2O (each three times). Subsequently, an aqueous solution of DMAP (300 mg in 24 mL) was added to the TOAB-stabilized gold NP solution. Phase transfer of the solution took place simultaneously and a ruby red aqueous

solution of DMAP-Au NPs was isolated. Purification was done with dialysis against water (three times for three hours). The stock solution was stored at 4 °C.

¹H NMR (400 MHz, CDCl₃): 7.86 (d, J = 6.9 Hz, 2 H, CH), 6.40 (d, J = 6.9 Hz, 2 H, CH), 2.76 (s, 3 H, CH₃); **TEM**: d = 8.6 ± 2.9 nm; **UV/Vis**: λ_{max} = 522 nm; **DLS**: d_{hydr} = 30 ± 3 nm.

Alloyed gold/silver nanoparticles (Au/Ag-Citrate):



An amount of HAuCl₄ was dissolved in 150 mL of Millipore water and heated to reflux. The respective amount of AgNO₃ was added under vigorous stirring immediately followed by the amount of sodium citrate. The temperature of the reaction mixture was lowered to 80 °C and stirred for 2 h. Subsequently the solution was cooled to 0 °C in an ice bath and filtered (0.2 μm pore size). A clear solution was obtained. The nanoparticles were characterized with TEM and UV/Vis spectroscopy.

	m _{HAuCl4}	n _{HAuCl4}	m _{AgNO3}	n _{AgNO3}	m _{Na3Cit}	d _{TEM}	λ _{abs}
Au	14.18 mg	36 μmol	-	-	78.15 mg	14.0 ± 0.9 nm	521 nm
Au/Ag 3:1	10.64 mg	27 μmol	1.55 mg	9 μmol	78.15 mg	31.5 ± 2.9 nm	500 nm
Au/Ag 1:1	7.09 mg	18 μmol	3.1 mg	18 μmol	78.15 mg	32.7 ± 4.1 nm	465 nm
Au/Ag 1:3	3.55 mg	9 μmol	4.65 mg	27 μmol	78.15 mg	33.4 ± 2.3 nm	432 nm
Ag	-	-	6.2 mg	36 μmol	78.15 mg	31.5 ± 2.6 nm	413 nm

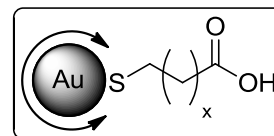
8.4 Ligand Exchange Reactions

General procedure for ligand exchange reaction in water:

I Two-phase system: The ligand ($6 \cdot 10^5$ equiv.) was dissolved in 5 mL of water and under vigorous stirring 1 mL of organic solvent including the nanoparticles was added. The reaction mixture was stirred for 16 h at room temperature whilst a phase transfer could be observed. The organic phase was removed and the aqueous phase was dialysed against water. The purified colloidal solution was stored at 4 °C.

II One-phase system: 10 mL of the nanoparticle solution were stirred at room temperature and $6 \cdot 10^5$ equivalents of the ligand were added. NaOH was added until a basic solution was obtained. After 16 h the solution was purified via dialysis against water and stored at 4 °C.

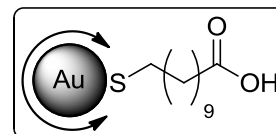
Ligand exchange at Au-Citrate 14 nm with different ligands:



According to the general procedure II ligand exchange reactions at Au-Citrate nanoparticles were performed with 11-mercaptopundecanoic acid (MUDA), 6-mercaptohexanoic acid (MHA), 3-mercaptopropionic acid (MPA), lipoic acid (LA). The resulting nanoparticles were characterized via UV/Vis.

	Ligand	amount _{ligand}	λ_{abs}
Au-MPA	MPA	9 μL	xx
Au-MHA	MHA	15 mg	xx
Au-MUDA	MUDA	22 mg	524 nm
Au-LA	LA	20 mg	531 nm

Ligand exchange with MUDA at Au-DT and Au-Citrate:



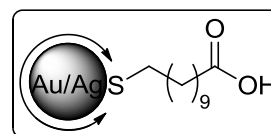
According to the general procedure I 1 mL of Au-DT (4 nm or 7 nm) were added to a solution of 44 mg MUDA (0.2 mmol) and 20 mg NaOH (0.5 mmol, pH>8) in 9 mL water. Dialysis against water three times with 300 mL (MWCO 3500) was performed.

According to general procedure II 10 mL 44 mg MUDA (0.2 mmol) and 20 mg NaOH (0.5 mmol, pH>8) were added to a solution of Au-Citrate (14 nm or 25 nm). Dialysis against water three times with 300 mL, MWCO 3500) was performed.

The nanoparticles were characterized with TEM, DLS and UV/Vis. Au-MUDA 14 nm was synthesized for the publication and characterized additionally with ^1H NMR and IR.

	d_{TEM}	d_{DLS}	λ_{abs}	C_{NP}
4 nm	3.8 ± 0.7 nm	5 ± 1 nm	507 nm	1.26 μM
7 nm	7.5 ± 0.4 nm	8 ± 2 nm	524 nm	1.5 μM
14 nm	14.5 ± 1.2 nm	24 ± 7 nm	527 nm	1 nM
25 nm	25.9 ± 2.3 nm	32 ± 8 nm	532 nm	0.5 nM

Ligand exchange with MUDA at alloyed Au/Ag nanoparticles:

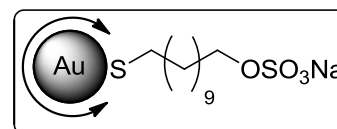


According to general procedure II 10 mL 44 mg MUDA (0.2 mmol) and 20 mg NaOH (0.5 mmol, pH>8) were added to citrate-stabilized gold, silver and the alloyed nanoparticles. Dialysis against water three times with 300 mL (MWCO 3500) was performed.

The nanoparticles were characterized with UV/Vis.

	Particle	λ_{abs}
Au	Au-MUDA	524 nm
Au/Ag 3:1	$\text{Au}_{0.75}\text{Ag}_{0.25}$ -MUDA	499 nm
Au/Ag 1:1	$\text{Au}_{0.5}\text{Ag}_{0.5}$ -MUDA	473 nm
Au/Ag 1:3	$\text{Au}_{0.25}\text{Ag}_{0.75}$ -MUDA	444 nm
0:1	Ag-MUDA	424 nm

Ligand exchange with MUDOLS at Au-DT and Au-Citrate:



The ligand MUDOLS was synthesized separately.

According to the general procedure I 1 mL of Au-DT (7 nm) were added to a solution of 60 mg MUDOLS (0.2 mmol) and 20 mg NaOH (0.5 mmol, pH>8) in 9 mL water. Dialysis against water three times with 300 mL (MWCO 3500) was performed.

According to general procedure II 10 mL 60 mg MUDOLS (0.2 mmol) and 20 mg NaOH (0.5 mmol) were added to a solution of Au-Citrate (14 nm or 25 nm). Dialysis against water three times with 300 mL (MWCO 3500) was performed.

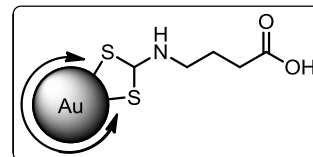
The nanoparticles were characterized with TEM, DLS and UV/Vis. Au-MUDOLS 14 nm was synthesized for the publication and characterized additionally with ^1H NMR and IR.

	d_{TEM}	d_{DLS}	λ_{abs}	c_{NP}
7 nm	7.3 ± 0.9 nm	19 ± 4 nm	524 nm	1.5 μM
14 nm	14.3 ± 1.3 nm	19 ± 3 nm	525 nm	1 nM
25 nm	28.4 ± 4.0 nm	18 ± 5 nm	528 nm	0.5 nM

8.5 Dithiocarbamate Functionalized Gold Nanoparticles

Au-DDT-GABA (\varnothing 14 nm):

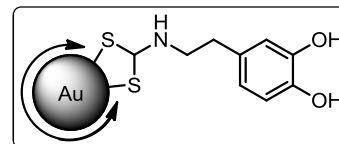
The dithiocarbamate-functionalized gold nanoparticles were synthesized out of citrate-stabilized particles (see above) followed by ligand exchange. 1 μL CS_2 , 5 μL NEt_3 and 1 mg GABA were dissolved in 0.5 mL of Millipore water and sonicated for 5 min. The solution was added to Au-Citrate nanoparticles and stirred at room temperature. The reaction mixture was dialysed against water three times, 300 mL water, MWCO 3500. The solution was stored at 4 $^\circ\text{C}$.



IR (KBr disc): ν/cm^{-1} = 3418.0 ($\nu_{\text{O-H}}$), 2974.9 (s, $\nu_{\text{C-H}}$), 2938.1 (s, $\nu_{\text{C-H}}$), 2738.7, 2677.7, 2492.0, 2184.3, 2108.5, 1589.9 ($\nu_{\text{C=O}}$), 1397.8, 1252.1, 1171.2, 1079.9, 1036.3, 948.7, 895.6, 842.3, 804.5, 665.0, 619.2; **TEM**: $d = 28.4 \pm 4.0$ nm; **UV/Vis**: $\lambda_{\text{max}} = 526$ nm; **DLS**: $d_{\text{hydr}} = 25 \pm 6$ nm.

Au-DDT-DA (\varnothing 14 nm):

The dithiocarbamate-functionalized gold nanoparticles were synthesized out of citrate-stabilized particles (see above) followed by ligand exchange. 1 μL CS_2 , 5 μL NEt_3 and 1 mg dopamine were dissolved in 0.5 mL of Millipore water and sonicated for 5 min. The solution was added to Au-Citrate nanoparticles and stirred at room temperature. The

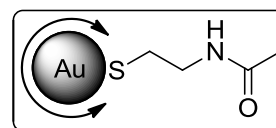


reaction mixture was dialysed against water: three times, 300 mL water, MWCO 3500. The solution was stored at 4 °C.

IR (KBr disc): $\nu/\text{cm}^{-1} = 3431.7$ ($\nu_{\text{O-H}}$), 2922.3 (s, $\nu_{\text{C-H}}$), 2851.1 (s, $\nu_{\text{C-H}}$), 1635.2 ($\nu_{\text{C=O}}$), 1488.0, 1403.4, 1045.2, 948.5, 771.7, 463.8; **TEM**: $d = 25.9 \pm 1.1$ nm; **UV/Vis**: $\lambda_{\text{max}} = 543$ nm; **DLS**: $d_{\text{hydr}} = 35 \pm 7$ nm.

8.6 Positively Charged Gold Nanoparticles

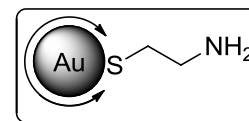
Au-CA-NAC (Ø 14 nm)



According to the general procedure II 12 mg NAc-CA·HCl (0.1 mmol) were added to a solution of Au-Citrate ($c_{\text{NP}} = 1$ nM) and stirred for 20 hours. The reaction mixture was dialysed against water: three times, 300 mL water, MWCO 3500. The solution was stored at 4 °C. A clear violet solution with a particle concentration of 1 nM was obtained and stored at 4 °C.

^1H NMR (400 MHz, D_2O): $\delta/\text{ppm} = 3.09$ (s, 3H, CH_3), 2.58 (d, $J = 15.6$ Hz, 2 H, CH_2), 2.44 (d, $J = 15.6$ Hz, 2 H, CH_2); **IR** (KBr disc): $\nu/\text{cm}^{-1} = 3442.7$ ($\nu_{\text{O-H}}$), 2919.8 (s, $\nu_{\text{C-H}}$), 2580.3, 2359.3, 2336.4, 1636.7 ($\nu_{\text{C=O}}$), 1384.3; **TEM**: $d = 14.1 \pm 3.6$ nm, **UV/Vis**: $\lambda_{\text{max}} = 525$ nm, **DLS**: $d_{\text{hydr}} = 14 \pm 4$ nm.

Cysteamine-coordinated gold nanoparticles (Au-CA Ø 30 nm)



Briefly, 16.4 mg of cysteamine hydrochloride (0.2 mmol) were dissolved in 1 mL water. 400 μL (85 μmol) were added quickly to a solution of 22 mg $\text{HAuCl}_4 \cdot 3 \text{H}_2\text{O}$ (65 μmol) in 20 mL water. The mixture was stirred for 20 min at room temperature in the dark. Then, 10 μL of freshly prepared NaBH_4 solution (3.8 mg in 10 mL, 0.1 μmol) was added quickly under vigorous stirring. After 30 min the mixture turned red and was stirred for another 16 h. Due to instability and incompatibility with the dialysis material, the particles were subsequently functionalized.

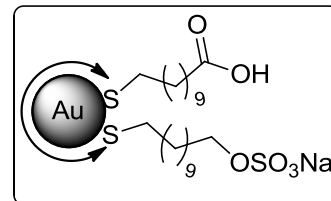
The nanoparticles were characterized with TEM, UV/Vis and DLS.

TEM: $d = 30.5 \pm 5.3$ nm; **UV/Vis**: $\lambda_{\text{max}} = 525$ nm; **DLS**: $d_{\text{hydr}} = 60 \pm 31$ nm.

8.7 Mixed Ligand Shell

Au-MUDA/MUDOLS (Ø 14 nm)

Stock solutions of MUDA and MUDOLS in water with a concentration of 10 mM were prepared. Stoichiometric amounts of MUDA and MUDOLS were added to a solution of Au-Citrate under vigorous stirring. The reaction mixtures were purified via dialysis against water: 3 x 3 h with 300 ml, MWCO 3.5. Clear violet solutions were obtained and stored at 4 °C. 1: Au-MUDA, 2: Au-MUDA/MUDOLS 2:1, 3: Au-MUDA/MUDOLS 1:1, 4: Au-MUDA/MUDOLS 1:2, 5: Au-MUDOLS. The nanoparticles were characterized with UV/Vis, DLS and ζ -potential.



	Shell	λ_{abs}	d_{hydr}	ζ potential	Conductivity
Au-Citrate	-	521 nm	17 ± 3 nm	-28 ± 6 mV	1.11 $\mu\text{S/cm}$
1 Au-MUDA	1:0	526 nm	24 ± 7 nm	-57 ± 17 mV	8.91 $\mu\text{S/cm}$
2 Au-MUDA/OLS	2:1	526 nm	34 ± 4 nm	-58 ± 23 mV	0.67 $\mu\text{S/cm}$
3 Au-MUDA/OLS	1:1	529 nm	38 ± 4 nm	-63 ± 12 mV	0.58 $\mu\text{S/cm}$
4 Au-MUDA/OLS	1:2	526 nm	32 ± 4 nm	-68 ± 12 mV	0.55 $\mu\text{S/cm}$
5 Au-MUDOLS	0:1	525 nm	19 ± 3 nm	-70 ± 13 mV	0.23 $\mu\text{S/cm}$

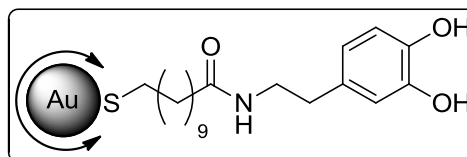
8.8 Functionalization of the Particles Shell

General procedure for the EDC/NHS mediated coupling in water:

10 mL of the nanoparticle solution were transferred in a glass vessel washed with aqua regia and distilled water. $6 \cdot 10^5$ equivalents of the respecting amine, EDC and NHS were dissolved in 0.5 mL of water with $12 \cdot 10^5$ equiv. of NEt_3 and added to the nanoparticle solution. The reaction mixture was stirred overnight and subsequently dialysed against water (3 x 3 h with 300 mL, MWCO 3500).

Au-MUDA-DA

According to the general procedure, dopamine was attached at Au-MUDA nanoparticles 14 nm. A clear red solution was obtained at stored at 4 °C.



7 nm:

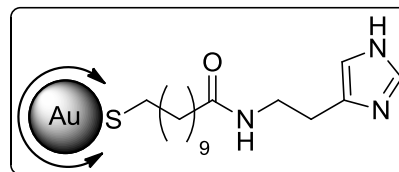
TEM: $d = 7.8 \pm 1.2$ nm; **UV/Vis:** $\lambda_{\text{max}} = 526$ nm; **DLS:** $d_{\text{hydr}} = 9 \pm 2$ nm.

14 nm:

^1H NMR (400 MHz, D_2O): $\delta/\text{ppm} = 6.80$ (d, $J = 7.8$ Hz, 1 H, CH), 6.74 (s, 1 H, CH), 6.54 (d, $J = 7.9$ Hz, 1 H, CH), 5.84 (s, 1 H, NH), 3.46 (q, 2 H, CH_2), 2.85 (t, 2 H, CH_2), 2.67 (t, 2 H, CH_2), 2.32 (s, 3 H, CH_3), 2.14 (t, 2 H, CH_2), 1.64-1.49 (m, 4 H, CH_2), 1.39-1.17 (m, 14 H, CH_2); **IR** (KBr disc): $\nu/\text{cm}^{-1} = 3431.1$, 3018.7 ($\nu_{\text{O-H}}$), 2919.7 (s, $\nu_{\text{C-H}}$), 2849.9 (s, $\nu_{\text{C-H}}$), 1704.4 ($\nu_{\text{C=O}}$, amide), 1656.4, 1488.1, 1404.3, 1384.9, 1290.3, 1231.9, 1081.1, 1003.7, 956.4, 948.6, 815.7, 720.4, 662.9; **TEM:** $d = 14.7 \pm 1.2$ nm; **UV/Vis:** $\lambda_{\text{max}} = 525$ nm; **DLS:** $d_{\text{hydr}} = 26 \pm 6$ nm.

Au-MUDA-HA

According to the general procedure, histamine was attached at Au-MUDA nanoparticles with three different sizes. A clear red solution was obtained at stored at 4 °C.



7 nm:

^1H NMR (400 MHz, D_2O): $\delta/\text{ppm} = 7.62$ (s, 1 H, CH), 7.30 (s, 1 H, CH), 6.90 (m, 1 H, NH), 3.15 (m, 2 H, CH_2), 2.99 (m, 2 H, CH_2), 2.84 (m, 2 H, CH_2), 2.79-2.70 (m, 6 H, CH_2), 2.09-2.03 (m, 1 H,

CH_2), 1.85-1.74 (m, 2 H, CH_2), 1.66-1.58 (m, 1 H, CH_2), 1.52-1.37(m, 1 H, CH_2), 1.33-1.11 (m, 10 H, CH_2); **TEM**: $d = 7.3 \pm 0.9$ nm; **UV/Vis**: $\lambda_{\max} = 524$ nm; **DLS**: $d_{\text{hydr}} = 11 \pm 2$ nm.

14 nm:

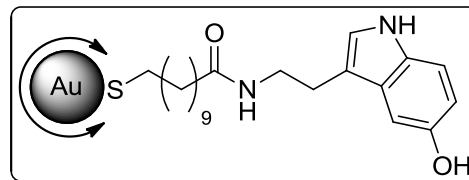
1H NMR (400 MHz, D_2O): $\delta/\text{ppm} = 7.55$ (s, 1 H, CH), 6.81 (s, 1 H, CH), 2.73-2.86 (m, 2 H, CH_2 (HA)), 2.57-2.71 (m, 3 H, CH_2 (HA) + NH), 2.41-2.53 (m, 2 H), 2.21-2.34 (m, 4 H), 2.10-2.21 (m, 3 H), 2.03 (t, $J = 7.7$ Hz, 1 H), 1.52-1.68 (m, 1 H), 1.36-1.48 (m, 1 H), 1.18 (bs, 8 H, CH_2); **IR** (KBr disc): $\nu/\text{cm}^{-1} = 3421.1$ (ν_{O-H}), 3018.8, 2921.4 (s, ν_{C-H}), 2850.0 (s, ν_{C-H}), 1641.1 ($\nu_{C=O}$, amide), 1596.3 (ν_{C-NH}), 1488.2, 1404.2, 957.1, 948.6; **TEM**: $d = 14.3 \pm 0.7$ nm; **UV/Vis**: $\lambda_{\max} = 528$ nm; **DLS**: $d_{\text{hydr}} = 19 \pm 3$ nm

25 nm:

1H NMR (400 MHz, D_2O): $\delta/\text{ppm} = 7.55$ (s, 1 H, CH), 6.81 (s, 1 H, CH), 2.86-2.72 (m, 2 H, CH_2), 2.70-2.57 (m, 2 H, CH_2), 2.50-2.43 (m, 2 H, CH_2), 2.33-2.22 (m, 4 H, CH_2), 2.20-2.11 (m, 3 H, CH_2), 2.10-2.00 (m, 1 H, CH_2), 1.66-1.50 (m, 1 H, CH_2), 1.46-1.36 (m, 1 H, CH_2), 1.31-1.12 (m, 8 H, CH_2); **TEM**: $d = 25.7 \pm 1.2$ nm; **UV/Vis**: $\lambda_{\max} = 534$ nm; **DLS**: $d_{\text{hydr}} = 32 \pm 8$ nm

Au-MUDA-5HT

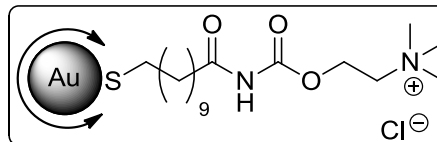
According to the general procedure, serotonin (5-hydroxytryptamine) was attached at Au-MUDA nanoparticles 14 nm. The reaction mixture was stirred under argon atmosphere. The solution was dialysed with degassed water under argon atmosphere and stored under argon atmosphere. A clear red solution was obtained at stored at 4 °C.



1H NMR (400 MHz, D_2O): $\delta/\text{ppm} = 7.40$ -7.30 (m, 1 H, CH), 7.25-7.16 (m, 1 H, CH), 7.08-7.00 (m, 1 H, CH), 6.68-6.75 (m, 1 H, CH), 3.28-3.21 (m, 2 H, CH_2), 2.99-2.92 (m, 2 H, CH_2), 2.15-2.08 (m, 2 H, CH_2), 1.88-1.80 (m, 2 H, CH_2), 1.55-1.42 (m, 4 H, CH_2), 1.36-1.31 (m, 1 H, CH_2), 1.29-1.22 (m, 2 H, CH_2); **IR** (KBr disc): $\nu/\text{cm}^{-1} = 3439.5$ (ν_{O-H}), 2921.3 (s, ν_{C-H}), 2848.0 (s, ν_{C-H}), 1629.3 ($\nu_{C=O}$, amide), 1488.1, 1384.4, 948.3, 617.1; **TEM**: $d = 14.1 \pm 0.9$ nm; **UV/Vis**: $\lambda_{\max} = 528$ nm; **DLS**: $d_{\text{hydr}} = 16 \pm 4$ nm.

Au-MUDA-CB

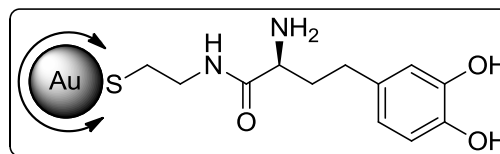
According to the general procedure, carbachol was attached at Au-MUDA nanoparticles 14 nm. The solution was dialysed three times for 2 hours each. The solution was stored under argon atmosphere in an Eppendorf cup.



^1H NMR (400 MHz, D_2O): δ/ppm = 4.47-4.41 (m, 2 H, CH_2), 3.66-3.60 (m, 2 H, CH_2), 3.14 (s, 3 H, CH_3), 3.09-3.00 (m, 4 H, CH_2), 1.88-1.78 (m, 2 H, CH_2), 1.40-1.16 (m, 12 H, CH_2), 1.03-0.98 (m, 2 H, CH_2); **IR** (KBr disc): ν/cm^{-1} = 3426.7 ($\nu_{\text{O-H}}$), 2921.0 (s, $\nu_{\text{C-H}}$), 2848.8 (s, $\nu_{\text{C-H}}$), 1640.8 ($\nu_{\text{C=O}}$, amide), 1576.0, 1487.8, 1465.0, 1408.3, 1342.9, 1238.0, 1099.6, 948.7, 721.5, 663.4; **TEM**: $d = 14.5 \pm 0.7$ nm; **UV/Vis**: $\lambda_{\text{max}} = 532$ nm; **DLS**: $d_{\text{hydr}} = 17 \pm 6$ nm.

Au-CA-His

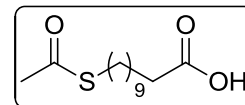
According to the general procedure, L-histamine was attached at Au-CA nanoparticles 30 nm. A clear red solution was obtained at stored at 4 °C.



^1H NMR (400 MHz, D_2O): δ/ppm = 7.73 (s, 1 H, CH), 7.64 (s, 1 H, CH), 7.39 (s, 1 H, CH), 3.11-3.08 (m, 2 H, CH_2), 2.80-2.75 (m, 1 H, CH_2), 1.80-1.77 (m, 4 H, CH_2); **TEM**: $d = 30.7 \pm 7.2$ nm; **UV/Vis**: $\lambda_{\text{max}} = 527$ nm; **DLS**: $d_{\text{hydr}} = 45 \pm 9$ nm.

8.9 Synthesis of the Ligands

11-(Acetylthio)undecanoic acid (AcS-MUDA):

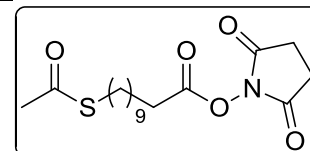


11-(Acetylthio)undecanoic acid was synthesized as reported in the literature

[163]: 500 mg 11-bromoundecanoic acid (1.88 mmol) were dissolved in 10 mL dry DMF. Separately, 322 mg KSAc (2.82 mmol, 1.5 equiv.) were dissolved in 5 mL dry DMF and added dropwise to the solution. After stirring for 1.5 h 50 mL of water was added and a white solid appeared. The precipitate was filtered off, washed three times with water and dried in vacuum. 413.2 mg of a colorless solid (1.6 mmol, 84%) could be obtained.

¹H NMR (400 MHz, CDCl₃): δ /ppm = 2.78 (t, J = 8 Hz, 2 H, CH₂), 2.28 (m, 5 H, CH₂ + CH₃), 1.61-1.52 (m, 2 H, CH₂), 2.52-2.26 (m, 2 H, CH₂), 1.32-1.16 (m, 12 H, CH₂); **¹³C-NMR** (100 MHz, CDCl₃): δ /ppm = 196.3 (C_q, C=O, acetyl), 179.5 (C_q, C=O), 33.9, 31.0 (CH₃), 29.5, 29.4, 29.3, 29.2, 29.2, 29.1, 29.0, 28.8, 24.7; **IR** (KBr disc): ν /cm⁻¹ = 2920.4 (s, ν_{C-H}), 2849.9 (s, ν_{C-H}), 1697.5 ($\nu_{C=O}$, amide), 1432.7, 1408.9, 1290.6, 1138.8, 950.4, 926.1, 631.5; **ESI**: [M+Na]⁺ = 283.1335 (calcd: [M+Na]⁺ = 283.1338); **CHN**: found C 59.84%, H 9.22% (calcd C 59.96%, H 9.29%)

2,5-Dioxopyrrolidin-1-yl-11-(acetylthio)undecanoate (AcS-MUDA-NHS):

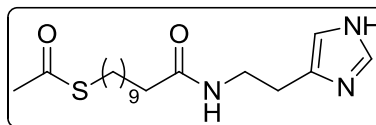


195 mg NHS (1.7 mmol, 1.1 equiv.) and 700 mg AcS-MUDA (1.55 mmol) were dissolved in DCM under stirring at room temperature. 350 mg DCC (1.7 mmol, 1.1 equiv.) were separately dissolved in 5 mL DCM and added slowly. After 30 min a white precipitate appeared. The reaction mixture was stirred overnight. The solvent was removed under reduced pressure. 506 mg (1.42 mmol, 92%) of a colorless powder were obtained.

¹H NMR (400 MHz, CDCl₃): δ /ppm = 2.81-2.77 (m, 6 H, CH₂), 2.53 (t, J = 7.3 Hz, 2 H, CH₂), 2.25 (s, 3 H, CH₃), 1.71-1.63 (m, 2 H, CH₂), 1.52-1.47 (m, 2 H, CH₂), 1.38-1.17 (m, 12 H, CH₂); **¹³C NMR** (100 MHz, CDCl₃): δ /ppm = 196.1 (C_q, C=O, acetyl), 169.3 (2 x C_q, C=O), 168.7 (C_q, C=O), 30.9 (CH₃), 30.7, 29.5, 29.3, 29.2, 29.2, 29.1, 29.0, 28.8, 28.7, 25.6 (2 x CH₂), 24.6; **IR** (KBr disc): ν /cm⁻¹ = 2917.6 (s, ν_{C-H}), 2848.4 (s, ν_{C-H}), 1817.2, 1788.4 ($\nu_{C=O}$), 1736.4 ($\nu_{C=O}$), 1682.1 ($\nu_{C=O}$, amide), 1541.1, 1465.0, 1425.9, 1413.9, 1366.9, 1208.1, 1129.6, 1076.0, 639.1; **ESI**: [M+Na]⁺ = 380.1502 (calcd: [M+Na]⁺ = 380.1600); **CHN**: found C 56.22%, H 7.71%, N 4.82% (calcd C 57.12%, H 7.61%, N 3.92%)

S-(11-((2-(1H-imidazol-4-yl)ethyl)amino)-11-oxoundecyl) ethanethioate (AcS-MUDA-HA):

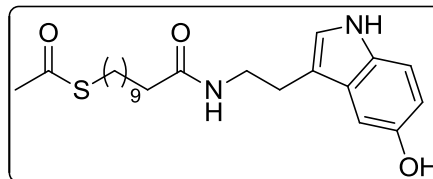
97 mg AcS-MUDA-NHS (0.27 mmol) were dissolved in DMF to form a clear solution. 34 mg HA·2 HCl (0.30 mmol, 1.1 equiv.) and a few drops NEt₃ were added and the solution was stirred overnight. Subsequently 50 mL water were added and a white solid appeared. The precipitate was filtered off and washed three times with water. The crude product was dissolved in CHCl₃ and filtered again. After evaporation 70 mg (0.19 mmol, 70%) of a colorless powder was obtained.



¹H NMR (400 MHz, CDCl₃): δ/ppm = 7.50 (s, 1 H, CH_{ar}), 6.75 (s, 1 H, CH_{ar}), 6.33 (br s, 1 H, NH), 3.52-3.42 (m, 2 H, CH₂ (HA)), 2.79-2.69 (m, 2 H, CH₂ (HA)), 2.53-2.39 (m, 2 H, CH₂), 2.56 (s, 3 H, CH₃), 2.10 (t, J = 7.2 Hz, 2 H, CH₂), 1.59-1.43 (m, 4 H, CH₂), 1.26-1.14 (m, 12 H, CH₂); **¹³C NMR** (100 MHz, CDCl₃): δ/ppm = 196.4 (C_q, C=O, acetyl), 173.7 (C_q, C=O, amide), 134.8 (CH, C_{ar}), 127.6 (C_q, C_{ar}), 118.6 (CH, C_{ar}), 39.2 (CH₂ (HA)), 36.9 (CH₂ (HA)), 30.7 (CH₃), 29.5, 29.3, 29.3, 29.2, 29.1, 28.7, 28.4, 26.9, 25.7; **IR** (KBr disc): ν/cm⁻¹ = 2920.7 (ν_{C-H}), 2850.6 (ν_{C-H}), 1691.9 (ν_{C=O}), 1638.9 (ν_{C=O}), 1575.2 (ν_{CN-H}), 1466.1, 1452.7, 1255.8, 1090.7, 623.3; **ESI**: [M+H]⁺ = 354.2221 (calcd: [M+H]⁺ = 354.2210); **CHN**: found C 59.72%, H 8.67%, N 11.37% (calcd C 61.15%, H 8.84%, N 11.89%)

S-(11-((2-(5-hydroxy-1H-indol-3-yl)ethyl)amino)-11-oxoundecyl) ethanethioate (AcS-MUDA-5HT):

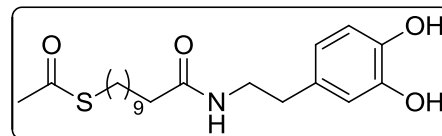
97 mg AcS-MUDA-NHS (0.27 mmol) were dissolved in DMF to form a clear solution. 64 mg 5HT·HCl (0.30 mmol, 1.1 equiv.) and a few drops NEt₃ were added and the solution was stirred overnight. Subsequently 50 mL water were added and a white solid appeared. The precipitate was filtered off and washed three times with water. The crude product was dissolved in CHCl₃ and filtered again. After evaporation 33 mg (0.08 mmol, 29%) of a colorless powder were obtained.



¹H NMR (400 MHz, CDCl₃): δ/ppm = 8.02 (s, 1 H, NH), 7.19-7.12 (m, 1 H, CH), 6.99-6.88 (m, 2 H, CH), 6.78-6.72 (m, 1 H, CH), 6.27 (s, 1 H, NH), 5.59 (bs, 1 H, OH), 3.54-3.46 (m, 2 H, CH₂), 2.85-2.75 (m, 4 H, CH₂), 2.25 (s, 3 H, CH₃), 2.05 (t, J = 7.5 Hz, 2 H, CH₂), 1.93-1.82 (m, 4 H, CH₂), 1.23-1.15 (m, 12 H, CH₂); **¹³C NMR** (100 MHz, CDCl₃): δ/ppm = 195.5, 172.4, 155.9, 149.1, 130.4, 127.0, 121.9, 111.1, 110.8, 102.1, 48.0, 38.6, 35.9, 32.9, 29.9, 29.6, 28.5, 28.3, 28.2, 28.1, 28.0, 24.6, 23.9.

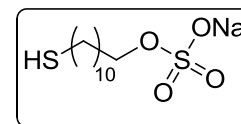
S-(11-((3,4-dihydroxyphenethyl)amino)-11-oxoundecyl) ethanethioate (AcS-MUDA-DA):

97 mg AcS-MUDA-NHS (0.27 mmol) were dissolved in 4 mL DMF to form a clear solution. 57 mg DA·HCl (0.30 mmol, 1.1 equiv.) in 1 mL DMF were added and the solution was stirred overnight. Subsequently 50 mL water were added and a white solid appeared. The precipitate was filtered off and washed three times with water. The crude product was dissolved in CHCl₃ and filtered again. After evaporation 54 mg (0.14 mmol, 52%) of a colorless powder were obtained.



¹H NMR (400 MHz, CDCl₃): δ /ppm = 6.80 (d, J = 7.80 Hz, 1 H, CH), 6.74 (s, 1 H, CH), 6.54 (d, J = 7.92, 1 H, CH), 5.84 (s, 1 H, NH), 3.46 (q, J = 6.28 Hz, 2 H, CH₂), 2.85 (t, J = 7.39 Hz, 2 H, CH₂), 2.67 (t, J = 7.03 Hz, 2 H, CH₂), 2.32 (s, 3 H, CH₃), 2.14 (t, J = 8.10 Hz, 2 H, CH₂), 1.64-1.49 (m, 4 H, CH₂), 1.39-1.17 (m, 4 H, CH₂); **¹³C NMR** (100 MHz, CDCl₃): δ /ppm = 196.7, 174.5, 144.5, 143.2, 130.5, 120.4, 115.4, 115.1, 40.9, 36.8, 34.9, 30.7, 29.5, 29.3, 29.3, 29.2, 29.1, 29.1, 29.0, 28.7, 28.3; **IR** (KBr disc): ν /cm⁻¹ = 2919.7 (ν_{C-H}), 2849.9 (ν_{C-H}), 1704.4 ($\nu_{C=O}$), 1656.4 ($\nu_{C=O}$, amide), 1488.1, 1404.3, 1384.9, 1231.9, 956.4, 948.6; 662.9; **ESI**: [M+H]⁺ = 418.27 (calcd: [M+Na]⁺ = 418.20); **CHN**: found C 63.22%, H 8.49%, N 3.66% (calcd: C 63.76%, H 8.41%, N 3.54%)

Sodium 11-mercaptoundecyl sulfate (MUDOLS):

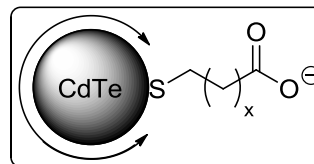


In a flame-dried vessel under argon atmosphere, 353 mg of 11-mercaptoundecanol (1.72 mmol) were dissolved in 3 mL dry DMF. Separately, 395 mg of SO₃·DMF complex (2.50 mmol, 1.5 equiv.) were dissolved in 1 mL dry DMF and added to the solution. After stirring for 1 h at room temperature the solvent was removed under reduced pressure (OPV) and the residue was dissolved in 4 mL of 1 M NaOH. A white precipitate appeared. 15 mL of ethanol were added and washed three times. The product was dried in vacuum. 280 mg of a colorless solid (0.91 mmol, 53%) could be obtained, the dimer was formed.

¹H NMR (200 MHz, DMSO-d₆): δ /ppm = 3.68 (t, J = 6.6 Hz, 2 H, CH₂), 3.35 (t, J = 6.3 Hz, 2 H, CH₂), 2.27-2.61 (m, 4 H, CH₂), 2.56-2.49 (m, 2 H, CH₂), 1.67-1.52 (m, 4 H, CH₂), 1.36-1.24 (m, 10 H, CH₂); **¹³C NMR** (200 MHz, DMSO-d₆): δ /ppm = 65.6, 60.7, 32.5, 29.1, 29.0, 28.9, 28.8, 28.6, 28.5, 27.7, 25.5; **IR** (KBr disc): ν /cm⁻¹ = 2918.7 (s, ν_{C-H}), 2849.9 (s, ν_{C-H}), 1614.8, 1470.0, 1261.7 & 1205.1 & 1128.1 (s, ν_{R-OSO_2-OR}), 1068.8, 966.4, 831.8, 718.9, 628.7, 586.3; **ESI**: [M+Na]⁺ = 633.16 (calcd: [M+Na]⁺ = 633.16); **CHN**: C₁₁H₂₃ClNa₂O₄S₂ found C 35.68%, H 6.01% (calcd: C 36.21%, H 6.35%).

8.10 Synthesis of Quantum Dots

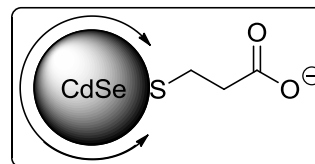
Mercaptocarboxylic acid functionalized cadmium telluride nanoparticles (CdTe-ligand)



55 mg of Te powder (0.43 mmol, 2 equiv.) and 42 mg NaBH_4 (1.11 mmol, 5.3 equiv.) were dissolved in 5 mL of degassed water under argon atmosphere and heated to 70 °C for 1.5 h. In parallel 56 mg $\text{Cd}(\text{OAc})_2 \cdot 2\text{H}_2\text{O}$ (0.21 mmol) and 4.8 equiv. of the respective ligand were dissolved in 12 mL of degassed water, NaOH was added until the solution cleared up. Both precursor solutions were combined and heated up to 100 °C for 4 h and then quenched with an ice bath. The solution was dialysed against water three times (MWCO 3500) and stored at 4 °C. The particles were characterized with TEM, DLS, UV/Vis and fluorescence spectroscopy.

	Ligand	Amount	d_{TEM}	d_{DLS}	λ_{abs}	λ_{em}
CdTe-TGA	TGA	33 μL	4.1 ± 0.3 nm	8 ± 1 nm	540 nm	594 nm
CdTe-MPA	MPA	42 μL	4.3 ± 0.4 nm	7 ± 1 nm	498 nm	574 nm
CdTe-MPSA	MPSA	180 mg	4.9 ± 0.4 nm	5 ± 1 nm	478 nm	544 nm

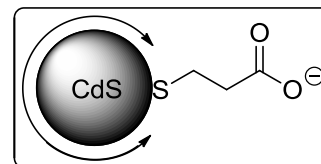
Mercaptocarboxylic acid functionalized cadmium selenide nanoparticles (CdSe-ligand)



34 mg of Se powder (0.43 mmol, 2 equiv.) and 42 mg NaBH_4 (1.11 mmol, 5.3 equiv.) were dissolved in 5 mL of degassed water under argon atmosphere at rt for 1.5 h. In parallel 56 mg $\text{Cd}(\text{OAc})_2 \cdot 2\text{H}_2\text{O}$ (0.21 mmol) and 4.8 equiv. of the respective ligand were dissolved in 12 mL of degassed water, NaOH was added until the solution cleared up. Both precursor solutions were combined and heated up to 100 °C. The reaction was quenched with an ice bath after 4 hours. The solution was dialysed against water three times (MWCO 3500) and stored at 4 °C. The particles were characterized with TEM, DLS, UV/Vis and fluorescence spectroscopy.

	Ligand	Amount	d _{TEM}	d _{DLS}	λ _{abs}	λ _{em}
CdSe-TGA	TGA	33 μL	3.5 ± 0.4 nm	7 ± 2 nm	540 nm	670 nm (br)
CdSe-MPA	MPA	42 μL	3.9 ± 0.2 nm	5 ± 1 nm	473 nm	543 nm

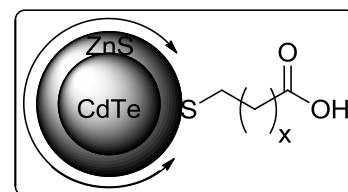
Mercaptocarboxylic acid functionalized cadmium sulfide nanoparticles (CdS-ligand)



34 mg of Na₂S (0.4 mmol, 2 equiv.) were dissolved in 10 mL of degassed water under argon atmosphere. In parallel 54 mg Cd(OAc)₂·2H₂O (0.2 mmol) and 42 μL of MPA (0.48 mmol, 2.4 equiv.) were dissolved in 20 mL of degassed water, NaOH was added until the solution cleared up. The sulfide precursor solution was added and the reaction mixture was heated up to 100 °C. The reaction was quenched with an ice bath after 4 h. The particle solution was dialysed against water three times (MWCO 3500) and stored at 4 °C. The particles were characterized with TEM and DLS measurements, UV/Vis and fluorescence spectroscopy.

	Ligand	Amount	d _{TEM}	d _{DLS}	λ _{abs}	λ _{em}
CdS-MPA	MPA	42 μL	3.7 ± 0.5 nm	5 ± 1 nm	430 nm	616 nm

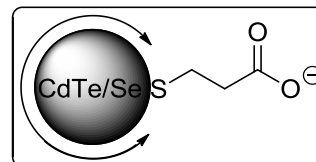
Passivation with ZnS of mercaptocarboxylic acid functionalized quantum dots (CdTe/ZnS-ligand)



To a purified quantum dot solution in water 17 mg ZnCl₂ (0.12 mmol), 9 mg Na₂S (0.12 mmol) and 0.48 mmol ligand were added and stirred under argon for 3 hours. The pH was adjusted to ≥8 with NaOH. The reaction mixture was heated to 60 °C for 3 h. The particle solution was purified with dialysis against water (MWCO 3500) and stored at 4 °C. The particles were characterized with TEM and DLS measurements, UV/Vis and fluorescence spectroscopy and XRD analysis

	Ligand	Amount	d _{TEM}	d _{DLS}	λ _{abs}	λ _{em}
CdTe/ZnS-TGA	TGA	33 μL	4.3 ± 0.2 nm	11 ± 2 nm	542 nm	590 nm
CdTe/ZnS-MPA	MPA	42 μL	4.5 ± 0.3 nm	6 ± 1 nm	500 nm	574 nm

Synthesis of $\text{CdTe}_x\text{Se}_{1-x}$ quantum dots



$\text{CdTe}_x\text{Se}_{1-x}$ quantum dots were synthesized using standard Schlenk technique. The precursor solutions of NaHSe and NaHTe were freshly prepared. For NaHTe 52 mg Te powder (0.4 mmol) and 37 mg NaBH_4 (1 mmol, 2.5 equiv.) were dissolved in 10 mL of degassed water and under argon atmosphere. The reaction mixture was heated to 75 °C for 1 h and then cooled to room temperature giving a red solution. For NaHSe 34 mg Se powder (0.4 mmol) and 37 mg NaBH_4 (1 mmol, 2.5 equiv.) were dissolved in 10 mL of degassed water and under argon atmosphere, cooled in an ice bath for 3 h and then heated up to room temperature giving a colorless solution. In the meantime a third flask was loaded with 54 mg $\text{Cd}(\text{OAc})_2 \cdot 2\text{H}_2\text{O}$ (0.2 mmol), 42 μL MPA (0.48 mmol) and 20 mL of water. NaOH was added until the solution cleared up. The mixture was heated up to 100 °C. Then both precursor solutions were added simultaneously to the Cd^{2+} precursor solution in different molar ratios ($x = 0.1$ to 0.9) and stirred for 4 h. The reaction mixture was quenched with an ice bath and the particle solution was dialyzed against water (three times, MWCO 3500). The particles were characterized with TEM and DLS, UV/Vis and fluorescence spectroscopy, XRD analysis and EDX spot analysis.

	x	d_{TEM}	d_{DLS}	EDX Te/Se	λ_{abs}	λ_{em}
CdSe-MPA	0	2.6 ± 0.2 nm	5 ± 1 nm	0.00/1.00	485 nm	584 nm
$\text{CdTe}_{0.1}\text{Se}_{0.9}$ -MPA	0.1	2.4 ± 0.3 nm	6 ± 2 nm	0.13/0.87	487 nm	598 nm
$\text{CdTe}_{0.2}\text{Se}_{0.8}$ -MPA	0.2	2.9 ± 0.2 nm	8 ± 2 nm	0.24/0.76	486 nm	581 nm
$\text{CdTe}_{0.3}\text{Se}_{0.7}$ -MPA	0.3	2.3 ± 0.3 nm	7 ± 2 nm	0.30/0.70	488 nm	579 nm
$\text{CdTe}_{0.4}\text{Se}_{0.6}$ -MPA	0.4	2.5 ± 0.2 nm	7 ± 2 nm	0.38/0.62	492 nm	573 nm
$\text{CdTe}_{0.5}\text{Se}_{0.5}$ -MPA	0.5	2.6 ± 0.2 nm	6 ± 2 nm	0.61/0.39	498 nm	567.5 nm
$\text{CdTe}_{0.6}\text{Se}_{0.4}$ -MPA	0.6	2.5 ± 0.3 nm	6 ± 1 nm	0.68/0.32	500 nm	564 nm
$\text{CdTe}_{0.7}\text{Se}_{0.3}$ -MPA	0.7	2.3 ± 0.3 nm	5 ± 2 nm	0.68/0.32	498 nm	564 nm
$\text{CdTe}_{0.8}\text{Se}_{0.2}$ -MPA	0.8	2.5 ± 0.2 nm	6 ± 2 nm	0.60/0.40	506 nm	560.5 nm
$\text{CdTe}_{0.9}\text{Se}_{0.1}$ -MPA	0.9	2.5 ± 0.2 nm	8 ± 2 nm	0.88/0.12	518 nm	559 nm
CdTe-MPA	1.0	2.6 ± 0.2 nm	7 ± 1 nm	1.00/0.00	520 nm	555 nm

8.11 Biological Functionality

Animals

Female and male Wistar rats with a body mass of 200 - 250 g were used. The animals were bred and housed at the institute for Veterinary Physiology and Biochemistry of the Justus-Liebig-University Giessen at an ambient temperature of 22.5 °C and air humidity of 50 - 55% on a 12 h : 12 h light-dark cycle with free access to water and food until the time of the experiment. Experiments were approved by the named animal welfare officer of the Justus-Liebig-University (administrative number 487_M) and performed according to the German and European animal welfare law.

Solutions

The standard solution for the *Ussing* chamber experiments was a buffer solution containing: NaCl 107 mmol l⁻¹, KCl 4.5 mmol l⁻¹, NaHCO₃ 25 mmol l⁻¹, Na₂HPO₄ 1.8 mmol l⁻¹, NaH₂PO₄ 0.2 mmol l⁻¹, CaCl₂ 1.25 mmol l⁻¹, MgSO₄ 1 mmol l⁻¹ and glucose 12 mmol l⁻¹. The solution was gassed with carbogen (5% CO₂ in 95% O₂, v/v); pH was 7.4. For the Cl⁻-free buffer, NaCl and KCl were substituted by Na gluconate and K gluconate (KGluc), respectively. The Ca²⁺ concentration in the Cl⁻-free buffer was increased to 5.75 mmol l⁻¹ to compensate for the Ca²⁺-buffering properties of gluconate.

Tissue preparation

Animals were killed by stunning followed by exsanguination. The serosa and tunica muscularis were stripped away by hand to obtain a mucosa-submucosa preparation of the distal colon. Briefly, the colon was placed on a small plastic rod with a diameter of 5 mm. A circular incision was made near the anal end with a blunt scalpel, and the serosa together with the tunica muscularis was gently removed in a proximal direction. Two segments of the distal colon of each rat were prepared.

Short-circuit current measurements

The mucosa-submucosa preparation was fixed in a modified *Ussing* chamber bathed with a volume of 3.5 mL on each side of the mucosa. The tissue was incubated at 37 °C and short-circuited by a computer-controlled voltage-clamp device (Ingenieur Büro für Mess- und Datentechnik Mussler, Aachen, Germany) with correction for solution resistance. Tissue conductance (Gt) was measured every minute by the voltage deviation induced by a current pulse (±50 µA, duration 200 ms) under open-circuit conditions. Short-circuit current (I_{sc}) was continuously recorded on a chart-recorder. I_{sc}

is expressed as $\mu\text{Eq h}^{-1} \text{ cm}^{-2}$, e. g. the flux of a monovalent ion per time and area, with $1 \mu\text{Eq h}^{-1} \text{ cm}^{-2} = 26.9 \mu\text{A cm}^{-2}$. At the end of each experiment, tissue viability was tested by administration of the cholinergic agonist, carbachol ($5 \times 10^{-5} \text{ mol l}^{-1}$ at the serosal side) and/or the administration of forskolin ($5 \times 10^{-6} \text{ mol l}^{-1}$ at the mucosal and the serosal side), an activator of adenylate cyclase(s), which induce a strong Ca^{2+} -respective cAMP-dependent Cl^{-} secretion.

Drugs

Au-MUDOLS, Au-MUDA-HA, carbachol, cimetidine, histamine dihydrochloride, and mepyramine were dissolved in aqueous stock solutions. Forskolin (Calbiochem, Bad Soden, Germany) was dissolved in ethanol (final maximal concentration 0.25%, v/v). Tetrodotoxin was dissolved in $2 \times 10^{-2} \text{ mol l}^{-1}$ citrate buffer. If not indicated otherwise, drugs were from Sigma (Taufkirchen, Germany).

Statistics

Results are given as means \pm SEM, with the number (n) of investigated tissues. When means of several groups had to be compared, an analysis of variance was performed followed by post hoc Tukey's-test. For the comparison of two groups, a Mann-Whitney U-test was applied. $P < 0.05$ was considered to be statistically significant.

9. References

- 1 Ostwald, W. (1914) *Die Welt der vernachlässigten Dimensionen. Eine Einführung in die moderne Kolloidchemie mit besonderer Berücksichtigung ihrer Anwendungen*, Steinkopff Verlag, Dresden.
- 2 Special Issue: Nanotechnology & Nanomaterials, Nanotoxicology & Nanomedicine (2014). *Angew. Chem. Int. Ed.*, **53** (46), 12265–12642.
- 3 Goesmann, H. and Feldmann, C. (2010) Nanoparticulate Functional Materials. *Angew. Chem. Int. Ed.*, **49** (8), 1362–1395.
- 4 Faraday, M. (1857) Experimental Relations of Gold (and other Metals) to Light. *Phil. Trans. R. Soc. Lond.*, **147**, 145–181.
- 5 Kunckels, J. (1676) *Nützliche Observationes oder Anmerkungen von Auro und Argento Potabili*, Schutzens, Hamburg.
- 6 Graham, T. (1861) Liquid Diffusion Applied to Analysis. *Phil. Trans. R. Soc.*, **151**, 183–190.
- 7 GDCh (ed) (2014) *Nano. Ein Magazin der Gesellschaft Deutscher Chemiker*, Spektrum der Wissenschaft Verlagsgesellschaft mbH, Heidelberg.
- 8 Savage, G. (1975) *Glass and Glassware*, Octopus Books, London.
- 9 British Museum The Lycurgus Cup. <http://blog.britishmuseum.org/2014/04/30/the-lycurgus-cup-transformation-in-glass/>; 02.02.2016.
- 10 Dörfler, H.-D. (2002) *Grenzflächen und kolloid-disperse Systeme*, Springer Verlag.
- 11 LaMer, V. and Dinegar, R.H. (1950) Theory, Production and Mechanism of Formation of Monodisperse Hydrosols. *J. Am. Chem. Soc.*, **72** (11), 4847–4854.
- 12 Chang, J. and Waclawik, E.R. (2014) Colloidal semiconductor nanocrystals: Controlled synthesis and surface chemistry in organic media. *RSC Adv.*, **4** (45), 23505–23527.
- 13 Kamat, P.V. (2002) Photophysical, Photochemical and Photocatalytic Aspects of Metal Nanoparticles. *J. Phys. Chem. B*, **106** (32), 7729–7744.
- 14 Daniel, M.-C. and Astruc, D. (2004) Gold Nanoparticles: Assembly, Supramolecular Chemistry, Quantum-Size-Related Properties, and Applications toward Biology, Catalysis, and Nanotechnology. *Chem. Rev.*, **104** (1), 293–346.
- 15 Schimpf, S., Lucas, M., Mohr, C., Rodemerck, U., Brückner, A., Radnik, J., Hofmeister, H., Claus, P. (2002) Supported gold nanoparticles: in-depth catalyst characterization and application in hydrogenation and oxidation reactions. *Catal. Today*, **72** (1-2), 63–78.

- 16 Turkevich, J., Stevenson, P.C., Hillier, J. (1951) A study of the nucleation and growth processes in the synthesis of colloidal gold. *Discuss. Faraday Soc.*, **11**, 55–75.
- 17 Frens, G. (1973) Controlled Nucleation for the Regulation of the Particle Size in Monodisperse Gold Suspensions. *Nature Phys. Sci.*, **241** (105), 20–22.
- 18 Frens, G. (1972) Particle size and sol stability in metal colloids. *Kolloid-Z. u. Z. Polymere (Kolloid-Zeitschrift und Zeitschrift für Polymere)*, **250** (7), 736–741.
- 19 Brust, M., Walker, M., Bethell, D., Schiffrin, D.J., Whyman, R. (1994) Synthesis of Thiol-derivatised Gold Nanoparticles in a Two-phase Liquid-Liquid System Synthesis of Thiol-derivatised Gold Nanoparticles in a Two-phase Liquid-Liquid System. *J. Chem. Soc., Chem. Commun.* (7), 801–802.
- 20 Brust, M., Fink, D., Bethell, D., Schiffrin, D.J., Kiely, C. (1995) Synthesis and Reactions of Functionalized Gold Nanoparticles. *J. Am. Chem. Soc., Chem. Commun.* (16), 1655–1656.
- 21 Kolb, U., Quaiser, S.A., Winter, M., Reetz, M.T. (1996) Investigation of Tetraalkylammonium Bromide Stabilized Palladium/Platinum Bimetallic Clusters Using Extended X-ray Absorption Fine Structure Spectroscopy. *Chem. Mater.*, **8** (8), 1889–1894.
- 22 Perez, H., Pradeau, J.-P., Albouy, P.-A., Perez-Omil, J. (1999) Synthesis and Characterization of Functionalized Platinum Nanoparticles. *Chem. Mater.*, **11** (12), 3460–3463.
- 23 Subramanian, V., Wolf, E., Kamat, P.V. (2001) Semiconductor - Metal Composite Nanostructures. To What Extent Do Metal Nanoparticles Improve the Photocatalytic Activity of TiO₂ Films? *J. Phys. Chem. B*, **105** (46), 11439–11446.
- 24 Gittins, D.I. and Caruso, F. (2001) Spontaneous Phase Transfer of Nanoparticulate Metals from Organic to Aqueous Media. *Angew. Chem. Int. Ed.*, **40** (16), 3001–3004.
- 25 Rucareanu, S., Gandubert, V.J., Lennox, R.B. (2006) 4-(*N,N*-Dimethylamino)pyridine-Protected Au Nanoparticles: Versatile Precursors for Water- and Organic-Soluble Gold Nanoparticles. *Chem. Mater.*, **18** (19), 4674–4680.
- 26 Zheng, N., Fan, J., Stucky, G.D. (2006) One-Step One-Phase Synthesis of Monodisperse Noble-Metallic Nanoparticles and Their Colloidal Crystals. *J. Am. Chem. Soc.*, **128** (20), 6550–6551.
- 27 Schmid, G., Pfeil, R., Boese, R., Bandermann, F., Meyer, S., Calis, G.H.M., van der Velden, Jan W. A. (1981) Au₅₅[P(C₆H₅)₃]₁₂Cl₆ - ein Goldcluster ungewöhnlicher Größe. *Chem. Ber.*, **114** (11), 3634–3642.
- 28 Nikoobakht, B. and El-Sayed, M.A. (2003) Preparation and Growth Mechanism of Gold Nanorods (NRs) Using Seed-Mediated Growth Method. *Chem. Mater.*, **15** (10), 1957–1962.

-
- 29 Schwartzberg, A.M., Olson, T.Y., Talley, C.E., Zhang, J.Z. (2006) Synthesis, characterization, and tunable optical properties of hollow gold nanospheres. *J. Phys. Chem. B*, **110** (40), 19935–19944.
- 30 Alkilany, A.M., Abulateefeh, S.R., Mills, K.K., Yaseen, A.I.B., Hamaly, M.A., Alkhatib, H.S., Aiedeh, K.M., Stone, J.W. (2014) Colloidal stability of citrate and mercaptoacetic acid capped gold nanoparticles upon lyophilization: effect of capping ligand attachment and type of cryoprotectants. *Langmuir*, **30** (46), 13799–13808.
- 31 Giersig, M. and Mulvaney, P. (1993) Preparation of ordered colloid monolayers by electrophoretic deposition. *Langmuir*, **9** (12), 3408–3413.
- 32 Njoki, P., Lim, I.-I., Mott, D., Park, H.-Y., Khan, B., Mishra, S., Sujakumar, R., Luo, J., Zhong, C.-J. (2007) Size Correlation of Optical and Spectroscopic Properties for Gold Nanoparticles. *J. Phys. Chem. C*, **111** (40), 14664–14669.
- 33 Kelly, K.L., Coronado, E., Zhao, L.L., Schatz, G.C. (2003) The Optical Properties of Metal Nanoparticles: The Influence of Size, Shape, and Dielectric Environment. *J. Phys. Chem. B*, **107** (3), 668–677.
- 34 Duonghong, D., Ramsden, J., Grätzel, M. (1982) Dynamics of Interfacial Electron-Transfer Processes in Colloidal Semiconductor Systems. *J. Am. Chem. Soc.*, **104** (11), 2977–2985.
- 35 Rossetti, R. and Brus, L. (1982) Electron-hole recombination emission as a probe of surface chemistry in aqueous cadmium sulfide colloids. *J. Phys. Chem.*, **86** (23), 4470–4472.
- 36 Henglein, A. (1982) Photochemistry of Colloidal Cadmium Sulfide 2. Effects of Adsorbed Methyl Viologen and of Colloidal Platinum. *J. Phys. Chem.*, **86** (23), 2291–2293.
- 37 Brus, L.E. (1983) A simple model for the ionization potential, electron affinity, and aqueous redox potentials of small semiconductor crystallites. *J. Chem. Phys.*, **79** (11), 5566.
- 38 Alivisatos, A.P. (1996) Semiconductor Clusters, Nanocrystals, and Quantum Dots. *Science*, **271** (5251), 933–937.
- 39 Murray, C.B., Norris, D.J., Bawendi, M.G. (1993) Synthesis and Characterization of Nearly Monodisperse CdE (E = S, Se, Te) Semiconductor Nanocrystallites. *J. Am. Chem. Soc.*, **115** (19), 8706–8715.
- 40 Liu, W., Howarth, M., Greytak, A.B., Zheng, Y., Nocera, D.G., Ting, A.Y., Bawendi, M.G. (2008) Compact biocompatible quantum dots functionalized for cellular imaging. *J. Am. Chem. Soc.*, **130** (4), 1274–1284.
- 41 Biju, V., Itoh, T., Anas, A., Sujith, A., Ishikawa, M. (2008) Semiconductor quantum dots and metal nanoparticles: syntheses, optical properties, and biological applications. *Anal. Bioanal. Chem.*, **391** (7), 2469–2495.

-
- 42 Zhang, H., Zhou, Z., Yang, B., Gao, M. (2003) The Influence of Carboxyl Groups on the Photoluminescence of Mercaptocarboxylic Acid-Stabilized CdTe Nanoparticles. *J. Phys. Chem. B*, **107** (1), 8–13.
- 43 Zhang, Y.-h., Zhang, H.-s., Ma, M., Guo, X.-f., Wang, H. (2009) The influence of ligands on the preparation and optical properties of water-soluble CdTe quantum dots. *Appl. Surf. Sci.*, **255** (9), 4747–4753.
- 44 Hannachi, L. and Bouarissa, N. (2008) Electronic structure and optical properties of $\text{CdSe}_x\text{Te}_{1-x}$ mixed crystals. *Superlattices Microstruct.*, **44** (6), 794–801.
- 45 Gaponik, N., Talapin, D.V., Rogach, A.L., Hoppe, K., Shevchenko, E.V., Kornowski, A., Eychmüller, A., Weller, H. (2002) Thiol-Capping of CdTe Nanocrystals: An Alternative to Organometallic Synthetic Routes. *J. Phys. Chem. B*, **106** (29), 7177–7185.
- 46 Rogach, A.L., Katsikas, A., Kornowski, A., Su, D., Eychmüller, A., Weller, H. (1996) Synthesis and Characterization of Thiol-Stabilized CdTe Nanocrystals. *Ber. Bunsenges. Phys. Chem.*, **100** (11), 1772–1778.
- 47 Dong, C. and Ren, J. (2012) Water-soluble mercaptoundecanoic acid (MUA)-coated CdTe quantum dots: one-step microwave synthesis, characterization and cancer cell imaging. *Luminescence*, **27** (3), 199–203.
- 48 He, Y., Sai, L.-M., Lu, H.-T., Hu, M., Lai, W.-Y., Fan, Q.-L., Wang, L.-H., Huang, W. (2007) Microwave-Assisted Synthesis of Water-Dispersed CdTe Nanocrystals with High Luminescent Efficiency and Narrow Size Distribution. *Chem. Mater.*, **19** (3), 359–365.
- 49 Zhang, H., Wang, L., Xiong, H., Hu, L., Yang, B., Li, W. (2003) Hydrothermal Synthesis for High-Quality CdTe Nanocrystals. *Adv. Mater.*, **15** (20), 1712–1715.
- 50 Wang, C.L., Zhang, H., Zhang, J.H., Li, M.J., Sun, H.Z., Yang, B. (2007) Application of Ultrasonic Irradiation in Aqueous Synthesis of Highly Fluorescent CdTe/CdS Core-Shell Nanocrystals. *J. Phys. Chem. C*, **111** (6), 2465–2469.
- 51 Wang, Q., Xu, Y., Zhao, X., Chang, Y., Liu, Y., Jiang, L., Sharma, J., Seo, D.-K., Yan, H. (2007) A facile one-step in situ functionalization of quantum dots with preserved photoluminescence for bioconjugation. *J. Am. Chem. Soc.*, **129** (20), 6380–6381.
- 52 Jeong, S., Achermann, M., Nanda, J., Ivanov, S., Klimov, V.I., Hollingsworth, J.A. (2005) Effect of the thiol-thiolate equilibrium on the photophysical properties of aqueous CdSe/ZnS nanocrystal quantum dots. *J. Am. Chem. Soc.*, **127** (29), 10126–10127.
- 53 Bailey, R.E. and Nie, S. (2003) Alloyed semiconductor quantum dots: tuning the optical properties without changing the particle size. *J. Am. Chem. Soc.*, **125** (23), 7100–7106.

- 54 Jiang, W., Singhal, A., Zheng, J., Wang, C., Chan, W.C.W. (2006) Optimizing the Synthesis of Red- to Near-IR-Emitting CdS-Capped CdTe_xSe_{1-x} Alloyed Quantum Dots for Biomedical Imaging. *Chem. Mater.*, **18** (20), 4845–4854.
- 55 Piven, N., Susha, A.S., Döblinger, M., Rogach, A.L. (2008) Aqueous Synthesis of Alloyed CdSe_xTe_{1-x} Nanocrystals. *J. Phys. Chem. C*, **112** (39), 15253–15259.
- 56 Yang, F., Xu, Z., Wang, J., Zan, F., Dong, C., Ren, J. (2013) Microwave-assisted aqueous synthesis of new quaternary-alloyed CdSeTeS quantum dots; and their bioapplications in targeted imaging of cancer cells. *Luminescence*, **28** (3), 392–400.
- 57 Medinitz, I., Uyeda, T., Goldman, E., Mattoussi, H. (2005) Quantum dot bioconjugates for imaging, labelling and sensing. *Nature Mater.*, **4** (6), 435–446.
- 58 Kairdolf, B.A., Smith, A.M., Stokes, T.H., Wang, M.D., Young, A.N., Nie, S. (2013) Semiconductor quantum dots for bioimaging and biodiagnostic applications. *Annu. Rev. Anal. Chem.*, **6** (1), 143–162.
- 59 Wang, C., Gao, X., Su, X. (2010) In vitro and in vivo imaging with quantum dots. *Anal. Bioanal. Chem.*, **397** (4), 1397–1415.
- 60 Bruchez, M., Moronne, M., Gin, P., Weiss, S., Alivisatos, A.P. (1998) Semiconductor Nanocrystals as Fluorescent Biological Labels. *Science*, **281** (5385), 2013–2016.
- 61 He, Y., Lu, H.-T., Sai, L.-M., Su, Y.-Y., Hu, M., Fan, C.-H., Huang, W., Wang, L.-H. (2008) Microwave Synthesis of Water-Dispersed CdTe/CdS/ZnS Core-Shell-Shell Quantum Dots with Excellent Photostability and Biocompatibility. *Adv. Mater.*, **20** (18), 3416–3421.
- 62 Hu, H.-Y., Dou, X.-R., Jiang, Z.-L., Tang, J.-H., Xie, L., Xie, H.-P. (2012) Cytotoxicity and cellular imaging of quantum dots protected by polyelectrolyte. *J. Pharm. Anal.*, **2** (4), 293–297.
- 63 Hoshino, A., Fujioka, K., Oku, T., Suga, M., Sasaki, Y.F., Ohta, T., Yasuhara, M., Suzuki, K., Yamamoto, K. (2004) Physicochemical Properties and Cellular Toxicity of Nanocrystal Quantum Dots Depend on Their Surface Modification. *Nano Lett.*, **4** (11), 2163–2169.
- 64 Porta, F., Speranza, G., Krpetić, Ž., Dal Santo, V., Francescato, P., Scari, G. (2007) Gold nanoparticles capped by peptides. *Mater. Sci. Eng.*, **140** (3), 187–194.
- 65 Mirkin, C.A., Letsinger, R.L., Mucic, R.C., Storhoff, J.J. (1996) A DNA-based method for rationally assembling nanoparticles into macroscopic materials. *Nature*, **382** (6592), 607–609.
- 66 Storhoff, J.J., Elghanian, R., Mucic, R.C., Mirkin, C.A., Letsinger, R.L. (1998) One-Pot Colorimetric Differentiation of Polynucleotides with Single Base Imperfections Using Gold Nanoparticle Probes. *J. Am. Chem. Soc.*, **120** (9), 1959–1964.
- 67 An, P., Zuo, F., Wu, Y.P., Zhang, J.H., Zheng, Z.H., Ding, X.B., Peng, Y.X. (2012) Fast synthesis of dopamine-coated Fe₃O₄ nanoparticles through ligand-exchange method. *Chinese Chemical Letters*, **23** (9), 1099–1102.

- 68 Bain, C.D., Troughton, E.B., Tao, Y.-T., Evall, J., Whitesides, G.M., Nuzzo, R.G. (1989) Formation of Monolayer Films by the Spontaneous Assembly of Organic Thiols from Solution onto Gold. *J. Am. Chem. Soc.*, **111** (1), 321–335.
- 69 Love, J.C., Estroff, L.A., Kriebel, J.K., Nuzzo, R.G., Whitesides, G.M. (2005) Self-assembled monolayers of thiolates on metals as a form of nanotechnology. *Chemical reviews*, **105** (4), 1103–1169.
- 70 Lin, S.-Y., Tsai, Y.-T., Chen, C.-C., Lin, C.-M., Chen, C.-h. (2004) Two-Step Functionalization of Neutral and Positively Charged Thiols onto Citrate-Stabilized Au Nanoparticles. *J. Phys. Chem. B*, **108** (7), 2134–2139.
- 71 Kassam, A., Bremner, G., Clark, B., Ulibarri, G., Lennox, R.B. (2006) Place exchange reactions of alkyl thiols on gold nanoparticles. *J. Am. Chem. Soc.*, **128** (11), 3476–3477.
- 72 Henglein, A. and Giersig, M. (1999) Formation of Colloidal Silver Nanoparticles: Capping Action of Citrate. *J. Phys. Chem. B*, **103** (44), 9533–9539.
- 73 Schmid, G. and Corain, B. (2003) Nanoparticulated Gold: Syntheses, Structures, Electronics, and Reactivities. *Eur. J. Inorg. Chem.*, **2003** (17), 3081–3098.
- 74 Weisbecker, C.S., Merritt, M.V., Whitesides, G.M. (1996) Molecular Self-Assembly of Aliphatic Thiols on Gold Colloids. *Langmuir*, **12** (16), 3763–3772.
- 75 Bain, C.D. and Whitesides, G.M. (1989) Modeling Organic Surfaces with Self-Assembled Monolayers. *Adv. Mater.*, **4** (28), 506–512.
- 76 Yu, C.-J. and Tseng, W.-L. (2008) Colorimetric Detection of Mercury(II) in a High-Salinity Solution Using Gold Nanoparticles Capped with 3-Mercaptopropionate Acid and Adenosine Monophosphate. *Langmuir*, **24** (21), 12717–12722.
- 77 Bellino, M.G., Calvo, E.J., Gordillo, G. (2004) Adsorption kinetics of charged thiols on gold nanoparticles. *Phys. Chem. Chem. Phys.*, **6** (2), 424.
- 78 Porter, M.D., Bright, T.B., Allara, D.L., Chidsey, C.E.D. (1987) Spontaneously organized molecular assemblies. 4. Structural characterization of n-alkyl thiol monolayers on gold by optical ellipsometry, infrared spectroscopy, and electrochemistry. *J. Am. Chem. Soc.*, **109** (12), 3559–3568.
- 79 Amoli, B.M., Gumfekar, S., Hu, A., Zhou, Y.N., Zhao, B. (2012) Thiocarboxylate functionalization of silver nanoparticles: Effect of chain length on the electrical conductivity of nanoparticles and their polymer composites. *J. Mater. Chem.*, **22** (37), 20048.
- 80 Wu, L., Wang, Z., Shen, B. (2013) Large-scale gold nanoparticle superlattice and its SERS properties for the quantitative detection of toxic carbaryl. *Nanoscale*, **5** (12), 5274–5278.

- 81 Niidome, T., Nakashima, K., Takahashi, H., Niidome, Y. (2004) Preparation of primary amine-modified gold nanoparticles and their transfection ability into cultivated cells. *Chem. Commun.* (17), 1978–1979.
- 82 Hostetler, M.J., Templeton, A.C., Murray, R.W. (1999) Dynamics of Place-Exchange Reactions on Monolayer-Protected Gold Cluster Molecules. *Langmuir*, **15** (11), 3782–3789.
- 83 Montalti, M., Prodi, L., Zaccheroni, N., Baxter, R., Teobaldi, G., Zerbetto, F. (2003) Kinetics of Place-Exchange Reactions of Thiols on Gold Nanoparticles. *Langmuir*, **19** (12), 5172–5174.
- 84 Templeton, A.C., Hostetler, M.J., Warmoth, E.K., Chen, S., Hartshorn, C.M., Krishnamurthy, V.M., Forbes, M.D.E., Murray, R.W. (1998) Gateway Reactions to Diverse, Polyfunctional Monolayer-Protected Gold Clusters. *J. Am. Chem. Soc.*, **120** (19), 4845–4849.
- 85 Templeton, A.C., Wuelfing, W.P., Murray, R.W. (2000) Monolayer-Protected Cluster Molecules. *Acc. Chem. Res.*, **33** (1), 27–36.
- 86 Oh, E., Susumu, K., Blanco-Canosa, J.B., Medintz, I.L., Dawson, P.E., Mattoussi, H. (2010) Preparation of stable maleimide-functionalized au nanoparticles and their use in counting surface ligands. *Small*, **6** (12), 1273–1278.
- 87 Gibson, J.D., Khanal, B.P., Zubarev, E.R. (2007) Paclitaxel-functionalized gold nanoparticles. *J. Am. Chem. Soc.*, **129** (37), 11653–11661.
- 88 Templeton, A.C., Hostetler, M.J., Kraft, C.T., Murray, R.W. (1998) Reactivity of Monolayer-Protected Gold Cluster Molecules: Steric effects. *J. Am. Chem. Soc.*, **120** (8), 1906–1911.
- 89 Thode, C.J. and Williams, M.E. (2008) Kinetics of 1,3-dipolar cycloaddition on the surfaces of Au nanoparticles. *J. Colloid Interface Sci.*, **320** (1), 346–352.
- 90 Lee, S.H., Bae, K.H., Kim, S.H., Lee, K.R., Park, T.G. (2008) Amine-functionalized gold nanoparticles as non-cytotoxic and efficient intracellular siRNA delivery carriers. *Int. J. Pharm.*, **364** (1), 94–101.
- 91 Zhu, M., Schneider, M., Papastavrou, G., Akari, S., Möhwald, H. (2001) Controlling the Adsorption of Single Poly(styrenesulfonate) Sodium on NH_3^+ -Modified Gold Surfaces on a Molecular Scale. *Langmuir*, **17** (21), 6471–6476.
- 92 Hostetler, M.J., Wingate, J.E., Zhong Chuan-Jian, Harris, J.E., Vachet, R.W., Clark, M.R., Londono, D., Green, S.J., Stokes, R.W., Wignall, G.D., Glish, G.L., Porter, M.D., Evans, N.D., Murray, R.W. (1998) Alkanethiolate Gold Cluster Molecules with Core Diameters from 1.5 to 5.2 nm: Core and Monolayer Properties as a Function of Core Size. *Langmuir*, **14** (1), 14–30.
- 93 Dhawan, A., Sharma, V., Parmar, D. (2009) Nanomaterials: A challenge for toxicologists. *Nanotoxicology*, **3** (1), 1–9.
- 94 Sperling, R.A., Rivera Gil, P., Zhang, F., Zanella, M., Parak, W.J. (2008) Biological applications of gold nanoparticles. *Chem. Soc. Rev.*, **37** (9), 1896–1908.

-
- 95 Mout, R., Moyano, D.F., Rana, S., Rotello, V.M. (2012) Surface functionalization of nanoparticles for nanomedicine. *Chem. Soc. Rev.*, **41** (7), 2539–2544.
- 96 Elsabahy, M. and Wooley, K.L. (2012) Design of polymeric nanoparticles for biomedical delivery applications. *Chem. Soc. Rev.*, **41** (7), 2545–2561.
- 97 Dreaden, E.C., Alkilany, A.M., Huang, X., Murphy, C.J., El-Sayed, M.A. (2012) The golden age: gold nanoparticles for biomedicine. *Chem. Soc. Rev.*, **41** (7), 2740–2779.
- 98 Khandare, J., Calderón, M., Dagia, N.M., Haag, R. (2012) Multifunctional dendritic polymers in nanomedicine: opportunities and challenges. *Chem. Soc. Rev.*, **41** (7), 2824–2848.
- 99 Barenholz, Y. (2012) Doxil®-the first FDA-approved nano-drug: lessons learned. *J. Controlled Release*, **160** (2), 117–134.
- 100 Shi, J., Xiao, Z., Kamaly, N., Farokhzad, O.C. (2011) Self-assembled targeted nanoparticles: evolution of technologies and bench to bedside translation. *Acc. Chem. Res.*, **44** (10), 1123–1134.
- 101 Huang, J.G., Leshuk, T., Gu, F.X. (2011) Emerging nanomaterials for targeting subcellular organelles. *Nano Today*, **6** (5), 478–492.
- 102 Dobrovolskaia, M.A. and McNeil, S.E. (2007) Immunological properties of engineered nanomaterials. *Nature Nanotechnology*, **2** (8), 469–478.
- 103 Yameen, B., Choi, W.I., Vilos, C., Swami, A., Shi, J., Farokhzad, O.C. (2014) Insight into nanoparticle cellular uptake and intracellular targeting. *J. Controlled Release*, **190**, 485–499.
- 104 Derfus, A.M., Chan, W.C.W., Bhatia, S.N. (2004) Probing the Cytotoxicity of Semiconductor Quantum Dots. *Nano Lett.*, **4** (1), 11–18.
- 105 Mammen, M., Choi, S.-K., Whitesides, G.M. (1998) Polyvalente Wechselwirkungen in biologischen Systemen: Auswirkungen auf das Design und die Verwendung multivalenter Liganden und Inhibitoren. *Angew. Chem.*, **110** (20), 2908–2953.
- 106 Gestwicki, J.E., Cairo, C.W., Strong, L.E., Oetjen, K.A., Kiessling, L.L. (2002) Influencing Receptor–Ligand Binding Mechanisms with Multivalent Ligand Architecture. *J. Am. Chem. Soc.*, **124** (50), 14922–14933.
- 107 Cairo, C.W., Gestwicki, J.E., Kanai, M., Kiessling, L.L. (2002) Control of Multivalent Interactions by Binding Epitope Density. *J. Am. Chem. Soc.*, **124** (8), 1615–1619.
- 108 Kiessling, L.L., Gestwicki, J.E., Strong, L.E. (2006) Synthetic multivalent ligands as probes of signal transduction. *Angew. Chem. Int. Ed.*, **45** (15), 2348–2368.
- 109 Kiessling, L.L., Gestwicki, J.E., Strong, L.E. (2000) Synthetic multivalent ligands in the exploration of cell-surface interactions. *Curr. Opin. Chem. Biol.*, **7** (4), 696–703.
- 110 Dervede, J., Enders, S., Reissig, H.-U., Roskamp, M., Schlecht, S., Yekta, S. (2009) Inhibition of selectin binding by colloidal gold with functionalized shells. *Chem. Commun.* (8), 932–934.

- 111 Saada, M.-C., Montero, J.-L., Vullo, D., Scozzafava, A., Winum, J.-Y., Supuran, C.T. (2011) Carbonic Anhydrase Activators: Gold Nanoparticles Coated with Derivatized Histamine, Histidine, and Carnosine Show Enhanced Activatory Effects on Several Mammalian Isoforms. *J. Med. Chem.*, **54** (5), 1170–1177.
- 112 Panigrahi, S., Basu, S., Praharaj, S., Pande, S., Jana, S., Pal, A., Ghosh, S., Pal, T. (2007) Synthesis and Size-Selective Catalysis by Supported Gold Nanoparticles: Study on Heterogeneous and Homogeneous Catalytic Process. *J. Phys. Chem. C*, **111** (12), 4596–4605.
- 113 Sivaraman, S.K., Kumar, S., Santhanam, V. (2011) Monodisperse sub-10 nm gold nanoparticles by reversing the order of addition in Turkevich method - the role of chloroauric acid. *J. Colloid Interface Sci.*, **361** (2), 543–547.
- 114 Biver, T., Corti, A., Eltugral, N., Lorenzini, E., Masini, M., Paolicchi, A., Pucci, A., Ruggeri, G., Secco, F., Venturini, M. (2012) Analysis of 4-dimethylaminopyridine (DMAP)-gold nanoparticles behaviour in solution and of their interaction with calf thymus DNA and living cells. *J. Nanopart. Res.*, **14** (2), 681–693.
- 115 Link, S., Wang, Z.L., El-Sayed, M.A. (1999) Alloy Formation of Gold–Silver Nanoparticles and the Dependence of the Plasmon Absorption on Their Composition. *J. Phys. Chem. B*, **103** (18), 3529–3533.
- 116 Wilcoxon, J. (2009) Optical Absorption Properties of Dispersed Gold and Silver Alloy Nanoparticles. *J. Phys. Chem. B*, **113** (9), 2647–2656.
- 117 Sun, L., Luan, W., Shan, Y.J. (2012) A composition and size controllable approach for Au-Ag alloy nanoparticles. *Nanoscale Res. Lett.*, **7** (1), 225.
- 118 Briñas, R.P., Maetani, M., Barchi, J.J. (2013) A survey of place-exchange reaction for the preparation of water-soluble gold nanoparticles. *J. Colloid. Interf. Sci.*, **392**, 415–421.
- 119 Eustis, S. and El-Sayed, M.A. (2006) Why gold nanoparticles are more precious than pretty gold: noble metal surface plasmon resonance and its enhancement of the radiative and nonradiative properties of nanocrystals of different shapes. *Chem. Soc. Rev.*, **35** (3), 209–217.
- 120 Nuzzo, R.G. and Allara, D.L. (1983) Adsorption of bifunctional organic disulfides on gold surfaces. *J. Am. Chem. Soc.*, **105** (13), 4481–4483.
- 121 Zhao, Y., Pérez-Segarra, W., Shi, Q., Wei, A. (2005) Dithiocarbamate assembly on gold. *J. Am. Chem. Soc.*, **127** (20), 7328–7329.
- 122 Arndt, T., Schupp, H., Schrepp, W. (1989) Self-Assembled And Langmuir-Blodgett Films Of Thiocarbaminates: A Comparative Study. *Thin Solid Films*, **178** (1-2), 319–326.
- 123 Sharma, J., Chhabra, R., Yan, H., Liu, Y. (2008) A facile in situ generation of dithiocarbamate ligands for stable gold nanoparticle-oligonucleotide conjugates. *Chem. Commun.* (18), 2140–2142.

- 124 Kailasa, S.K. and Wu, H.-F. (2012) One-pot synthesis of dopamine dithiocarbamate functionalized gold nanoparticles for quantitative analysis of small molecules and phosphopeptides in SALDI- and MALDI-MS. *Analyst*, **137** (7), 1629–1638.
- 125 Mehta, V.N., Kumar, M.A., Kailasa, S.K. (2013) Colorimetric Detection of Copper in Water Samples Using Dopamine Dithiocarbamate-Functionalized Au Nanoparticles. *Ind. Eng. Chem. Res.*, **52** (12), 4414–4420.
- 126 Banerjee, S., Kar, S., Perez, J.M., Santra, S. (2009) Quantum Dot-Based OFF/ON Probe for Detection of Glutathione. *J. Phys. Chem. C*, **113** (22), 9659–9663.
- 127 Takeuchi, H., Omogo, B., Heyes, C.D. (2013) Are Bidentate Ligands Really Better than Monodentate Ligands For Nanoparticles? *Nano Lett.*, **13** (10), 4746–4752.
- 128 Zhang, M., Liu, Y.-Q., Ye, B.-C. (2011) Colorimetric assay for sulfate using positively-charged gold nanoparticles and its application for real-time monitoring of redox process. *Analyst*, **136** (21), 4558–4562.
- 129 Jv, Y., Li, B., Cao, R. (2010) Positively-charged gold nanoparticles as peroxidase mimic and their application in hydrogen peroxide and glucose detection. *Chem. Commun.*, **46** (42), 8017–8019.
- 130 Portilla, L. and Halik, M. (2014) Smoothly tunable surface properties of aluminum oxide core-shell nanoparticles by a mixed-ligand approach. *ACS Appl. Mater. Interfaces*, **6** (8), 5977–5982.
- 131 Thermo Scientific NHS/Sulfo-NHS, 1–4.
- 132 Staros, J.V., Wright, R.W., Swingle, D.M. (1986) Enhancement by *N*-Hydroxysulfosuccinimide of Water-Soluble Carbodiimide-Mediated Coupling Reactions. *Anal. Bioanal.*, **156** (1), 220–222.
- 133 Roskamp, M., Enders, S., Pfengle, F., Yekta, S., Dekaris, V., Dervede, J., Reissig, H.-U., Schlecht, S. (2011) Multivalent interaction and selectivities in selectin binding of functionalized gold colloids decorated with carbohydrate mimetics. *Org. Biomol. Chem.*, **9** (21), 7448.
- 134 Seiler, N., Demisch, L., Schneider, H. (1971) Biochemie und Funktion von biogenen Aminen im Zentralnervensystem. *Angew. Chem.*, **83**, 53–88.
- 135 Dreyer, D.R., Miller, D.J., Freeman, B.D., Paul, D.R., Bielawski, C.W. (2012) Elucidating the Structure of Poly(dopamine). *Langmuir*, **28** (15), 6428–6435.
- 136 Lee, H., Dellatore, S.M., Miller, W.M., Messersmith, P.B. (2007) Mussel-Inspired Surface Chemistry for Multifunctional Coatings. *Science*, **318** (5849), 426–430.

- 137 Bu, Y. and Lee, S. (2012) Influence of Dopamine Concentration and Surface Coverage of Au Shell on the Optical Properties of Au, Ag, and Ag core Au shell Nanoparticles. *ACS Appl. Mater. Interfaces*, **4** (8), 3923–3931.
- 138 Lu, C.-C., Zhang, M., Li, A.-J., He, X.-W., Yin, X.-B. (2011) 3,4-Dihydroxy-L-phenylalanine for Preparation of Gold Nanoparticles and as Electron Transfer Promoter in H₂O₂ Biosensor. *Electroanalysis*, **23** (10), 2421–2428.
- 139 Xu, C., Xu, K., Gu, H., Zheng, R., Liu, H., Zhang, X., Guo, Z., Xu, B. (2004) Dopamine as A Robust Anchor to Immobilize Functional Molecules on the Iron Oxide Shell of Magnetic Nanoparticles. *J. Am. Chem. Soc.*, **126** (32), 9938–9939.
- 140 Yuen, A.K.L., Hutton, G.A., Masters, A.F., Maschmeyer, T. (2012) The interplay of catechol ligands with nanoparticulate iron oxides. *Dalton Trans.*, **41** (9), 2545–2559.
- 141 Shultz, M.D., Reveles, J.U., Khanna, S.N., Carpenter, E.E. (2007) Reactive Nature of Dopamine as a Surface Functionalization Agent in Iron Oxide Nanoparticles. *J. Am. Chem. Soc.*, **129** (9), 2482–2487.
- 142 Montet, X., Funovics, M., Montet-Abou, K., Weissleder, R., Josephson, L. (2006) Multivalent Effects of RGD Peptides Obtained by Nanoparticle Display. *J. Med. Chem.*, **49** (20), 6087–6093.
- 143 Nichols, D.E. and Nichols, C.D. (2008) Serotonin receptors. *Chem. Rev.*, **108** (5), 1614–1641.
- 144 Cappelli, A., Manini, M., Paolino, M., Gallelli, A., Anzini, M., Mennuni, L., Del Cadia, M., Rienzo, F. de, Menziani, M.C., Vomero, S. (2011) Bivalent Ligands for the Serotonin 5-HT₃ Receptor. *ACS Med. Chem. Lett.*, **2** (8), 571–576.
- 145 Paolino, M., Mennuni, L., Giuliani, G., Anzini, M., Lanza, M., Caselli, G., Galimberti, C., Menziani, M.C., Donati, A., Cappelli, A. (2014) Dendrimeric tetravalent ligands for the serotonin-gated ion channel. *Chem. Commun.*, **50** (62), 8582–8585.
- 146 Park, K. (2013) Facing the Truth about Nanotechnology in Drug Delivery. *ACS Nano*, **7** (9), 7442–7447.
- 147 Shenhar, R. and Rotello, V.M. (2003) Nanoparticles: Scaffolds and Building Blocks. *Acc. Chem. Res.*, **36** (7), 549–561.
- 148 Fasting, C., Schalley, C.A., Weber, M., Seitz, O., Hecht, S., Koksche, B., Dervede, J., Graf, C., Knapp, E.-W., Haag, R. (2012) Multivalency as a Chemical Organization and Action Principle. *Angew. Chem. Int. Ed.*, **51** (42), 10472–10498.
- 149 Greger, R. (2000) Role of CFTR in the Colon. *Annu. Rev. Physiol.*, **62** (1), 467–491.
- 150 Böhme, M., Diener, M., Rummel, W. (1991) Calcium- and cyclic-AMP-mediated secretory responses in isolated colonic crypts. *Pflügers Arch. Eur. J. Phys.*, **419** (2), 144–151.

- 151 Bell, A., Althaus, M., Diener, M. (2015) Communication between mast cells and rat submucosal neurons. *Pflug. Arch. Eur. J. Phy.*, **467** (8), 1809–1823.
- 152 Schultheiss, G., Hennig, B., Schunack, W., Prinz, G., Diener, M. (2006) Histamine-induced ion secretion across rat distal colon: involvement of histamine H₁ and H₂ receptors. *Eur. J. Pharmacol.*, **546** (1-3), 161–170.
- 153 Wang, Y.Z. and Cooke, H.J. (1990) H₂ receptors mediate cyclical chloride secretion in guinea pig distal colon. *Am. J. Physiol.*, **258** (6), G887–G893.
- 154 Strabel, D. and Diener, M. (1995) Evidence against direct activation of chloride secretion by carbachol in the rat distal colon. *Eur. J. Pharmacol.*, **274** (1-3), 181–191.
- 155 Bridges, R.J., Rummel, W., Simon B. (1983) Forskolin induced chloride secretion across the isolated mucosa of rat colon descendens. *Naunyn-Schmiedeberg's Arch. Pharmacol.*, **323** (4), 355–360.
- 156 Hug, F., Diener, M., Scharrer, E. (1996) Modulation by fish oil diet of eicosanoid-induced anion secretion in the rat distal colon. *Z. Ernährungswiss.*, **35** (4), 323–331.
- 157 Garrison, J.C. and Rall, T.W. (1990) Autacoids; drug therapy of inflammation., in *Goodmann and Gilman's The Pharmacological Basis of Therapeutics* (eds A.G. Gilman, T.W. Rall, A.S. Nies, P. Taylor), Pergamon Press, New York, 8th edition, pp. 574–599.
- 158 Brunton, L.L. (1990) Agents for control of gastric acidity and treatment of peptid ulcers., in *Goodmann and Gilman's The Pharmacological Basis of Therapeutics* (eds A.G. Gilman, T.W. Rall, A.S. Nies, P. Taylor), Pergamon Press, New York, 8th edition, pp. 897–913.
- 159 Panula, P., Chazot, P.L., Cowart, M., Gutzmer, R., Leurs, R., Liu, W.L.S., Stark, H., Thurmond, R.L., Haas, H.L. (2015) International Union of Basic and Clinical Pharmacology. XCVIII. Histamine Receptors. *Pharmacol. Rev.*, **67** (3), 601–655.
- 160 Kenyon, J. and Gobbins, W.R. (1977) Effects of Low-Chloride Solutions On Action Potentials of Sheep Cardiac Purkinje Fibers. *J. Gen. Physiol.*, **70** (5), 635–660.
- 161 Tavernaro, I.K. (2014) Multivalente Präsentation potenzieller Inhibitoren der Selektin-Ligand-Wechselwirkungen durch biokompatible Nanopartikel. Justus-Liebig-Universität Gießen. Dissertation.
- 162 Scherrer, P. (1918) Bestimmung der Größe und der inneren Struktur von Kolloidteilchen mittels Röntgenstrahlen. *Gött. Nachr.*, **2**, 98–100.
- 163 Tahir, M.N., Théato, P., Müller, Werner E G, Schröder, H.C., Janshoff, A., Zhang, J., Huth, J., Tremel, W. (2004) Monitoring the formation of biosilica catalysed by histidine-tagged silicatein. *Chem. Commun.* (24), 2848–2849.

10. Appendix

10.1 Abbreviations and Symbols

5HT	Serotonin, 5-hydroxytryptamine	MPSA	3-Mercapto-1-propanesulfonic acid sodium salt
CA	Cysteamine	MR	Magnetic resonance
CB	Carbachol	MS	Mass spectrometry
d	Diameter; doublet (NMR)	MUDA	11-Mercapto-1-undecanoic acid
DA	Dopamine	MUDOL	11-Mercapto-1-undecanol
DLS	Dynamic light scattering	MUDOLS	11-Mercapto-1-undecyl sulfate sodium salt
DTC	Dithiocarbamate	MWCO	Molecular weight cut off
e. g.	<i>Exempli gratia</i> for example	NAc-CA	<i>N</i> -Acetylcysteamine
EDC	1-Ethyl-3-(3-dimethylamino-propyl)carbodiimide	NEt₃	Triethylamine
EDX	Energy dispersive X-ray spectroscopy	NHS	<i>N</i> -Hydroxysuccinimide
equiv.	Equivalent	nm	Nanometer, 10 ⁻⁹ m
FDA	Food and drug administration	NMR	Nuclear magnetic resonance
GABA	γ -Aminobutanoic acid	NP	Nanoparticle
HA	Histamine	PEG	Poly(ethylene glycol)
IC₅₀	Half maximal inhibitory concentration	o/n	Over night
IR	Infra-red	q	Quartet (NMR)
I_{sc}	Short circuit current	QY	Quantum yield
LA	Lipoic acid, 6,8-dithiooctanoic acid	QD	Quantum dot
L-Dopa	Levodopa, L-3,4-dihydroxy - phenylalanine	RT	Room temperature
LED	Light emitting diode	s	Singlet
m	Meter; multiplett (NMR)	SAM	Self-assembled monolayer
MHA	6-Mercapto-1-hexanoic acid	SPION	Superparamagnetic iron oxide nanoparticle
min	Minute	t	Triplet
MPA	3-Mercapto-1-propanoic acid	TEM	Transmission electron microscopy

TGA	2-Mercaptoacetic acid, thioglycolic acid; thermogravimetric analysis	TOPO	Trioctylphosphine oxide
TMAH	Tetramethylammonium hydroxide	UV/Vis	Ultraviolet/visible
TMS	Trimethylsilane	XRD	X-Ray diffraction
TOAB	Tetraoctylammonium bromide	ζ	<i>Zeta</i> -potential
TOP	Trioctylphosphine	potential	
		λ	Wavelength [nm]
		ν	Vibration [cm ⁻¹]

10.2 Calculation of core diameters

The concentration of the particle solution was determined under the assumption that a fully conversion of used salt amounts took place. The average radius of the NP is taken from TEM analysis counting 100 particles.

An example is given for Au nanoparticles:

Volume per particle	$V = \frac{4}{3} \cdot \pi \cdot r^3$	
Mass per particle	$m = \rho \cdot V$	$\rho(Au) = 19.32 \text{ g/cm}^3$
Mol per particle	$n_{\text{Au pro NP}} = m \cdot M$	$M(Au) = 196.97 \text{ g/mol}$
Number NP	$N_{\text{NP}} = \frac{n_{\text{Au ges}}}{n_{\text{Au per NP}}}$	
Mol NP	$M_{\text{NP}} = \frac{N_{\text{NP}}}{N_A}$	$N_A = 6.022 \times 10^{23} \text{ mol}^{-1}$
Concentration NP	$c(NP) = \frac{M_{\text{NP}}}{V}$	

10.3 List of Figures

Figure 1: Length scale for classification of nanomaterials. Adapted from [3].....	1
Figure 2: The Lycurgus cup contains nanoparticles of gold and silver (British Museum). [9]	3
Figure 3: Gold as bulk material and dispersed in water as colloids.	4
Figure 4: Top-down and bottom-up approach for the synthesis of nanoparticles.	5
Figure 5: LaMer diagram to describe nucleation and nucleus growth. Adapted from [12]	6
Figure 6: Growth and stabilization of nanoparticles. Adapted from [3]	7
Figure 7: UV/Vis spectra (normalized) for Au nanoparticles with different core sizes in aqueous solution. Adapted from [32]	10
Figure 8: Plasmon resonance: scheme for oscillation of the electron cloud at a spherical nanoparticle. Adapted from [33]	10
Figure 9: Density of states in a semiconductor crystal in dependence of the dimension. Adapted from [38]	11
Figure 10: Size-dependent photoluminescence (a+b) and absorption and emission spectra (c) of CdSe. Adapted from [41]	12
Figure 11: Quantum dot core materials and their emission wavelengths. Adapted from [57]	14
Figure 12: Confocal fluorescence microscopy images of cells incubated with quantum dots. Two different kinds of modified CdTe coloring nuclei (red) and cytoplasm (green). Adapted from [59]	14
Figure 13: Photostability of a traditional dye compared to quantum dots. Adapted from [61]	15
Figure 14: General scheme for the functionalization of nanoparticles.	16
Figure 15: Mercaptocarboxylic acids for ligand exchange reactions.	17
Figure 16: Different reaction types for covalent attachment of bioactive molecules.	19
Figure 17: Different mechanisms of binding with monovalent and multivalent ligands.	25
Figure 18: TEM images of colloidal gold nanoparticles with different sizes synthesized via the <i>Stucky</i> approach (A, B), the <i>Brust-Schiffrin</i> method (C) and the <i>Turkevich</i> method (D, E).	29
Figure 19: Reaction scheme for the synthesis of citrate-stabilized gold nanoparticles.	30
Figure 20: Reaction scheme for the synthesis of dodecanethiol-stabilized gold nanoparticles in organic solution.	31
Figure 21: Reaction scheme for the biphasic synthesis of DMAP-stabilized gold nanoparticles.	32
Figure 22: UV/Vis absorption spectra of all gold nanoparticles synthesized. For bigger nanoparticles the maximum of the plasmon resonance shifts to longer wavelengths (inset).	33

Figure 23: Reaction scheme for the synthesis of alloyed nanoparticles with the citrate reduction route.....	34
Figure 24: UV/Vis absorption spectra of Au/Ag alloy nanoparticles. The photograph shows the colloidal solutions. The maxima of the plasmon resonance shift linearly between both Au and Ag nanoparticles. The spectra are normalized for a better comparison between the different alloys.	35
Figure 25: Reaction scheme for the ligand exchange at citrate-stabilized gold nanoparticles with mercaptocarboxylic acids.	36
Figure 26: UV/Vis absorption spectra of gold nanoparticles stabilized different ligands compared to Au-Citrate are shown. For short chained ligands MHA and LA no stable solution could be obtained.	37
Figure 27: UV/Vis absorption spectra of gold nanoparticles with different sizes after the ligand exchange reaction with MUDA. All colloidal solutions are stable.	38
Figure 28: UV/Vis absorption spectra of Au/Ag alloy nanoparticles after the ligand exchange with MUDA. All colloidal solutions are stable. The spectra are normalized for better comparison between the different alloys.	38
Figure 29: UV/Vis absorption spectra of gold nanoparticles after the ligand exchange with MUDA, MUDOL and MUDOLS. No stable solution of alcohol-terminated nanoparticles could be obtained.	39
Figure 30: UV/Vis absorption spectra of gold nanoparticles with different core sizes after the ligand exchange with MUDOLS. All colloidal solutions are stable.	40
Figure 31: Reaction scheme of the formation of DTC-anchors followed by the ligand exchange at citrate-stabilized gold nanoparticles.	41
Figure 32: UV/Vis absorption spectra of gold nanoparticles after the exchange with DTC-ligands.	41
Figure 33: Reaction scheme for the ligand exchange with <i>N</i> Ac-CA at Au-Citrate followed by deprotection of the amino moiety.....	42
Figure 34: Reaction scheme for the synthesis of gold nanoparticles with free amino moieties.....	43
Figure 35: Variation of the reaction temperature for the synthesis of amino-stabilized gold nanoparticles.....	44
Figure 36: Variation of the molar ratios for the synthesis of amino-stabilized gold nanoparticles...	44
Figure 37: Surface structure of gold nanoparticles with two different ligand containing either carboxylic acid (MUDA) or sulfated alcohol (MUDOLS) termination.	45
Figure 38: UV/Vis absorption spectra of gold nanoparticles with a mixed ligand shell of both MUDA and MUDOLS are shown. All colloidal solutions are stable.	46

Figure 39: Reaction pathway of the formation of the stable amide bond between carboxylate and amine mediated by EDC and NHS. A: unstable reactive o-acylisourea ester, B: semi-stable amine-reactive NHS ester, C: stable amide bond.....	48
Figure 40: Formation of Au-MUDA-NHS active ester in solution. The product is not stable and hydrolyzed within hours.....	48
Figure 41: Coupling of amines to MUDA-functionalized gold nanoparticles by a NHS/EDC mediated reaction. The resulting nanoparticles are stable in aqueous solution.....	49
Figure 42: Bioactive amines histamine, dopamine, serotonin (5-hydroxytryptamine) and carbachol.	49
Figure 43: UV/Vis spectra of gold nanoparticles (14 nm) functionalized with histamine (HA), dopamine (DA), serotonin (5HT) and carbachol (CB). Au-MUDA is plotted for comparison with the precursor solution.....	50
Figure 44: Histamine functionalized gold nanoparticles with three different core sizes: reaction scheme and TEM images. A $d_{\text{TEM}} = 7.3 \pm 0.9$ nm, $d_{\text{hydr}} = 11 \pm 2$ nm; B $d_{\text{TEM}} = 14.7 \pm 1.2$ nm, $d_{\text{hydr}} = 26 \pm 6$ nm; C $d_{\text{TEM}} = 25.7 \pm 1.2$ nm, $d_{\text{hydr}} = 32 \pm 8$ nm.....	51
Figure 45: Dopamine functionalized gold nanoparticles with two different core sizes: reaction scheme and TEM images. A $d_{\text{TEM}} = 7.8 \pm 1.2$ nm, $d_{\text{hydr}} = 9 \pm 2$ nm; B $d_{\text{TEM}} = 15 \pm 1$ nm, $d_{\text{hydr}} = 26 \pm 6$ nm.	52
Figure 46: Mechanism of the formation of polydopamine under aerobic conditions. [135]	53
Figure 47: Serotonin functionalized gold nanoparticles: reaction scheme and TEM image. Diameter $d_{\text{TEM}} = 14.1 \pm 0.9$ nm, $d_{\text{hydr}} = 16 \pm 4$ nm.....	54
Figure 48: Carbachol functionalized gold nanoparticles: reaction scheme and TEM image. Diameter $d_{\text{TEM}} = 14.5 \pm 0.7$ nm, $d_{\text{hydr}} = 17 \pm 6$ nm.....	55
Figure 49: L-Dopa functionalized gold nanoparticles: reaction scheme and TEM image. Diameter $d_{\text{TEM}} = 30.7 \pm 7.2$ nm, $d_{\text{hydr}} = 45 \pm 9$ nm.....	56
Figure 50: Au-MUDA-HA 7 nm at the serosal side induced a time-dependent increase in the I_{sc} , forskolin was added for the control of proper biological functionality; each peak is an addition of gold nanoparticle samples. Five different samples were tested.	57
Figure 51: Au-MUDA at the serosal side induced a time-dependent increase in I_{sc} , forskolin was added for the control of proper biological functionality; each peak is an addition of gold nanoparticles. Four different samples were tested.	58
Figure 52: Au-MUDA-DA 7 nm (left) and 14 nm (right) at the serosal side induced a time dependent increase in I_{sc} , forskolin was added for the control of biological functionality.	59

- Figure 53: Au-MUDA-5HT at the serosal side induced a time-dependent increase in I_{sc} , forskolin was added for the control of proper biological functionality; each peak is an addition of gold nanoparticles. Four different samples were tested; $n = 7$ 59
- Figure 54: Au-MUDA CB induced an increase in the I_{sc} , native carbachol induced an increase in the I_{sc} at different concentrations; $n = 6$ 60
- Figure 55: Potency of Au-MUDA-CB versus native carbachol; an equivalent potency between Au-MUDA-CB and carbachol was obtained at 1 pM Au-MUDA-CA and 500nM CB. 61
- Figure 56: Synthetic procedure for gold nanoparticles with a mean diameter of 14 nm (NP 1) followed by ligand exchange with 11-mercaptoundecanoic acid (NP 2) and functionalization with histamine (NP 3, Au-MUDA-HA). Double arrows at the Au core represent the ligand. 65
- Figure 57: IR spectra of (a) Au-Citrate NP 1, (b) Au-MUDA NP 2 and (c) Au-MUDA-HA NP 3; vibration for the amide bond is found at 1641 cm^{-1} 66
- Figure 58: (A) UV/Vis spectra of the stepwise functionalization of Au-Citrate NP 1, Au-MUDA NP 2 and Au-MUDA-HA NP 3 nanoparticles. (B) TEM images and DLS measurements with values for the distribution of the hydrodynamic diameters of (i) Au-Citrate NP 1 $d = 14.0 \pm 0.9\text{ nm}$, $d_{hydr} = 16.7 \pm 3.0\text{ nm}$, (ii) Au-MUDA NP 2 $d = 14.5 \pm 1.2\text{ nm}$, $d_{hydr} = 24.1 \pm 6.7\text{ nm}$ and (iii) Au-MUDA-HA NP 3 $d = 14.3 \pm 0.7\text{ nm}$, $d_{hydr} = 19.3 \pm 2.9\text{ nm}$; $d = \text{diameter}$ 67
- Figure 59: (A) Synthetic procedure for the preparation of Au-MUDOLS NP 4, (B) UV/Vis spectra of Au-Citrate NP 1 and Au-MUDOLS NP 4, (C) TEM images and DLS measurements with values for the distribution of the hydrodynamic diameters of (i) Au-Citrate NP 1 $d = 14.0 \pm 0.9\text{ nm}$, $d_{hydr} = 16.7 \pm 3.0\text{ nm}$, (ii) Au-MUDOLS NP 4 $d = 14.3 \pm 1.3\text{ nm}$, $d_{hydr} = 18.6 \pm 2.5\text{ nm}$; $d = \text{diameter}$ 68
- Figure 60: Synthesis of the monovalent analogue AcS-MUDA-HA (3) starting from 11-bromoundecanoic acid 1. Reaction conditions: (a) KSOAc, DMF, 2 h, rt, (b) NHS, DCM, 18 h, rt, (c) EDC, HA·2HCl, NEt_3 , DCM, 6 h, rt. 68
- Figure 61: Au-MUDA-HA ($10^{-11}\text{ mol l}^{-1}$ at the serosal side, arrow) induced an increase in I_{sc} (A), which was almost abolished in the absence of chloride (0 Cl^- ; black bar, (B)). At the end of the experiments, the secretagogues carbachol ($5 \times 10^{-5}\text{ mol l}^{-1}$ at the serosal side, white bars) and forskolin (forsk; $5 \times 10^{-6}\text{ mol l}^{-1}$ at the mucosal and the serosal side, grey bars, (A & B), known to induce chloride secretion, were administered. Line interruptions are caused by omission of time intervals in order to synchronize the tracings of individual records to the administration of drugs. Values are means (symbols) \pm SEM (parallel continuous lines), $n = 6-8$ 69
- Figure 62: Au-MUDA-HA (10^{-11} , 5×10^{-11} , $10^{-10}\text{ mol l}^{-1}$, administered cumulatively at the serosal side, arrows) induced an increase in I_{sc} . (B) AcS-MUDA-HA ($10^{-7.5}$, 10^{-7} , $10^{-6}\text{ mol l}^{-1}$, at

the serosal side, arrows) was ineffective. (C) Au–MUDOLS (10^{-12} , 5×10^{-12} , 10^{-11} mol l^{-1} , at the serosal side, arrows) failed to change the I_{sc} . All particles except Au–MUDOLS preserved the secretory function of the tissues as they did not impair the effect of the secretagogue forskolin (forsk; 5×10^{-6} mol l^{-1} at the mucosal and the serosal side, grey bars). Values are means (symbols) \pm SEM (parallel continuous lines), $n = 4-8$	71
Figure 63: (A) Histamine induced a concentration-dependent increase in I_{sc} . (B) shows the potency of Au–MUDA–HA versus histamine; an equivalent potency between Au–MUDA–HA and histamine was obtained with 10^{-11} mol l^{-1} and 10^{-5} mol l^{-1} , respectively. Values are given as increase in I_{sc} above baseline in short-circuit current (ΔI_{sc}) just before administration of the corresponding drug and are means \pm SEM, $n = 6-8$	72
Figure 64: Mercaptocarboxylic acids used for the synthesis of quantum dots.	79
Figure 65: Reaction scheme for the synthesis of CdTe quantum dots in aqueous solution.	79
Figure 66: Absorption and emission spectra of CdTe quantum dots.	80
Figure 67: Reaction scheme for the synthesis of CdSe quantum dots in aqueous solution.	80
Figure 68: Absorption and emission spectra of CdSe quantum dots.	81
Figure 69: Reaction scheme for the synthesis of CdS quantum dots in aqueous solution.	81
Figure 70: Absorption and emission spectra of CdS quantum dots.	82
Figure 71: Reaction scheme for the passivation of CdTe quantum dots with a ZnS shell.....	82
Figure 72: Summary of absorption and emission spectra of CdTe and CdSe quantum dots with different ligands.	83
Figure 73: Summary of absorption and emission spectra of passivated CdTe quantum dots and their precursors.	84
Figure 74: Overview of CdTe quantum dots used for biological applications.	85
Figure 75: Crypts incubated with the QDs for 1 h in a Tyrode buffer solution; fluorescence intensity before and afterwards was compared. X-axis exposure time, Y-axis in arbitrary units.....	86
Figure 76: Crypts incubated with the QDs for 1 h in a Tyrode buffer solution; fluorescence intensity before and afterwards was compared. X-axis exposure time, Y-axis in arbitrary units.....	87
Figure 77: Crypts incubated with the QDs for 1 h in a buffer solution (tyrode).	87
Figure 78: Synthetic procedure for the mixed crystal system $\text{CdTe}_x\text{Se}_{1-x}$	88
Figure 79: Emission ($\lambda_{\text{ex}} = 350$ nm) and absorption maxima of $\text{CdTe}_x\text{Se}_{1-x}$ -MPA with $x = 0.0$ to $x = 1.0$ Inset: Photography of $\text{CdTe}_x\text{Se}_{1-x}$ -MPA with $x = 0.1$ to $x = 1$ under the UV lamp ($\lambda_{\text{ex}} = 366$ nm).	89
Figure 80: XRD patterns of $\text{CdTe}_x\text{Se}_{1-x}$ -MPA with $x = 0.0$ to $x = 1$. Both binary compounds CdTe and CdSe are also shown for comparison with the mixed crystal system.....	90
Figure 81: Histamine functionalized gold nanoparticles and native histamine.....	94

10.4 List of Tables

Table 1: Summary of the nanoparticle characterization methods.	20
Table 2: Reaction conditions for the synthesis of Au-Citrate nanoparticles in aqueous solution. [112]	30
Table 3: Three different gold nanoparticles synthesized through reduction of HAuCl_4 with different amounts of $\text{Na}_3\text{Citrate}$. TEM and DLS values are given for the determination of the core size. Scale bar is 20 nm.	31
Table 4: Different gold nanoparticles were synthesized in different organic solvents. TEM and DLS values are given for the determination of the core size.	32
Table 5: Reaction conditions for the deprotection of the amino moiety at gold nanoparticles.	43
Table 6: <i>Zeta</i> -Potential measurements of gold nanoparticles with different mixed ligand shells.	47
Table 7: Effects of additive concentrations of Au–MUDA–HA 14 nm on I_{sc} and H_1 and H_2 receptors.	70
Table 8: Quantum dots stabilized with different ligands and the analogues passivated with a ZnS shell.	85
Table 9: Overview $\text{CdTe}_x\text{Se}_{1-x}$ -MPA quantum dots: diameter, composition, absorption and emission maxima.	91

11. Publications and Presentations

Publications:

- Friederike Gasiorek, Ervice Pouokam, Martin Diener, Sabine Schlecht, Mathias S. Wickleder: Effects of Multivalent Histamine Supported on Gold Nanoparticles: Activation of Histamine Receptors by Derivatized Histamine at Subnanomolar Concentrations *Org. Biomol. Chem.* **2015**, 13, 9984-9992.

Oral Presentations:

- “Dopamine-functionalized Nanoparticles – Synthesis, Characterization and Application”
Nanodays Köln, September 5-7, 2013
- “Multivalent Presentation of Bioactive Amines on Nanoparticles “
Nanodays Aachen, September 4-6, 2014
- “Synthesis, Characterization and Application of Gold Nanoparticles with Multivalently Presented Histamine”
17. JCF-Frühjahrssymposium, March 25-28, 2015
- “Quantum Dots for Cellular Imaging”
GGL 8th Annual Conference Gießen, September 30 / October 1, 2015

Poster Presentations:

- “Synthesis of Water Soluble Gold Nanoparticles for Biomedical Applications”
Wissenschaftsforum Darmstadt, September 1-4, 2013; GGL 6th Annual Conference Gießen, September 11-12, 2013
- “Multivalent Presentation of Bioactive Ligands on Functionalized Noble Metal Nanoparticles”
INASCON Middelfahrt, Denmark, September 11-14, 2014
- “Synthesis, Characterization and Application of Gold Nanoparticles with Multivalently Presented Histamine”
GGL 7th Annual Conference Gießen, September 17-18 2014; 17. JCF-Frühjahrssymposium, March 25-28, 2015
- “Multivalent Presentation of Histamine on Bioactive Nanoparticles”
Multivalenzsymposium Berlin, October 23-24, 2014
- “Structural and Optical Properties of CdTe_xSe_{1-x} Nanoparticles”
Materialforschungstag Marburg, July 9, 2015
- “Synthesis and Characterization of Water-Dispersed CdX (X = Se, Te) Quantum Dots for Cellular Imaging”
Wissenschaftsforum Dresden, August 30-September 3, 2015

12. Lebenslauf

Der Lebenslauf wurde aus der elektronischen Version der Arbeit entfernt.

13. Acknowledgement

Beim Verfassen dieser Arbeit bin ich von vielen Seiten fachlich und auch menschlich unterstützt worden. An dieser Stelle sei den Personen herzlich gedankt.

Im Einzelnen möchte ich mich ausdrücklich bei Prof. Dr. Siegfried Schindler bedanken, der die Betreuung dieser Arbeit übernommen hat und mir stets Vertrauen und Freiheit beim Bearbeiten des Themas entgegen gebracht hat.

Ebenfalls bedanken möchte ich mich bei Prof. Dr. Mathias S. Wickleder, der mich in seine Arbeitsgruppe aufgenommen hat und den Nanopartikeln eine Zukunft gibt.

Sabine Schlecht danke ich für die Vergabe des interessanten Themas.

Meinen Kooperationspartnern Prof. Dr. Martin Diener und Dr. Ervice Pouokam möchte ich für die Durchführung der Experimente in der Veterinärphysiologie und die tolle Zusammenarbeit über die letzten drei Jahre danken.

Bedanken möchte ich mich auch bei Anne S. Schulze für die Anfertigung der TEM-Bilder und bei Oliver Falkenbach für die XRD-Messungen.

Dr. Christian Logemann, Felix Machka und Ken James danke ich für die Korrekturen, Anne S. Schulze und Jolanthe Lintl danke ich für sorgfältiges und aufmerksames Lesen der Arbeit.

Für die stets gute Zusammenarbeit und zahlreichen anregenden Diskussionen danke ich den Mitgliedern der Arbeitsgruppen Schindler und Wickleder.

Ich danke auch allen Mitarbeitern des Fachbereiches, die diese Arbeit mit Messungen, Ratschlägen und Diskussionen unterstützt haben.

Bei Michael Linden möchte ich mich für seine große Hilfsbereitschaft, nicht nur während der Promotion, bedanken, auf welche ich mich immer verlassen konnte.

Nicht zuletzt geht ein großes Dankeschön an meine Familie für die bedingungslose Unterstützung während der gesamten Studienzeit. Felix Machka danke ich für den stetigen Zuspruch und die viele Geduld in den letzten Jahren.

14. Erklärung

Versicherung nach § 17 der Promotionsordnung

Ich erkläre: Ich habe die vorgelegte Dissertation selbstständig und ohne unerlaubte fremde Hilfe und nur mit den Hilfen angefertigt, die ich in der Dissertation angegeben habe. Alle Textstellen, die wörtlich oder sinngemäß aus veröffentlichten Schriften entnommen sind, und alle Angaben, die auf mündlichen Auskünften beruhen, sind als solche kenntlich gemacht. Ich stimme einer evtl. Überprüfung meiner Dissertation durch eine Antiplagiat Software zu. Bei den von mir durchgeführten und in der Dissertation erwähnten Untersuchungen habe ich die Grundsätze guter wissenschaftlicher Praxis, wie sie in der „Satzung der Justus-Liebig-Universität Gießen zur Sicherung guter wissenschaftlicher Praxis“ niedergelegt sind, eingehalten.

Ort, Datum

Unterschrift